HZDR-063

DEVELOPMENT AND VALIDATION OF ADVANCED THEORETICAL MODELING FOR CHURN-TURBULENT FLOWS AND SUBSEQUENT TRANSITIONS

Gustavo Montoya

Wissenschaftlich-Technische Berichte
HZDR-063· ISSN 2191-8708

WISSENSCHAFTLICH-
TECHNISCHE BERICHTE

HZDR
HELMHOLTZ
ZENTRUM DRESDEN
ROSSENDORF

Wissenschaftlich-Technische Berichte
HZDR-063

Gustavo Montoya

DEVELOPMENT AND VALIDATION OF ADVANCED THEORETICAL MODELING FOR CHURN-TURBULENT FLOWS AND SUBSEQUENT TRANSITIONS

HZDR

HELMHOLTZ
ZENTRUM DRESDEN
ROSSENDORF

Druckausgabe: ISSN 2191-8708

Elektronische Ausgabe: ISSN 2191-8716

Qucosa: http://fzd.qucosa.de/startseite/

Die vorliegende Arbeit wurde sowohl als Dissertation an der Fakultät III – Prozesswissenschaften der Technischen Universität Berlin, sowie als Wissenschaftlich-Technischer Bericht des Helmholtz-Zentrum Dresden – Rossendorf mit der Berichtsnummer **HZDR-063** veröffentlicht.

2015

Herausgegeben vom

Helmholtz-Zentrum Dresden - Rossendorf

Bautzner Landstraße 400

01328 Dresden

Germany

Development and Validation of Advanced Theoretical Modeling for Churn-Turbulent Flows and Subsequent Transitions

vorgelegt von
Dipl.-Ing.
Gustavo Adolfo Montoya Zabala
geb. in Caracas, Venezuela

von der Fakultät III – Prozesswissenschaften
der Technischen Universität Berlin
zur Erlangung des akademischen Grades

Doktor der Ingenieurwissenschaften
- Dr.-Ing. -

genehmigte Dissertation

Promotionsausschuss:

Vorsitzender: Prof. Dr. Felix Ziegler
Gutachter: Prof. Dr. Matthias Kraume
Gutachter: Prof. Dr. Uwe Hampel
Gutachter: Prof. Dr. Emilio Baglietto

Tag der wissenchaftlichen Aussprache: 10. Juli 2015

Berlin 2015

‘Everything is theoretically impossible, until it is done.’ [1]

[1]Robert A. Heinlein (*1907, †1988)

Acknowledgements

These last three years have been full of meaningful people which, in some way or another, have greatly influenced me both, scientifically and personally. It is difficult to mention them all, but I will do my best.

First of all, I want to thank my family, Gustavo Gerardo Montoya, Aura Elena Zabala De Montoya, and Cristal Carolina Montoya. It is due to their unconditional support and the values which they have instilled in me that I am the man who I am today. Without them, the set of events which led me here, would not have been possible. It is from them that I have learnt that one must never quit, one must endure independently of any present difficulties.

I would like to acknowledge Dr. Dirk Lucas, Dr. Gunther Gerbeth and E.ON Kernkraft for allowing me the opportunity to base my PhD work in this amazing topic and for their support during these last three years. I also thank Dr. Dirk Lucas for his great guidance and supervision. I would also like to acknowledge my research group at the CFD department of HZDR, and especially, Dr. Eckhard Krepper, Dr. Thomas Höhne, Dr. Yixiang Liao, Dr. Roland Rzehak, and Thomas Ziegenhein for their support during my PhD.

I want to express my utmost gratitude to Prof. Emilio Baglietto for having granted me the opportunity of being part of his group at MIT for a year as a visiting student. He always had his door open for his students, ready for listening and to provide meaningful and most of the time, fascinating discussions. Equally, I would also like to acknowledge his research team and specially Rosie Sugrue, Giancarlo Lenci, Lindsey Gilman, Nazar Lubchenko, Etienne Demarly, Ben Magolan, Sasha Tan-Torres, Mariana Rodriguez-Buno, Eugeny Sosnovsky, and Giulia Agostinelli. Honestly, it was always refreshing to see your everlasting interest in engaging, understanding, and discussing a different selection of scientific problems, and it never mattered how far away from your current topic it was. Personally, of course, all of you and your friendship made my life at MIT truly enjoyable and, at times, oddly interesting. I also would like to acknowledge the support received from the DOE sponsored Consortium for Advanced Simulation of Light Water Reactors (CASL) during part of my research at MIT.

Finally, “away“ from the scientific work, I would like to thank my friends: Daniela Baldova, Susan Dürigan, Susann Hänsch, Reuven Rachamin, Petra Hodulikova, Dana Melzer, Michael Melzer, Tomas Skripcak, and Olga Roshchupkina. If life got tough you were there, and if life was good, you were also there. My time in Dresden would have never been so unique and amazing without knowing each and every one of you. I deeply thank you all.

Abstract

Gustavo Montoya, Institute of Chemical and Process Engineering, PhD thesis 2015

Development and Validation of Advanced Theoretical Modeling for Churn-Turbulent Flows and Subsequent Transitions

The applicability of CFD codes for two-phase flows has always been limited to special cases due to the very complex nature of its interface. Due to its tremendous computational cost, methods based on direct resolution of the interface are not applicable to most problems of practical relevance. Instead, averaging procedures are commonly used for these applications, such as the Eulerian-Eulerian approach, which necessarily means losing detailed information on the interfacial structure. In order to allow widespread application of the two-fluid approach, closure models are required to reintroduce in the simulations the correct interfacial mass, momentum, and heat transfer.

It is evident that such closure models will strongly depend on the specific flow pattern. When considering vertical pipe flow with low gas volume flow rates, bubbly flow occurs. With increasing gas volume flow rates larger bubbles are generated by bubble coalescence, which further leads to transition to slug, churn-turbulent, and annular flow. Considering, as an example, a heated tube producing steam by evaporation, as in the case of a vertical steam generator, all these flow patterns including transitions are expected to occur in the system. Despite extensive attempts, robust and accurate simulations approaches for such conditions are still lacking.

The purpose of this dissertation is the development, testing, and validation of a multifield model for adiabatic gas-liquid flows at high gas volume fractions, for which a multiple-size bubble approach has been implemented by separating the gas structures into a specified number of groups, each of which represents a prescribed range of sizes. A fully-resolved continuous gas phase is also computed, and represents all the gas structures which are large enough to be resolved within the computational mesh. The concept, known as GENeralized TwO Phase flow or GENTOP, is formulated as an extension to the bubble population balance approach known as the inhomogeneous MUltiple SIze Group (iMUSIG). Within the polydispersed gas, bubble coalescence and breakup allow the transfer between different size structures, while the modeling of mass transfer between the polydispersed and continuous gas allows including transitions between different gas morphologies depending on the flow situations. The calculations were performed using the computational fluid dynamic code from ANSYS, CFX 14.5, with the support of STAR-CCM+ v8.06 and v9.02. A complete three-field and four-field model, including a continuous liquid field and two to three gas fields representing bubbles of different sizes, were first tested for numerical convergence and then validated against experimental data from the TOPFLOW and MT-Loop facilities.

Zusammenfassung

Gustavo Montoya, Institut für Prozess- und Verfahrenstechnik, Doktorarbeit 2015

Entwicklung und Validierung einer neuartigen Modellierung von turbulent aufgewühlten Strömungen und deren anschließenden Regimewechsel

Aufgrund der komplexen Natur der Grenzfläche in Blasenströmungen ist die Anwendbarkeit von CFD-Codes für Mehrphasenströmungen seit jeher auf Spezialfälle begrenzt. Eine Auflösung aller Grenzflächen in solchen Strömungen ist wegen des enormen Rechenaufwandes nicht möglich, deshalb werden für gewöhnlich Mittelungsverfahren wie die Euler-Euler Methode benutzt um solche Probleme handhabbar zu machen. Eine Mittelung bedeutet notwendigerweise, dass die Struktur der Grenzfläche verloren geht, um dennoch eine korrekte Modellierung des Energie-, Impuls- und Stoffaustausches zu gewährleisten werden Schließungsmodelle benutzt. Dabei ist es offensichtlich, dass solche Schließungsmodelle stark vom vorherrschenden Strömungszustand abhängen. In einem vertikalen Rohr herrscht zum Beispiel bei kleinen Gasbelastungen eine Blasenströmung, mit zunehmenden Gasvolumenstrom wächst die Anzahl und auch koaleszenzbedingt die Größe der Blasen bis die Blasen den gesamten Rohrquerschnitt einnehmen und eine Kolbenströmung entsteht. Bei weiterer Erhöhungen des Gasvolumenstromes wird die Kolbenströmung stark turbulent und aufgewühlt bis sich schließlich eine Ringströmung bildet. Betrachtet man zum Beispiel ein beheiztes Rohr in einem Dampferzeuger können all diese Strömungszustande mit ihren komplexen Übergangszuständen auftreten. Trotz der Notwendigkeit all diese Zustände mit einem Verfahren zu simulieren, konnte bis jetzt kein solches Verfahren entwickelt werden das zufriedenstellend hinsichtlich Robustheit und Genauigkeit ist. Das Ziel dieser Arbeit ist die Entwicklung und Validierung einer Mehrfeld-Methode für adiabate Gas-flüssig-Strömungen bei hohen Gasgehalten. Die Mehrfeld-Methode beschreibt dabei die Aufteilung der Gasstrukturen in nicht aufgelöste disperse Gasstrukturen und aufgelöste kontinuierliche Strukturen in verschiedene Felder, wobei die dispersen Gasstrukturen untereinander weiter aufgeteilt werden. Die kontinuierlichen Strukturen sind dabei diejenigen, die groß genug sind um durch das verwendete Berechnungsgitter aufgelöst zu werden. Die nicht aufgelösten Blasen in den dispersen Feldern werden dabei mit dem Populations-Bilanz-Modell iMUSIG (inhomogeneous MUltiple SIze Group) beschrieben und die aufgelösten Gasstrukturen im kontinuierlichen Feld mit dem GENTOP (GENeralized TwO Phase flow)-Modell beschrieben was als Erweiterung des iMUSIG-Modells formuliert wird. Die Blasengrößenverteilung beim iMUSIG-Modell wird dabei durch Blasenkoaleszenz- und Zerfallsmodelle bestimmt. Der Übergang zwischen der dispersen Phase und der kontinuierlichen Phase wird hingegen von Modellen bestimmt die Abhängig von der Strömungssituation sind. In der Arbeit werden Drei-Feld und Vier-Feld Modelle verwendet die ein kontinuierliches Feld und zwei bzw. drei disperse Felder enthalten. Als erstes wird die Konvergenz der Methode untersucht und anschließend mit experimentellen Daten aus den TOPFLOW und MT-Loop Versuchsanlagen validiert. Die Rechnungen wurden mit den kommerziellen CFD Programm ANSYS, CFX 14.5 durchgeführt, außerdem wurde mit den Programmen STAR-CCM+ v8.06 und v9.02 unterstützende Rechnungen durchgeführt und Codeunabhängigkeit gezeigt.

Contents

List of Figures

List of Tables

Nomenclature

Abbreviations

0D, 1D, 2D, 3D	Zero, One, Two, and Three Dimensional
AIAD	Algebraic Interfacial Area Density
ASMM	Algebraic Slip Mixture Model
ATHLETE	Analysis of Thermal-hydraulics of Leaks and Transients
BIT	Bubble Induced Turbulence
BPBE	Bubble Population Balance Equation
BWR	Boiling Water Reactor
CSF	Continuum Surface Force
CFD	Computational Fluid Dynamics
FAD	Favre Averaged Drag
DN	Nominal Diameter
DNS	Direct Numerical Simulations
GENTOP	Generalized Two Phase Flow
HZDR	Helmholtz-Zentrum Dresden-Rossendorf
LES	Large Eddy Simulation
LOCA	Loss of Coolant Accident
PLIC	Piecewise Linear Interface Calculation
RANS	Reynolds Averaged Navier Stokes
MT-Loop	Measurement Test Loop
iMUSIG	Inhomogeneous Multiple Size Group
MUSIG	Multiple Size Group
PWR	Pressurized Water Reactor
TOPFLOW	Transient Two Phase Flow
VOF	Volume Of Fluid

Symbols

α	Void fraction	
β	Averaged factor	
k	Turbulence kinetic energy, kappa vector	$m^2\ s^{-2}$
ε	Turbulence eddy dissipation	$m^2\ s^{-3}$

μ	Dynamic viscosity	kg m^{-1} s^{-1}
ρ	Density	kg m^{-3}
σ	Surface tension	N m^{-1}
Y	Kinematic viscosity	m^2 s^{-1}
γ	Young module	
φ	Blending function	
τ_0	Oscillating period	s
ω_0	Oscillating frequency	Hz
C	Coefficient	
D	Diameter	m
M	Morton number	
R	Radius	m
S	Source term	
V	Velocity	m s^{-1}
Z	Distance from the nose of a bubble directed downward	m
a	Constant	
g	Gravity	m s^{-2}
j	Superficial velocity	m s^{-1}
p	Pressure	Pa
t	Time	s
y	Distance from the wall boundary	m
T	Temperature	
AF	Acceleration factor	
Ca	Cauchy number	
Eo	Eötvos number	
Fr	Froude number	
$\boldsymbol{M}^i$	Interfacial force for component i	N m^{-3}
Re	Reynolds	
$Rint$	Radius of the bubble interface	m
SF	Scale factor	
ST	Surface tension	
We	Weber number	
j^*	Dimensionless superficial velocity	
$\dot{m}$	Mass flow rate	kg s^{-1}
Δx	Characteristic cell length scale	m

Indexes

A	Area
B	Bubble
D	Drag
L	Lift
T	Tube; Terminal
W	Wall
b	Bubble
c	Constant
d	Dispersed
g	Gas
h	Horizontal
k	Phase-k
l	Liquid
m	Mixture
n	General coefficient, normal
p	Particle
t	Tangential
w	Wall
LG	Liquid-Gas
SP	Seed point
SL	Solid-Liquid
SG	Solid-Gas
TD	Turbulence dispersion
VM	Virtual mass
clust	Clustering
crit	Critical
c, max	Maximum cap bubble limit
d, max	Maximum distorted bubble limit
cg	Continuous gas
ds	Spherical bubble limit
fs	Free surface
max	Maximum
min	Minimum

1 Introduction

Two-phase gas-liquid flows are usually observed in a large range of industrial applications, including the petrochemical, pharmaceutical, biochemical, nuclear, and metallurgical industries. Bubbly flow conditions, are often useful in the cultivation of bacteria and mold fungi, production of cell proteins, animal cell cultures, and treatment of sewage in the biochemical industry. Higher-turbulent flows, as for example the churn-regime, are frequently used in highly exothermic processes such as liquid phase methanol synthesis, Fischer-Tropsch synthesis, and hydrogenation MAC. The understanding of these flow regimes is also very important in the nuclear industry, for example in Boiling Water Reactors (BWR), where the accurate knowledge of the correct distribution of the void fraction allows the prediction of moderator density curves, which strongly influence the neutronics performance and local power production, as well as the heat transfer within the reactor core. Highly turbulent two-phase flows can also be relevant in nuclear reactor safety analyses, an example is the investigation of the manifestation of flashing instabilities in the riser of passive systems during startup conditions, which are a potential occurrence in the German BWR concept known as KERENA (Leyer and Which, 2012). Similarly, studies based on hot leg models of Pressurized Water Reactors (PWR) have shown that churn-turbulent and slug flows play an important role in the evolution of Counter Current Flow Limitation (CCFL) during the depressurization accident scenario identified as Loss of Coolant Accident also known as LOCA (Navarro et al., 2005; Deendarlianto et al., 2011; Montoya et al., 2012; Al Issa & Macian-Juan, 2013).

Extensive experimental studies have been conducted in support of the understanding of two-phase flows. These studies include visual observations and application of various linear and non-linear time-series techniques such as spectral analysis, chaos analysis, stochastic modeling, and multi-resolution analyses. Still, empirical correlations have shown large discrepancies in their predictions for the same operating and design conditions. Although large advances have been made in theoretical and computational methods, progressing from one-dimensional models to full 2D and 3D approaches, capable of accounting for non-uniformities in radial gradients for heterogeneous flows, the modeling is still limited by the accuracy of the interfacial momentum representation.

Most of the experimental work on two-fluid approaches, as well as the development of closure models, has been largely focused on low gas volume fractions typical of bubbly flow. The behavior of the small bubbles in this flow regime has been extensively studied and characterized by various authors including, as representative, the work of Whalley (1987) on drag forces, and the extensive experimental and theoretical studies on drag and non-drag forces of Tomiyama (2002). At the same time, these closure laws have been applied on a wide regime of scenarios, with acceptable agreement against experimental results (Ziegenhein et al., 2015; Rzehak et al., 2014; Liao et al., 2015).

The complexity of the two-phase flows increases with the rise in void fraction, where countering mechanisms induce on the one side coalescence of the small bubbles into larger ones, and on the other breakup of the large structures. Furthermore, the increase in bubble sizes also introduces a higher level of complexity at the interface, as a consequence of the increasing turbulent conditions of the liquid phase. The increased deformability makes the theoretical modeling of the large bubbles particularly difficult.

The challenges of modeling high void fraction regimes increases due to the very limited information that can be extracted from experimental data. While local and transient information has been obtained for the small and large bubble mixtures (Prasser et al., 2007; Lucas et al., 2005), churn-like bubbles are extremely unstable and therefore not prone to separate analysis, which would be essential, for developing appropriate lift closure relations.

The lack of data and insufficient understanding of the physics behind churn-turbulent flows, have brought discrepancies in its definition starting from Vermeer and Krishna (1981) who expressed that no interaction exist between large and small bubbles. In turn, Chen et al. (1994), defined that small and large bubbles do interact in a mostly chaotic scenario, and that a transitional flow between bubbly and churn-regime occurs, where large bubbles are mostly in the center, while small bubbles are entrained at the wall of the pipe recirculating due to a liquid downward flow. Later experimental data (Beyer et al., 2008; Lucas et al., 2010) showed that a combination of both scenarios occurs in churn-turbulent flow. In reality, this flow regime is characterized by large spiraling, transient, vortex-like structures which move throughout the system. These vortices contain large, highly distorted bubbles that concentrate in the core of the pipe and draw small bubbles in their wake (Fig. 1.1). At low liquid flow rates, close to bubble column conditions ($V_l = 0$), due to buoyancy forces, the void fraction maximum in the pipe or column center induces a liquid recirculation with the water rising at the center and falling in the wall region.

Due to its characteristically transient behavior in both space and time, 0D and 1D methods are not truly applicable for these highly turbulent regimes. Furthermore, usefulness and applicability of Computational Fluid Dynamics (CFD) codes in this type of flow regime suffer from incomplete understanding of the complex counteracting physical mechanisms. The lack of complete understanding, together with the absence of reliable experimental data for churn-like and slug bubbles, render the modeling via the Eulerian-Eulerian approaches extremely challenging due to the difficulty of assembling robust closure models for the deformable gas structures. Additionally, Direct Numerical Simulation (DNS) of such flows in realistic configurations is still not achievable with the state-of-the-art of computational power. In this work, a new approach is proposed to more accurately represent this class of problems, based on a hybrid representation that takes into account different resolution methods based on the different interfacial structures. The approach still requires the correct prediction of bubble breakup and coalescence between the different bubbles sizes.

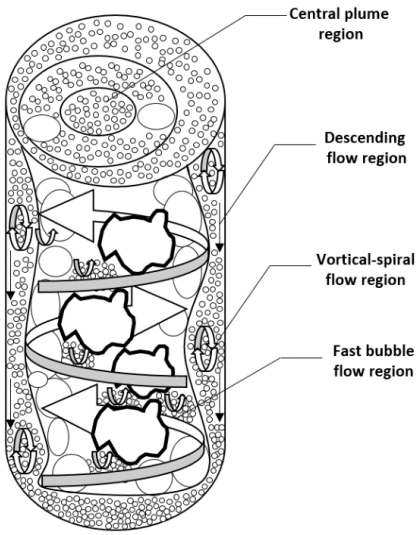

Fig. 1.1 Churn-turbulent flow hydrodynamics representation based on TOPFLOW experimental data.

1.1 Thesis objectives

The main objectives of this thesis are:

- To develop a new multifield model for adiabatic gas-liquid flows at high gas volume fractions, which includes a more realistic approach behind the churn and slug-like bubbles, including its interaction with smaller gas structures.
- To implement this method in the commercially available ANSYS CFX software.
- To validate the model and to evaluate the influence of the new set of physics against a series of analytical models and experimental data, in order to enhance the accuracy of the code predictions in steady-state and transient calculations. These included adiabatic vertical pipe flows of different diameters under churn, slug, and annular flow regimes.

The objectives were pursued according to the following steps:

- A comprehensive study of the available literature on modeling high void fraction regimes was performed, allowing a thorough understanding of the state-of-the-art, and evidencing the existing limitations.
- As a starting point, a set of well-validated closure models which has been developed for bubbly flows were used, and its limitations were studied.
- Optimization of closure models were made in order to stablish a baseline approach for polydispersed representation of high void fraction regimes.
- Starting from the polydispersed approach conclusions, a hybrid model known as GENTOP was later assembled. The initial model performance was evaluated for the application to churn and slug flow regimes and provided a first assessment of the model potential.
- A progressive improvement of the GENTOP approach was performed through continuous testing and separate submodel validation. All modifications to the improved version of

GENTOP have been systematically tested against the complete data set and are discussed in detail in comparison to both analytical and experimental understanding.

1.2 Thesis structure

Chapter 2 reviews the state-of-the-art, as well as the evolution on the understanding and theoretical modeling of the churn-turbulent flow regime and subsequent transitions. The basics of two-phase flow modelling approaches for high void-fraction regimes are also described in this section, focusing on the adopted methods. Chapter 3 introduces the description of the experimental facilities that were used for validation of the two-phase pipe flow cases in this dissertation.

Chapter 4 focuses on the challenges and limitations of theoretical modeling for high void fraction regimes. The first section of the chapter describes the physical mechanisms behind the different models evaluated, followed by a discussion of numerical discretization methods and details on the experimental validation data; the second part discusses the challenges related to the model application to churn and slug-like gas structures. Chapter 5 presents the details on the studies and improvements for extending the HZDR bubbly flow baseline model to higher void fraction regimes. The chapter also discussed the details of the validation, capabilities and limitations of the polydispersed approach as implemented in the CFX software.

Chapter 6 discusses the assessment and resulting limitations of the GENeralized TwO Phase flow (GENTOP) concept for a high void fraction regime application. The description of the conceptual approach adopted in GENTOP, together with qualitative and quantitative validation are presented, including the discussion of the advantages and open challenges. Chapters 7 is dedicated to the analysis of the progressive GENTOP model improvements, which aim at improving the physical representation in order to extend the generality and robustness of the approach. The chapter focuses on the modifications to the different closure components and modeling of the bubble size distribution for the continuous gas. A key aspect discussed in this chapter is the implementation of a surface tension model inside the GENTOP framework, which provides a more realistic representation of the large gas structures. The implementation and validation of the capability of including the effect of the contact angle between the fluids interface and the walls are also encompassed in Chapter 7.

Finally, chapter 8 provides an overall summary of the extensive model development, validation and application experience, together with the main conclusions derived from the work. Further, Annex A.1 presents the applicability of the final GENTOP model assemble in this work to the simulation of annular flows. The encouraging results indicate the potential of adopting this concept for simulation of Boiling Water Reactors (BWR) in the near future.

2 Understanding and modeling of churn-turbulent flows and subsequent flow transitions

2.1 Characterization of churn-turbulent flows

2.1.1 Flow patterns

In vertical pipe flows, four types of flow patterns are commonly observed. These flow regimes are known as homogeneous (bubbly), heterogeneous (churn-turbulent), slug, and annular flow (Fig. 2.1). Depending on the flow regime, both, the morphology of the gas phase, as well as its interaction with the continuous liquid phase, vary considerably. While this review focuses mostly on the churn-turbulent flow regime, an understanding of the other three flow patterns is useful in order to properly appreciate the physical mechanisms and their influence on the later transition from and to the heterogeneous regime.

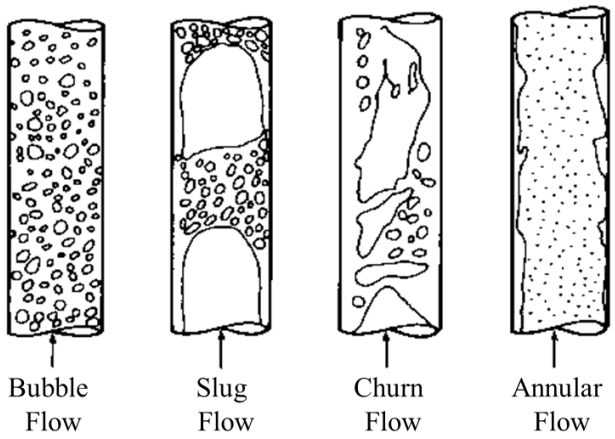

Fig. 2.1 Various flow regimes in vertical upward air-water systems. Adapted from Weisman (1983).

The bubbly flow regime is characterized by the occurrence of spherical, ellipsoidal and/or cap bubbles. In Fig. 2.2, a commonly adopted map is presented, which is based on the Reynolds (Eq. 2.1), Eötvos (Eq. 2.2), and Morton (Eq. 2.3) numbers, to describe the expected bubble morphology. In the case of low gas volume fractions only small bubbles are present, as the surface tension is the dominant force. Such spherical bubbles can be treated as spheres, but require modified formulation of the closure forces due to the mobility of the interface. As the gas volume fraction starts to increase, the small bubbles start coalescing producing larger gas structures, which are not spherical anymore. The Eötvos number is a measure for the deformability of the bubble, based on the ratio of gravitational forces to surface or interfacial tension forces. When the Eötvos number is less than one ($Eo << 1$), it implies that the flow is only weakly dependent on gravitational forces, whereas a greater than one

value (Eo >> 1), implies that the gravitational forces dominate over interfacial forces. Bubbly flow is expected to occur until a maximum void of 30%.

If the bubble sphere equivalent diameter exceeds about 60% of the pipe diameter, the dependability on its motion is no longer controlled by the equivalent spherical diameter, but instead by the width of the pipe (D_T). The smaller the diameter of the pipe, the higher the probability of obtaining plug-like bubbles with its characteristically bullet-shaped nose. This is known as the slug flow regime, and the maximum void fraction in this flow pattern is between 30% and 80%, without vapor in the near cells to the walls.

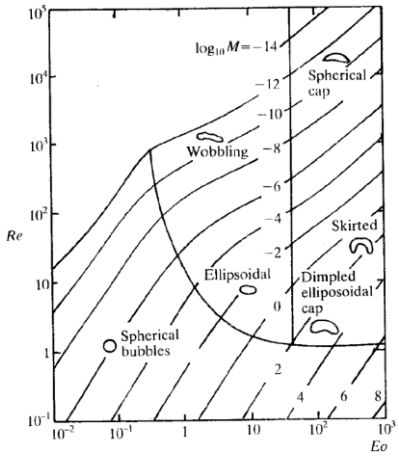

Fig. 2.2 Reynolds, Eötvos, and Morton numbers for single rising bubbles (Bhaga, 1981).

$$Re = \frac{\rho_l |V_g - V_l| D_p}{\mu_l} \tag{2.1}$$

$$E_o = \frac{g(\rho_l - \rho_g){D_p}^2}{\sigma} \tag{2.2}$$

$$M = \frac{g{\mu_l}^4(\rho_l - \rho_g)}{{\rho_l}^2\sigma^3} \tag{2.3}$$

As the mass flow rate increases, and the fraction of gas in the pipe surpass about 80%, disturbance waves alongside with a gas core start appearing. This regime is known as annular flow. In the annular regime, the liquid phase accumulates on the walls of the pipe, while the vapor phase and any entrained liquid tend to gather on the open regions where velocities are higher. Different subdivisions exist in this flow regime, such as ideal annular flow. In the aforementioned case, it is assumed that no entrainment of the liquid phase exists, and a smooth, symmetric liquid-gas interface is expected. This does not occur in reality, but it is commonly used for analytical studies (Whalley, 1987). For large liquid flow rates a further regime, known as wispy annular occurs, and it is characterized by the entrained liquid flowing in large agglomerates.

When increasing the diameter of the pipe in the slug flow regime, large bubbles become unstable and the flow regime becomes much more chaotic. This flow pattern is known as churn-turbulent flow regime, and it is characterized by an intense coalescence and break-up, which allow the appearance of a wider bubble size distribution. The largest bubbles churn through the liquid, and the non-uniform radial distribution of void fraction produce bulk liquid circulation.

Shaikh and Al-Dahhan (2007) characterized the churn-regime based on its proportionality to the superficial gas velocity ($\alpha \propto j_g^n$). While in bubbly flow, this relationship is almost linear (n = [0.8, 1]), in churn-regime the linearity between the overall gas holdup and the superficial gas velocity is lost (n = [0.4, 0.6]). Another way of characterizing this flow regime instead, is analyzing microscopic structures from which the previously mentioned macroscopic parameters are derived. There have been many attempts at capturing the instantaneous flow behaviors through energetic temporal signatures such as pressure fluctuations (Nishikawa, 1969; Matsui, 1984; Drahos et al., 1991; Letzel et al., 1997; Vial et al., 2001; Park and Kim, 2003), local holdup fluctuations using resistive optical probes (Barkshi et al., 1995; Briens et al., 1997), temperature fluctuations using a heat transfer probe (Kikuchi et al., 1997), conductivity probes (Zhang et al., 1997); and sound fluctuations using acoustic probes (Holler et al., 2003; Al-Masry, 2005; Al-Masry and Ali, 2007). For example, Fig. 2.3a and 2.3b, presents typical pressure signals in bubbly and churn-regimes obtained in a 0.376 m diameter bubble column at ambient conditions (Park and Kim, 2003).

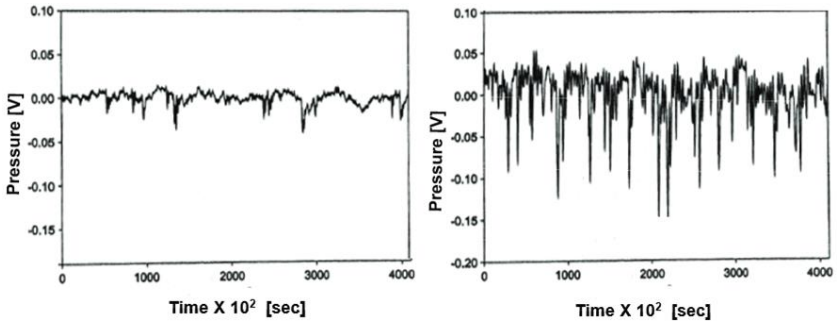

Fig. 2.3 Pressure fluctuations signals in A) bubbly flow and B) churn-turbulent flow regime (Park and Kim, 2003).

Commonly, time-series analyses are used in order to interpret these fluctuations and to identify the proper flow regime, for example statistical analysis, autocorrelation analysis, stochastic modeling, spectral analysis, chaos analysis, and wavelet analysis. The problem with point measurements is that, while they are in principle less intrusive than other methods like for example wire mesh sensors, they can only measure cord length and not bubble sizes. Still, Ellis et al. (2004) have shown the significant effect that the probe may have in the hydrodynamic of the flow.

More advanced, and less intrusive techniques exists such as Particle Image Velocimetry or PIV (Chen et al., 1994; Lin et al., 1996), Laser Doppler Anemometry or LDA (Olmos et al., 2003), or

wiremesh sensor analysis (Lucas et al., 2010). The wiremesh sensors analysis (WMS) allows the determination of bubble size distributions.

A way to analyze the distinctive flow regimes based on different flow parameters, are the flow regime maps. There are two basic classifications of these maps: empirical flow maps, which are commonly fitted to the database of the observed flow pattern, and theoretical or semi theoretical flow maps, where the transitions are predicted from the physical models of the flow phenomena. Theoretical or semi-theoretical flow-pattern maps are developed taking into account the flow structure and, sometimes, they are related to heat transfer mechanisms and diabatic characteristics. Usually only two parameters are taken into account to define a coordinate system on which the boundaries between the different flows patterns are plotted, like for example, the superficial gas and liquid velocities. Transition boundaries are then proposed to distinguish the different flow regimes as it would be done with a classical map.

The problem with the flow maps arises since the transition from bubbly to churn-turbulent flow and from slug to churn depends at the same time on a number of parameters such as superficial gas velocity, pipe diameter, liquid and gas phase properties, and distributor design (Urseanu, 2000). Presently, there is no flow map that can cover such a wide range of conditions. For example, Fig. 2.4a, shows one of the few approximate flow maps of transition velocity versus column diameter which distinguish among bubbly, transition, churn-turbulent, or slug flow (Shah et al., 1982). Still this map is limited to low viscosity systems at ambient conditions. Fig. 2.4b, shows another map, which distinguishes between discrete and dispersed bubbles, slug, churn, bridging, and annular flow (Zhang et al., 1997). This map was proposed for air-water system at ambient conditions, but it is limited to small diameter pipes (DT < 0.0826 m).

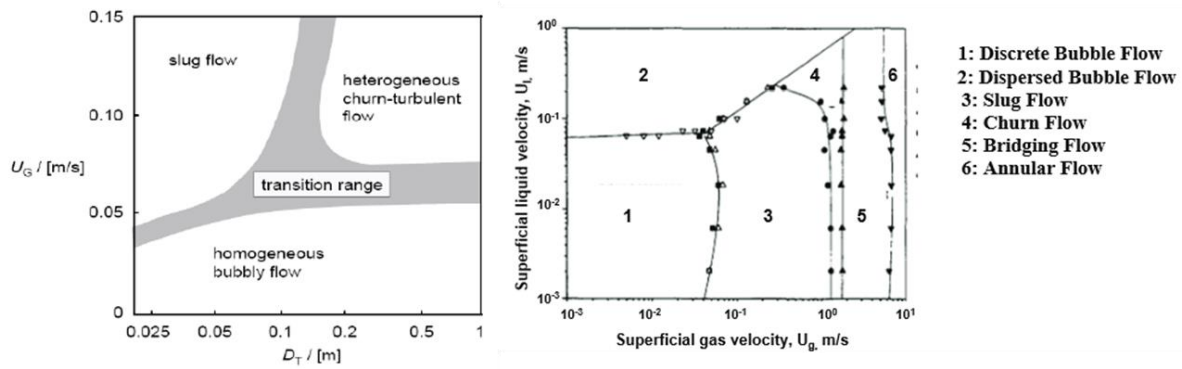

Fig. 2.4 Flow regime maps for air-water system at ambient pressure by A) Shah et al., (1982) and B) Zhang et al. (1997).

2.1.2 Transitions

When increasing the gas velocity, and for a pipe with a large diameter (D_T > 0.1 m), a direct transition from bubbly to churn-turbulent flow is expected. The major phenomenon causing this

transition is the occurrence of large bubbles due to coalescence mechanisms. When the diameters is less than 0.1 m, a clear transition from bubbly to churn-regime does not occur, instead slug flow appears after the homogeneous pattern, characterized by the typical Taylor bubbles with entrained small bubbles in their wakes.

In many occasions, the churn-regime has been confused with slug flow. Barbosa et al., (2001) highlighted this fact by explaining that the term "churn" has been generally used in two contexts. Zuber and Findlay (1965) defined the churn turbulent flow regime as that which allows specific forms of the drift-flux model to be used over a certain range of gas and liquid velocity, while Taitel et al. (1980) has defined it as a form of developing slug flow; the longer the pipe, the more likely the flow was to correspond to classical slug flow rather than to a flow with apparently churning motion. While the use of the classical definition of Zuber and Findlay is generally recommended, for large-size channels the churn-regime appears to be more of a developing slug-flow where the large diameter does not allow the full formation of the typical Taylor bubbles for certain gas velocities. For these large diameter pipes, there have been reports that slug flow could also occur by increasing the ratio of gas to liquid flow rates to about 12.8 (Parvareh et al. 2010). For small-diameter pipes, on the other hand, the churn-regime occurs after the breakdown of slug flow as the velocity of the gas increases (Hewitt and Hall-Taylor, 1970).

Other definitions of the transitions from slug to churn-flow include the ones by Nicklin and Davidson (1962), Wallis (1962), McQuillan and Whalley (1985) and Govan et al. (1991) who attributed the transition to local flooding of the liquid film falling by gravity around the Taylor bubble, and flowing in counter-current to the gas. Mishima and Ishii (1984), on the other hand, attributed the transition to the reduction of the liquid slug length which would lead to a strong wake effect of the Taylor bubble and the destabilization and destruction of the slug itself. Jayanti et al. (1993) accepted the first theory as the most plausible for the slug-churn transition and developed a model based on this proposal of local flooding inside the slug-bubble, reporting a good prediction of experimental data including the effect of pressure changes on the channel. The second definition is true mostly for low liquid superficial velocities, where the liquid film flowing in counter-current is strong enough to produce such effect.

More recently, several experimental studies on differentiation for the transition between slug and churn-turbulent flow depending on the pipe diameter, have been made at the TOPFLOW experimental facility in the Helmholtz-Zentrum Dresden-Rossendorf (HZDR). In Fig. 2.5a, the different flow patterns obtained for a 50 mm nominal diameter channel can be observed, and in Fig. 2.5b, for a 200 mm nominal diameter pipe. At the same superficial gas velocities at which the slug flow is present for the DN50 pipe, a churn-turbulent flow regime can be observed for the DN200 channel. This is even clearer when the bubble size distribution of the fully developed flow is observed in Fig. 2.6, alongside with the reconstruction of the wire-mesh sensor data in the axial direction. From these

figures, it is evident that the main difference between churn-turbulent and slug flow is that the regular structure of Taylor bubbles, including the liquid film alongside such bubbles gets lost, and a rather distorted shape of the largest bubbles is observed. The general structure of the bubble size distributions, however, remains similar.

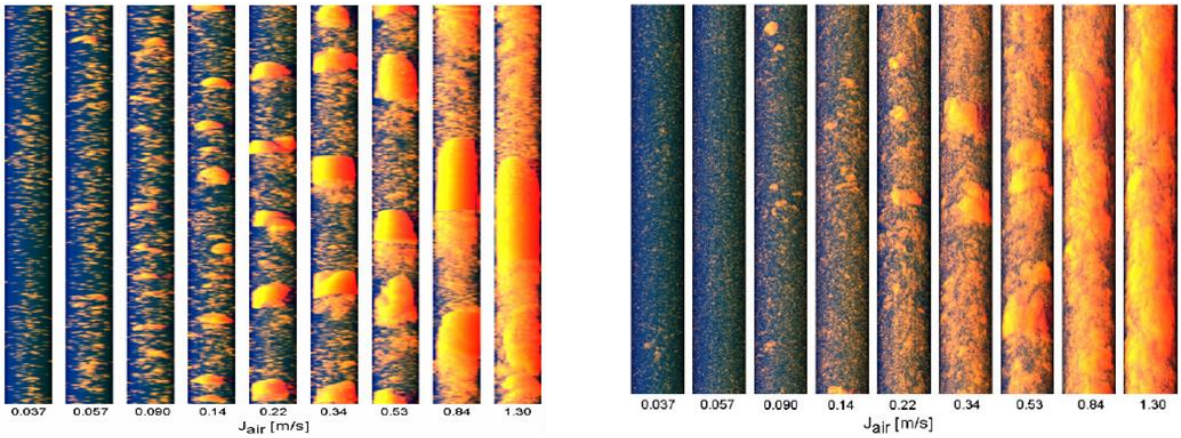

Fig. 2.5 Virtual side projections of the void distribution in the A) DN50 and B) DN200 test sections with J_{water}=1 m/s. (Prasser et al., 2007).

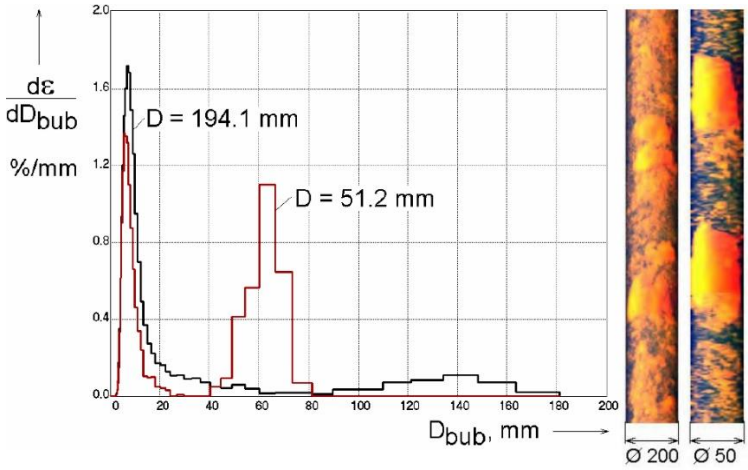

Fig. 2.6 Comparison of bubble size distribution in DN50 and DN200 test sections for an air flow rate typical for slug flow in pipes of small diameter
J_G = 0.534 m/s, J_L = 1.017 m/s.

Depending on the pipe diameter, a transition to the annular regime occurs after slug or churn-flow. Annular and churn-flow regimes counts with an averaged maximum void at the center of the channel and a liquid layer near to the wall (Hewitt et al., 1985). Due to the presented similarities, and like the slug flow, there is confusion about the differentiation between churn and annular flows. Researchers such as Nicklin and Davidson (1962) have given the name of semi-annular flow to the churn-regime in order to recognize its annular nature.

For small diameter pipes, for example, a direct transition between churn and annular regime is based on the breakdown of the slug flow. This is followed by a very rapid increase in the pressure

gradient due to an intensified wave activity and friction. This could be observed from Owen and Hewitt (1986) where the transition points between these flows regimes were illustrated, based on the dimensionless gas velocity (see Fig. 2.7).

$$j_g^* = j_g \left[\frac{\rho_g}{g D_T (\rho_l - \rho_g)} \right]^2 \tag{2.4}$$

Where, j_g is the superficial gas velocity, g is the acceleration due to gravity, D_T is the diameter of the tube, and ρ_l and ρ_g are the liquid and gas densities, respectively. In Fig. 2.7, p is the absolute pressure and $\dot{m}_l$ is the liquid mass velocity (mass flow rate per unit cross-sectional area). For $j_g^* \geq 0.4$, the pressure gradient decreases when increasing gas flow rate while the liquid flow rate stays constant due to the decreasing intensity of the gas-liquid interaction. After a while, the pressure gradient begins to increase again as the annular flow regime begins.

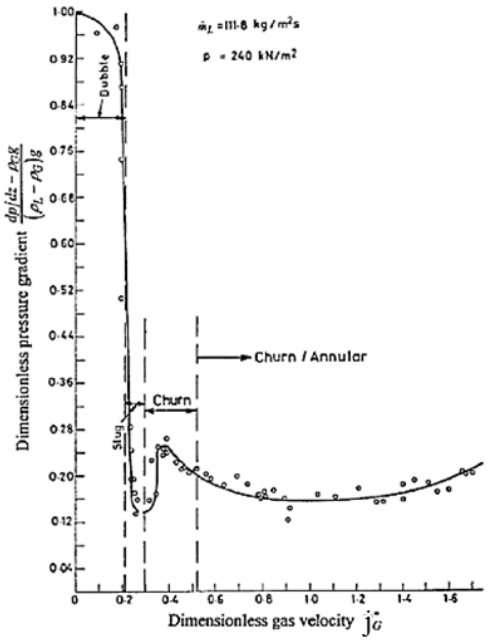

Fig. 2.7 An example of the pressure gradient distribution against dimensionless gas velocity for gas-liquid flow in vertical pipes (Owen and Hewitt, 1986).

Like in the case of the transition between slug and churn-turbulent flow, Hewitt et al. (1985) intended to explain the mechanism in the churn regime by visualization experiments. It was reported that the liquid is transported upwards in large waves. These waves picked up both, the liquid from a falling film ahead of them and shed liquid from a falling film behind them (see Fig. 2.8). The origin of these large waves are said to be similar to those which cause the flooding phenomenon in counter-current gas-liquid flow. Later on, other researches such as Govan et al. (1991) further proved such connection from experimental data.

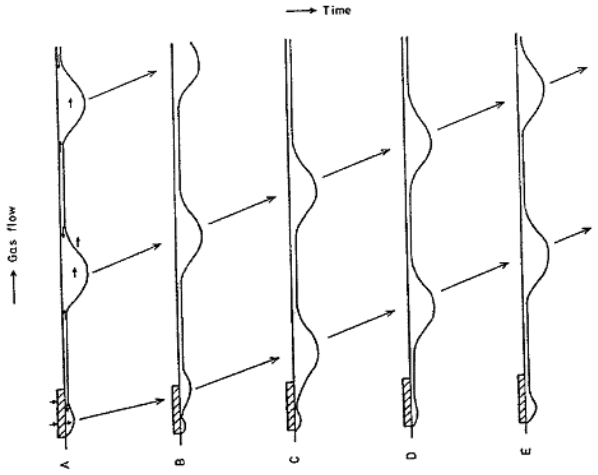

Fig. 2.8 Postulated mechanism of churn flow (Hewitt et al., 1985).

The flooding wave's theory indicates that, eventually, these structures will breakup to form droplets as they move across the channel, and a large fraction of the liquid is entrained as these droplets. Wallis (1962) illustrated (see Fig. 2.9) how the entrained fraction decreases with increasing gas velocity in what is clearly churn-flow up to a minimum value before increasing again in an annular regime. When downwards co-current flow is considered instead, the flooding type waves are not produced and the entrained fraction goes smoothly to zero as the gas flow rate decreases.

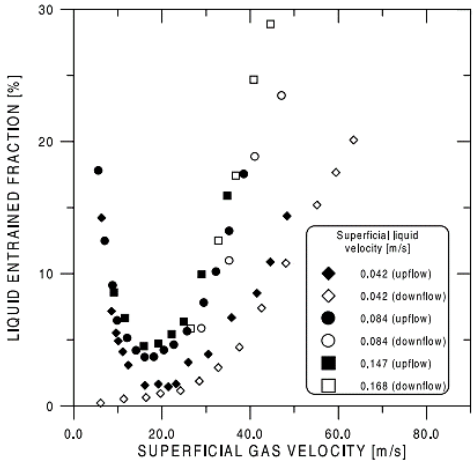

Fig. 2.9 Comparison of entrained fraction in upwards and downwards co-current annular flow (Wallis, 1962).

2.2 Status on the modeling of churn-turbulent flows

2.2.1 Analytical models

Krishna et al. (1993), and Ellenberger and Krishna (1994) used analogous behaviors between gas-liquid bubble columns and gas-solid fluidized beds in order to describe the gas volume fraction in terms of small and large bubbles gas fields. Their proposal was based on the velocity of the gas in the transition regime from bubbly to churn-turbulent flow. They proposed a so-called mean-bubble

approach for the description of the bubble sizes on the modeling of churn-regimes. This gave rise to a complete empirical model for churn-regime by Krishna et al. (2001). They made reference to this average size of large bubbles for air-water systems and calculated it as in Eq. 2.5.

$$D_b = 0.069(j_g - j_{g,trans})^{0.376} \tag{2.5}$$

Krishna et al. (2001) showed an improvement on their theory of single-size bubble diameter, by introducing a two-bubble class concept. They established a single size for small bubbles of 4 mm, and recommended to use the Harmathy (1960) correlations for the calculation of their rise velocity (see Eq. 2.6).

$$V_{b,small} = 1.53\left(\frac{\sigma g}{\rho_l}\right)^{0.25} \tag{2.6}$$

For the large bubbles, a series of correlations were proposed by Krishna et al. (1999), introducing an acceleration factor AF into the Collins (1967) equation for the rise of a single spherical cap bubble. The expressions developed for the large bubble size and acceleration factor for air-water systems are summarized from Eq. 2.7 to Eq. 2.11. These are also used for the drag coefficient proposed by Krishna et al. (1999). Eq. 2.7 represents the velocity of large bubble swarms, and Eq. 2.8 shows the acceleration factor. The correlations presented in Eq. 2.9, Eq. 2.10, and Eq. 2.11 represent the scale factors.

$$V_b = 0.71\sqrt{gD_b}(SF)(AF) \tag{2.7}$$

$$AF = 2.73 + 4.505(j_g - j_{g,trans}) \tag{2.8}$$

$$SF = 1 \quad for\ \frac{D_b}{D_T} < 0.125 \tag{2.9}$$

$$SF = 1.13e^{\left(-\frac{D_b}{D_T}\right)} \quad for\ 0.125 < \frac{D_b}{D_T} < 0.6 \tag{2.10}$$

$$SF = 0.496\sqrt{\frac{D_T}{D_b}} \quad for\ \frac{D_b}{D_T} > 0.6 \tag{2.11}$$

Finally, all the empirical modeling allows them to arrive to the conclusion that when using the superficial gas velocity at the regime of transition for air-water operations at $j_g \leq j_{g,trans}$, a homogeneous bubbly flow regime is generally the one that prevails. When this happens, the only two

phases that appear in the system are small bubbles and liquid. For churn-turbulent operations at $j_g > j_{g,trans}$, the complete three phase model must be invoked. Krishna and Ellenberger (1993) considered that in the churn-turbulent flow regime the superficial gas velocity through the small bubble phase was $j_{g,trans}$. The remainder of the gas ($j_g - j_{g,trans}$) was taken to rise up the column in the form of large bubbles. This means that at the inlet boundary, the large bubbles constitute a fraction ($j_g - j_{g,trans}$) / j_g of the total incoming volumetric flow, whereas the small bubbles constitute a fraction ($j_{g,trans}/j_g$) of the total incoming flow. As a conclusion, Krishna et al. (1999) defined $j_{g,trans}$ as a model parameter whose choice has a significance increasing effect on the small bubble holdup, but its influence on the center-line velocity is negligible.

While this is certainly an interesting approach for describing the transition to churn-regime from the homogeneous flow, its applicability is very limited, since as with all empirical models, it strongly depends on the experimental conditions for which it was proposed.

2.2.2 "1D" approaches: System codes and subchannel analysis

The computational models for flow analysis can be subdivided into three major categories: 0D, 1D, and 3D (including 2D simplifications). The first category is the 0D, where properties are averaged over the total volume, and no spatial information is available. These approaches are widely used for the modeling of valves, cylinders, pipe junctions, among other related systems (Blumberg et al., 1979; Mattavi et al., 1980; Heywood, 1980).

On the other hand, one-dimensional codes are often used for pipe flow. These codes are used in the nuclear and oil industries to model large systems such as heat exchangers, pressurizers, and the reactor vessels. ATHLET (ATHLET Overview, 2012; Mayinger et al., 1993; Vijayan et al., 1995), RELAP (RELAP5 Code Manual, 1995; Pokharna et al., 1997; Tiselj, 1996), TRACE (Murray, 2007; TRACE v5.0 Theory Manual, 2014; TRACE v5.0 Assessment Manual), RAMONA (Boure, 1973; Manera, 2005), and CATHARE (Robert, 2003; Emonot, 2009) are among such codes. CATHARE, RELAP, TRACE, and ATHLET, are among the system codes which are widely used for analysis of nuclear reactor simulations under steady state and accidental transient operations (Bestion, 2010). The development of theses codes included extensive validation and verification that highly benefited from the nuclear reactor safety programs carried out in the 1970's and 80's. (Bestion, 2002).

System codes make a number of simplified assumptions to the fundamental thermal hydraulic equations in order to perform with low computational cost. This was a limiting factor for effective transient simulation of reactor systems until the 1990s. While most of these codes have achieved a very high level of maturity, one of their greatest limitations is its empirical nature. In order to predict a wide range of accidental transients for PWRs and BWRs within a reasonable margin of error, choosing the correct models, code options, numerical methods, and nodalization details is essential.

All this is generally based on experienced user judgment and available experimental database in support of the particular simulation.

In terms of multiphase flow modeling, the current system codes use the two-fluid model with algebraic empirical formulations of the constitutive laws which describe the interfacial and wall-to-fluid processes. However, they are highly limited by the strong degree of empiricism and lack of dynamical modeling of the interfacial area and flow regime transitions. Eventually, system codes were developed to use 3D models which improved the spatial analysis. Still, this approach was limited by the lack of sufficient spatial discretization as well as other closure relations such as turbulence models.

While the latest versions of system codes, such as RELAP5-3D, include the ability to model transverse momentum components, it is still limited to large systems. This is due to its compatibility with only coarse nodalization. This becomes restrictive in modeling the complex structures present in the bottom of reactor vessels where high flow resolution needs to be resolved. The latest system codes also could have the ability to utilize the Reynolds-averaged Navier-Stokes (RANS) model for turbulence, but the Reynolds stresses and heat fluxes are still neglected. That means that only a mean flow is present, and that the high-frequency fluctuations are negligible. This last statement is known to be completely false for highly-turbulent flows where transient turbulence fluctuations are present.

In order to resolve the transverse momentum (e.g. cross flow) in nuclear reactor cores with higher level of accuracy, sub-channel analysis codes are used in the nuclear industry. VIPRE-01 (Stewart et al., 1989) and Cobra-IV (Wheeler et al., 1976) are two examples of LWR Subchannel codes (Sosnovsky, 2014). The sub-channel analysis codes solve the 1.5D momentum and energy equation in the direction of the flow and are able to resolve individual pins in the core and fuel assemblies. However, this subchannel analysis codes do not resolve the radial flow distributions within the subchannels and are limited to loss coefficients when modeling spacer grids or mixing vanes. Within the class of subchannel analysis models, three field models are commonly utilized for better simulation of boiling in the subchannels. The three fields are continuous liquid, continuous gas and dispersed liquid. The main motivation behind this is to mechanistically model the depletion of the liquid film in annular flow regime. However, such models still use many empirical closures and lack sufficient spatial resolution to model the flow geometry changes such as effect of spacer grids on the flow.

These limitations based on both 1-D and 3-D systems and subchannels codes, brought the need of a new generation of codes that are able to implement new closures while coupling with microscopic and macroscopic models, whether thermal-hydraulics, neutron-kinetics, fuel thermo-mechanics, or structure mechanics. This motivation gave rise to codes such as the NEPTUNE multi-scale thermo-hydraulic code, and increased the use of CFD tools for certain nuclear reactor issues related to turbulent mixing, Pressurized Thermal Shock (PTS), and others.

2.2.3 CFD modeling

As shown before, churn-turbulent flows are characterized by 3D gas distributions where both, spatial effects and correct bubble sizes need to be considered for an accurate representation of the flow. These characteristics can only be represented by CFD codes, where the nature of the flow is three-dimensional.

Direct Numerical Simulation (DNS), due to its extreme computational cost, is limited to the modeling of reduced computational domains, and has the potential to offer extremely valuable insights to the understanding of the underlying physics. While successful applications exist for the two extremes of bubbly and annular flow regimes (Tryggvason et al., 2001; Bolotnov et al., 2011; Fukano and Inatomi, 2003), the computational challenges have not yet allowed simulating churn-turbulent flow regimes. This is related to the still open challenge for the numerical methods to correctly resolve the interface interaction (break-up and coalescence) and to the extreme computational requirements necessary to resolve a large distribution of interfacial scales and turbulent scales.

The next possible approach is known as mixture modeling. This approach is based on the fact that only one momentum equation is solved where both phases share one velocity field, with or without resolution of the sharp interface. Some examples of this category that have been used for the modeling of churn-flow are the volume of fluid (VOF) model, and the algebraic slip mixture (ASMM) model. While the ASMM shares the concept of different velocity fields and slip velocity with the Euler-Euler approach, it is still considered as part of the Eulerian approach. This is due to the resolution of only one momentum equation. Consequently, the relative velocities are introduced only as an algebraic empirically derived equation.

The VOF model is based in a surface-tracking technique applied to a fixed Eulerian mesh. In this model, a single set of momentum equations is shared by the fluids, and the volume fraction of each of those fluids in each computational cell are tracked through the domain. The VOF approach has been used in the field of modeling churn-turbulent flow regime for the description of the wave theory explained earlier in this review. Because of the constant tracking of the gas-liquid interface motion and deformation, the volume of fluid has no need of assuming the shape of the wave a priori unlike other methods like, for example, the one used by Jayanti et al. (1996). The limitation of the VOF approach is mainly related to the need to explicitly resolve the interface, and the consequence that interfacial scales which are not significantly larger than the mesh size are simply discarded.

There have been different attempts at simulating churn-turbulent flow using VOF based on the previously discussed churn-turbulent travel wave theory. Da Riva et al. (2009), used air-water and liquid-vapor equilibrium mixture for R134a under adiabatic conditions to simulate vertical churn-turbulent pipe flow. They reported satisfactory results when compared against experimental data

regarding the frequency of formation of the ring-type waves typical of churn-flow. They also found that increasing the dimensionless gas velocity flatters the gas-liquid interfaces and that the superficial liquid velocity has a strong effect on the distribution of the two phases. Additionally, when R134a was used, there was an appearance of small amplitude waves at the vapor-liquid interface, which was not present before. Parvareh et al. (2010) also use the main VOF PLIC algorithm from FLUENT but within a 3D grid. They reported good results, but there is very little information about the numerical models that they used (e.g. turbulence approach), and the results are only compared qualitatively and very generally to Electrical Resistance Tomography (ERT) experimental data, also by the same author.

On the other hand, the algebraic slip mixture model assumes both phases as interpenetrating continua, instead of specifically tracking its interface. The volume fraction from both phases in a specific control volume can therefore be equal to any value between 0 and 1, depending on the space occupied by either phase. Moreover, the algebraic slip mixture model allows two phases to move at different velocities. This approach is based on the resolution of the continuity equation for the mixture phase, the momentum equation for the mixture phase, the volume fraction equation for the secondary phase, as well as an algebraic expression for the relative velocity. Still, the ASMM model cannot be justifiable over the Euler-Euler approach which considers a much more consistent calculation of phase velocities instead of using an algebraic correlation.

Chen et al. (2009) evaluated the use of the ASMM model along with a bubble population balance equation (BPBE). By using the BPBE, Chen eliminated the assumptions of a single bubble size, and improved the gas holdup prediction. Their results were compared against experimental data from Radioactive Particle Tracking (CARPT) and Computed Tomography (CT), which allow validation of velocities and void profiles. They reported good estimations for every flow regime but churn-turbulent flow. In this regime, there was an overprediction of the axial velocity profiles, as well as an unrealistic void profile with maximum away from the centerline of the column. This comes as a consequence not only from the algebraic calculation of the slip velocity, which assumes that the phases are in local equilibrium over short spatial length scales, but also from the poor selection of submodels which were used.

A summary of the most important flow and numerical conditions from the aforementioned calculations can be found in Table 1.

The Euler-Lagrange approach, in turn, is based on the resolution of acceleration, velocity and position when applying external forces to the particles. This method becomes problematic when very large particles, such as the gas structures found in churn-turbulent and slug flow, need to be handled. The Eulerian-Eulerian approaches are able to overcome such computational burdens at a cost of averaging the dispersed structures.

Table 2.1 VOF and ASMM modelling summary.

Published Work	Flow Conditions	Numeric Conditions
Chen et al. (2009)	Adiabatic gas-liquid bubbly and churn-turbulent flow / Pseudo-two-phase air-Therminol-Glass beads. Air-Water. Vertical bubble column flow.	ASMM with BPBE. Continuum surface force (CSF) by Brackbill et al. (1992) inherent from FLUENT. RNG $\kappa - \varepsilon$ with standard wall functions. 2D Axisymmetric with 80000 cells.
Da Riva et al. (2009)	Adiabatic gas-liquid churn-turbulent flow. Air-Water / Liquid-Vapor R134a. Vertical pipe flow.	VOF using piecewise linear interface calculation (PLIC) scheme. Continuum surface force (CSF) by Brackbill et al. (1992) inherent from FLUENT. RNG $\kappa - \varepsilon$ with standard wall functions. 2D Axisymmetric mesh with 80000 square cells.
Parvareh et al. (2010)	Adiabatic gas-liquid oscillating churn regime, plug, and annular flow. Air-Water. Vertical and horizontal pipe flow.	VOF using piecewise linear interface calculation (PLIC) scheme. Continuum surface force (CSF) by Brackbill et al. (1992) inherent from FLUENT. 3D mesh with different grids between 168249 and 1034823 cells.

Finally, in the Euler-Euler modeling approach, each phase is considered as continuum (including the fields that derived from the phases), which can interpenetrated with the other fluid fields. Several averaging methods are used to formulate the governing equations. For adiabatic flows the Eulerian model solves momentum and continuity equations for each of the phases, and the equations are coupled through pressure and exchange coefficients.

For each considered phase *k*, the volume – averaged mass and momentum conservation equations in the Eulerian framework are given by the correlations Eq. 2.12 and Eq. 2.13. This set of equations are specified for adiabatic flows.

$$\frac{\partial(\alpha_k \rho_k)}{\partial t} + \nabla \cdot (\rho_k \alpha_k \mathbf{V}_k) = m_k''' \tag{2.12}$$

$$\frac{\partial(\alpha_k \rho_k \mathbf{V}_k)}{\partial t} + \nabla \cdot (\rho_k \alpha_k \mathbf{V}_k \mathbf{V}_k) = -\alpha_k \nabla \mathrm{p}_k + \nabla \cdot \left(\alpha_k \underline{\tau}_k\right) + \rho_k \alpha_k \mathbf{g} + \sum_{\boldsymbol{j}} \mathbf{M}_{kj}^{i} + \sum_{\boldsymbol{m}} m_{m,k}''' \mathbf{V}_{\boldsymbol{m}}^{\boldsymbol{i}} \tag{2.13}$$

Where $m_k''' = \sum_m m_{m,k}'''$

In the aforementioned equations, α_k represents the volume fraction of the field-*k*, while $m_{m,k}'''$ is the volumetric mass transfer term from other fields which represents the same phase. In case of not considering mass transfer, this term will be equal to zero. The term $\underline{\tau}_k = \underline{\tau}_k{}^{\mu} + \underline{\tau}_k{}^{Re} = \mu_k\left(\nabla \mathbf{V}_k + \nabla \mathbf{V}_k{}^{\boldsymbol{T}}\right) - \frac{\mathbf{2}}{\mathbf{3}}\mu_k \nabla \cdot \mathbf{V}_k \boldsymbol{I}$ is the total shear stress term. The variable $\mathbf{M}_{kj}^{i}$ represents the interfacial momentum transfer per unit time between two different fields.

For adiabatic flows without any kind of transfer including bubble breakup and coalescence, Eq. 2.13 will be simplified into equation Eq. 2.14.

$$\frac{\partial(\alpha_k \rho_k \mathbf{V}_k)}{\partial t} + \nabla \cdot (\rho_k \alpha_k \mathbf{V}_k \mathbf{V}_k) = -\alpha_k \nabla \mathrm{p} + \alpha_k \nabla \cdot \underline{\tau}_k + \rho_k \alpha_k \mathbf{g} + \mathbf{M}_k^{i} \tag{2.14}$$

The compatibility condition for the coupled solver equation set is expressed as Eq. 2.15.

$$\sum_{k=1}^{n} \alpha_k = 1 \tag{2.15}$$

Where n represents the number of fields.

The usefulness of a multi-field model for the prediction of gas-liquid two-phase flow in vertical tubes, not only for the regimes such as churn-turbulent and slug flow but also for the transition between them, has been emphasized by many researches including Stevanovic et al. (2007).

In order to complete these equations for the case of churn-turbulent flows, appropriate closure models are required for the interfacial forces, liquid phase turbulence, and bubble coalescence and breakup. The turbulence of the gas, can usually be neglected due to the low density of this phase.

2.2.4 Mechanistic models for interfacial forces

Due to the averaging of the conservation equations, most of the information is lost, but must be reintroduced by the use of closure relations. The closure laws objective is to account for the mass and momentum transfer between the different fields and phases while providing the functional form expected for the interfacial forces. The present models are limited by the need of local condition

dependent coefficients, derived from the fact that the closure laws have been developed for ideal bubbly flow, and are now being applied to churn-turbulent flow and slug conditions.

The different forces that interact at the interface of the flow can be divided into drag and non-drag components with their respective mechanistic models.

$$\mathbf{M}_{c,k}^{i} = -\mathbf{M}_{d,k}^{i} \tag{2.16}$$

In churn-turbulent flow, the non-drag forces which contribute to the momentum exchange at the interface include the lift force, the wall force, the turbulent dispersion force, and the virtual mass force. Other contributions such as the Basset force may be present but are neglected due to their small effect. The total force acting at the interface of the flow can be expressed as the superposition of several component forces.

$$\mathbf{M}_{k}^{i} = \mathbf{M}_{k}^{D} + \mathbf{M}_{k}^{VM} + \mathbf{M}_{k}^{TD} + \mathbf{M}_{k}^{L} + \mathbf{M}_{k}^{W} \tag{2.17}$$

In terms of the drag force (Eq. 2.18), it is very well-known that in the axial direction the drag force plays a major role in the hydrodynamic of the flow. Moreover, the drag force depends on the bubble-geometry that is being modeled, since when assuming ellipsoidal or spherical cap bubbles, the drags experienced in the vertical and horizontal direction are markedly different.

$$\mathbf{M}_{d,k}^{D} = \frac{3}{4}\alpha_{d,k}\frac{\rho_c}{D_b}C_{D,k}\left|\mathbf{V}_c - \mathbf{V}_{d,k}\right|\left(\mathbf{V}_c - \mathbf{V}_{d,k}\right) \tag{2.18}$$

The drag coefficient, $C_{D,k}$, is a dimensionless quantity which is used to model all complex dependencies on shape, inclination, and flow conditions on the hydrodynamic of bubbles and drops, and is an essential term in all drag force formulations. There are different models available for the formulation of the interphase drag coefficient which has been used in churn-turbulent flow calculations. The Schiller and Naumann (1935) correlation was said to be successfully applied to churn-turbulent flow by Chen et al. (2005). Still, this seems unlikely since this is a drag coefficient which is limited to spherical particles, and for that matter, should be unable to represent the changes on the force for churn-like and slug bubble shapes. Chen et al. (2009) uses the Grace (Clift et al., 1978) correlation instead, which consider the deformability of the bubbles based on the Eötvos and Morton number. There is also the Tomiyama (Takamasa and Tomiyama, 1999) drag coefficient which is based on a large number of experimental data, and it is well suitable for gas-liquid flows with bubbles of different shapes ($10^{-2} < Eo < 10^{3}$). It is a suitable correlation also for large range of Morton ($10^{-14} < Mo < 10^{7}$) and Reynolds numbers ($10^{-3} < Re < 10^{5}$) but despite of this, it has not been used for churn-regime in the literature.

Wallis (1969) made a relatively small modification in the exponent and the constant which multiply the Reynolds numbers for Reynolds lower than 1000 in the formulation from Schiller and Naumann (1935). Some researchers (Guillen et al., 2009; Tselishcheva et al., 2010) have used this method for the small bubbles in the churn-regime, while using Ishii and Zuber (1979) for the larger gas structures.

The Ishii and Zuber correlation has a relative important advantage over Schiller-Naumann, by considering the deformability of the bubbles using the Eötvos number for the ellipsoidal bubbles, and a different value for the cap particles. As with the Grace model, the Ishii-Zuber correlation is intended for the distorted bubbles. It has been reported that the Ishii-Zuber correlation, when applied to a churn-turbulent flow regime, significantly overestimates the drag coefficient so that one has to artificially increase the bubble size for simulations to match the observed flow data (Chen et al., 2005; Tsuchiya et al., 1997).

As long as bubbles move in a sparsely distributed manner, the drag coefficients discussed previously are applicable. In high void fraction regimes, this behavior is no longer correct, since as the gas velocities increase, there is a high possibility that a swarm of bubbles will start moving together. This can effectively decrease the drag force in a significant manner. While this is an effect known to occur, it is highly challenging to measure it experimentally, which increases the difficulty to differentiate among the quality of the large number of swarm corrections in the literature. Some drag corrections known to be used for churn-turbulent flows are the linear correction use by Chen et al. (2009), the mixture Reynolds correction for spherical bubbles used by Wallis (1969), and a modified version used by Ishii-Zuber (1979), the Eötvos multiplier correction for ellipse bubbles also used by Ishii-Zuber, and the volume fraction exponent correction which can be used for various shaped bubbles and it is used by Ishii-Zuber for large cap bubbles.

A turbulence volume fraction dispersion force is needed in order to account for the increased mixing due to the turbulence in a two-phase flow. There are different modifications of the turbulence dispersion force used for simulating churn-flow. For example, the Lopez de Bertodano et al. (1998) formulation, it is known for the difficulty of stablishing an appropriate turbulence dispersion coefficient. The Podowski (2009) modification of that force seems appropriate only for small bubbles. On the other hand, acceptable results have been obtained in the past (Montoya et al., 2013; Krepper et al., 2014) using the Favre Averaged Drag (FAD) model (Eq. 2.19) by Burns (2004).

$$\boldsymbol{M_c^{TD}} = -\boldsymbol{M_c^{TD}} = C_{TD} C_{D,k} \frac{v_c}{\sigma_c} \left(\frac{\nabla \alpha_d}{\alpha_d} - \frac{\nabla \alpha_c}{\alpha_c} \right) \tag{2.19}$$

The lift force (Eq. 2.20) is used to account for the interfacial momentum exchange between the bubbles and the liquid field due to aerodynamic lift. The effect of the lift force is to move the bubbles

towards or away from the pipe wall. It also acts on the bubbles in a perpendicular direction to the bulk flow when gradients of liquid velocity are present.

$$\boldsymbol{M}_{d,k}^{L} = -C_L \rho_c \alpha_{d,k} (\mathbf{V}_{d,k} - \mathbf{V}_c) \times (\nabla \times \mathbf{V}_c) \tag{2.20}$$

The lift arising from the deformation of the bubbles is dominant in the churn-regime but this is not taken into account in the present models. The current lift force and lift force coefficient formulations are limited by the conditions in which the experiments were made. For that matter and since most of the correlations for lift force have been developed mostly for bubbly flow conditions, they cannot accurately predict the lift effect on churn or slug gas structures.

The lift coefficient is an important dimensionless parameter of the lift force formulations which, as with the drag coefficient, is used to model all complex dependencies of shape and flow conditions on the hydrodynamics of bubbles and droplets. While there have been many recommendations for the value of this coefficient, the Tomiyama et al. (2002) correlation has been developed from a large range of experimental data. An important fact is that this correlation was developed while calculating the drag force with the Tomiyama drag coefficient correlation previously discussed, and they have been reported to work more accurately when used alongside.

The virtual mass force (Eq. 2.21) accelerates the flow around a bubble as it accelerates through the liquid (Guillen et al., 2009). The effect of the added mass can be seen only when high-frequency fluctuations of the slip velocity occur (Drew, 1983), but these high frequency velocity fluctuations are not resolved in the two fluid model, and are then lost in the averaging process. The large fast-rising bubbles, typical of churn-regime, do not have a close wake and so the concept of added mass is not applicable. On the other hand, the small bubbles do have a close wake, but in this regime these bubbles suffer strong recirculation, moving downwards near the wall region. The added mass contributions to the small bubbles would only lead to severe convergence difficulties. The virtual mass coefficient is specified by the user and is commonly taken to be around 0.5.

$$\boldsymbol{M}_{d,k}^{VM} = -C_{VM,k} \rho_l \alpha_k \left\{ \left[\frac{\partial \mathbf{V}_{d,k}}{\partial t} + (\mathbf{V}_{d,k} \cdot \nabla) \mathbf{V}_{d,k} \right] - \left[\frac{\partial \mathbf{V}_c}{\partial t} + (\mathbf{V}_c \cdot \nabla) \mathbf{V}_c \right] \right\} \tag{2.21}$$

The interfacial wall force (Eq. 2.22) accounts for the hydrodynamic impulse on a bubble traveling in close proximity to a solid wall. The effect of the wall force is generally observed as a sharp spike in the bubble void fraction near the wall that affects the small bubbles, and in a weaker manner also the larger bubbles (Guillen et al., 2009).

$$\boldsymbol{M}_{\boldsymbol{d,k}}{}^{\boldsymbol{W}} = -C_W \frac{D_b \alpha_k}{2} \left(\frac{1}{y^2} \right) \rho_c V_{rel}^2 \overrightarrow{n_r} \tag{2.22}$$

It is a well-known fact that both, the wall and lift forces, are responsible for the determination of the gas fraction in the region close to the wall. The respective wall coefficient can be calculated as proposed by Hosokawa et al. (2002) which is valid for both high and low Morton numbers provided that the bubble does not collide with the wall. This coefficient has been reported to produce acceptable results in the literature (Krepper et al., 2014).

All these closure laws were developed for single rising bubbles, but nevertheless have been used in calculations with much different conditions such as heterogeneous bubbly and churn-turbulent flow. Here, the assumption of the forces acting on a single rising bubble are far away from the real force contributions on each of the bubbles in the flow.

Bubble forces strongly depend on bubble sizes. A broad bubble size distribution in churn-turbulent flow should have a great influence on the drag and non-drag forces. Even in the case of bubbly flow, the momentum exchange between the liquid and the bubbles strongly depends on the bubble size. An example of this would be the sign change of the lateral lift force action on a bubble at a critical size, which leads to a de-mixing of small and large bubbles. Still, it has been observed that simulations with only two-fluid models are expected to have clear limitations since they take into account only the limit based on the change of lift, or the deformability of churn-like bubbles, but not both.

2.2.5 Turbulence modeling

The difficulty of studying turbulent flows lies in the range of length scales and the complexity of the phenomena. A classification of turbulent flows can be made based on the range of such length and time scales that are modeled and the ones that are resolved. Generally, in order to obtain a high quality solution, most of the turbulent scales should be resolved, but this will be directly linked to a finer resolution of the simulation, and for that matter also to higher computational costs. In general, all the existing methods for modeling turbulence developed for single phase flow (k-ε, Ri-ε, LES, etc.) have been extended to two-phase flow with a lower maturity and degree of reliability. Some information about this can be found in the ERCOFTAC (2011) document.

The RANS approach can be considered as the simplest, cheapest (in terms of CPU), the most advanced, and the most used available two-phase CFD method (Bestion, 2011). The RANS turbulence treatment for two-phase flow consists of applying an ensemble averaging or a time averaging, which filter all turbulent scales and all two-phase intermittency scales. Such an approach can only be used with steady and quasi-steady flows in the case in which for both, the largest time scales of turbulence and two-phase intermittency, the time scales of the variation of mean variables results to be larger. RANS is in principle compatible with all two-phase flow regimes provided that they are steady or quasi-steady. However, for slug and churn flow regimes with large bubbles (either Taylor bubbles in the case of slug flow, or distorted large bubbles in churn flow) the intermittency

due to the passage of these gas structures corresponds to rather large time scales. Since the RANS filters even these large scales, then it is not able to predict this intermittency. Still, most of the approaches for modelling the churn-turbulent flow regime so far are mostly based on this technique.

In high void fraction regimes, it is expected that inside the dispersed gas-field, the larger particles increase the turbulence in the continuous liquid phase. That happens due to the presence of wakes behind the respective bubbles. A series of successful predictions of bubble column operations under churn-regime when using bubble induced turbulence or BIT has been already reported by Pan and Duduković (2001). Sato and Sekoguchi (1975) were able to represent the particle induced turbulent phenomena using an enhanced continuous phase eddy viscosity. It is worth mentioning that this model was developed for bubbly flows. Therefore, it is not very accurate in the prediction of the particle induced turbulence for the churn or slug-regime where the turbulence produce by the bubbles would be certainly much higher than the expected in bubbly flows. Rzehak and Krepper (2012) presented a novel model for particle induced turbulence and compared it with others like the Sato enhanced turbulence approach, showing a better prediction with their proposed model. For this matter, a two equation turbulence approach with additional source term for the description of the bubble induced turbulence was adopted. While this model is still developed for turbulent bubbly flow and not churn-turbulent regime, it has been proved that it works better than the Sato model. Therefore, it appears to be a more adequate approach for modeling the particles inducing turbulence in the churn-regime.

2.2.6 Modeling of bubble coalescence and breakup mechanisms

One of the greatest challenges in modeling gas-liquid flow is the treatment of the coalescence and breakup of bubbles, and the effects of those phenomena on the species, energy, and momentum transport processes. The strong dependency of the mean motion of two-phase flow on the small-scale motion requires an understanding of the interaction, not only with the fluid that surrounds them, but also with each other. These interactions usually depend on the flow conditions, fluid properties, and geometry of the flow channel.

Based on the literature (Kim, 1999; Hibiki and Ishii, 2000; Fu, 2001; Hibiki et al., 2001; Sun, 2001; Ishii and Kim, 2004; Liao and Lucas, 2009; Liao and Lucas, 2010), the mechanisms for bubble breakup and coalescence expected to act on a two-phase flow regime can be classified into the following categories:

- Coalescence between the fluid particles due to random collisions driven by turbulent eddies.
- Coalescence between the fluid particles due to wake entrainment.
- Disintegration of the fluid particles caused by turbulent eddy impact.
- Shearing-off of small fluid particles at the rim of large cap, slug, or churn fluid particles.
- Breakup of large cap and churn-turbulent fluid particles induced by flow instabilities.
- Collision due to velocity gradient near the wall region.

- Collision due to different rise velocity of fluid particles in different sizes.
- Breakup caused by laminar viscous forces.

Typically, the possibility of collision among multiple (more than two) fluid particles is expected to be low in comparison with the binary collisions, making the last one the commonly reasonable model mechanism in these approaches. Wang et al. (2010) reported that for bubbly flow, only the three first interactions could be considered relevant. While for the churn and slug regime, the first five interactions are needed for a correct approach.

Many research works have established that once the transition regime is achieved, the coalescence increases sharply, greatly increasing the diameter of what could be considered as small and large bubbles. Once churn-turbulent flow is achieved, it is expected that the coalescence and breakup phenomena reach full equilibrium a couple of diameters above the inlet boundary.

The most established and used models that can be found in the literature for bubble breakup and coalescence are those of Prince and Blanch (1990), and Luo and Svendsen (1996). These series of models have been used in an important number of research papers as it was originally conceived, and also with certain modifications (Tselishcheva et al., 2010). None of these modifications on the original proposed mechanisms approaches seems to work very well in the prediction of high void fraction regimes. The lack of consideration of the full spectra of mechanisms for breakup and coalescence here, ask for a much more completed approach.

Finally, Liao et al. (2011) proposed a novel approach for the inhomogeneous multiple size group (iMUSIG) model. Their main objective was to consider a major number of important mechanisms presented in bubble breakup and coalescence in turbulent gas-liquid mixtures. For bubble coalescence they took into account coalescence due to turbulence, laminar shear, wake-entrainment, and eddy-capture. For bubble breakup they considered the effect due to turbulent fluctuation, laminar shear, and interfacial slip velocity. These models are still being tested, but have shown promising results.

2.2.7 Simulations based on multi-fluid approach

In churn-turbulent flow, bubble-bubble interactions result in widely distributed bubble sizes where the local mean bubble size in the core region is larger than in the wall region. In the core region of the pipe, gas holdup is higher while the dissipation rate is lower, which results in larger bubbles because of the higher coalescence rate and lower breakup rate. On the other hand, gas hold up is lower while the dissipation rate is higher in the wall region, which results in smaller bubbles because of the lower coalescence rate and higher breakup rate. As it has been stated in previous sections, most of the work that can be found in the literature considers, at least, a two gas-phase approach composed of large and small bubbles. One of the challenges in these calculations is to capture correctly the appropriate interfacial area density.

Modeling an accurate interfacial area density in problems regarding churn-turbulent and slug flow is important in order to predict the correct behavior of the defined drag and non-drag forces. Various approaches exist to model the interfacial area density by defining bubble size by empirical correlations in a large range of flow regimes. For churn and slug flow (intermittent flow between $0.25 < \alpha < 0.75$) for example, the Sun et al. (2003) correlation exists (Eq. 2.23).

$$D_b = 0.001(1309.5{\alpha_g}^3 - 2464.2{\alpha_g}^2 + 140.5\alpha_g - 210.05) \quad (2.23)$$

This is a correlation which has been known to be used by Sun et al. (2004) for studying various parameters such as the drag coefficients of two-group bubble data under churn and slug flow regime. As expected, this polynomial distribution made an accurate prediction for the specific experimental conditions at which the correlation was developed. As with most empirical correlations, using different hydrodynamic properties or fluid velocities could increase or decrease the strong coalescence expected during these flow regimes, rendering the approximation inaccurate.

On the other hand, bubble population balance approaches allow the definition of how populations of separate entities develop based on specific properties in time. Furthermore, the evolution of the bubble size distribution resulting from coalescence and breakup processes can be modeled by means of such population balance equations. Reports on using bubble population balance approaches for resolving churn-turbulent flow regime in pipe flows exist, such as with the Inhomogeneous Multiple Size Group (iMUSIG) in Montoya et al. (2013), and with less known approaches such as the one developed and used by Wang (2010). While final results varied, the advantages on the importance of defining different bubble classes for the correct resolution for the interfacial forces by accounting on different velocity fields and interfacial area density groups are clear.

Lo et al. (1996) originally proposed the algebraic multiple size group model in order to combine the adequate number of bubble size classes for the simulation of coalescence and breakup with the purpose of limiting the computational effort. The MUSIG model was originally developed by assuming that all size groups were moving at the same velocity, which restricted the applicability of the model to homogeneous dispersed flows.

Krepper et al. (2005), introduced the idea of using different velocity groups instead. Basically, the gaseous dispersed phase is divided into a number of N velocity groups (or phases), where each velocity group is characterized by its own velocity field. Then, the overall bubble size distribution is further represented by dividing the bubble diameter range within each of the velocity groups j into a number, M_j ($j = 1 \ldots N$), bubble sub-size fractions (see Fig. 2.10). The population balance model considers bubble coalescence and breakup that are applied to the sub-size classes. It means that the mass exchange between the sub-size groups can exceed the size ranges assigned to the velocity clusters (Krepper et al., 2009).

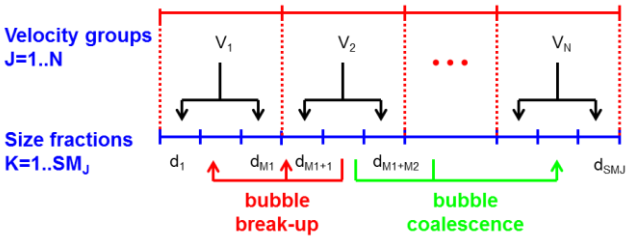

Fig. 2.10 Improvement of the polydispersed approach: the size fractions M_j are assigned to the velocity field V_j (Krepper et al., 2005).

The subdivision should be based on the physics of bubble motion for gas structures of different sizes, for example, dissimilar behavior of distinctively sized bubbles with respect to lift force. Extensive validation made by Krepper et al. (2007 & 2008), have shown that in most cases N = 2 or 3 velocity groups should be sufficient in order to capture the main phenomena, at least in bubbly regimes. One way to separate the different velocity field sub fractions would be to consider the variety of bubble shapes, and categorizing the velocity fields depending of such bubble geometries. In general, for gas-liquid two-phase flows, bubbles could be separated into five different categories such as spherical, distorted, cap, Taylor (slug), and churn-turbulent. Bubbles with different shapes are expected to have different behaviors and different characteristics in terms of drag, motion, and general interaction mechanisms.

Ishii and Zuber (1979) proposed three length scales: the spherical bubble limit (D_{ds}), maximum distorted bubble limit ($D_{d,max}$), and maximum cap bubble limit ($D_{c,max}$). They are defined as Eq. 2.24, Eq. 2.25, and Eq. 2.26.

$$D_{ds} = 4\sqrt{\frac{2\sigma}{g\Delta\rho}}\left(\frac{\mu_l{}^2}{\sqrt{\frac{\rho_l{}^2\sigma^3}{(g\Delta\rho)}}}\right)^{1/6} \tag{2.24}$$

$$D_{d,max} = 4\sqrt{\frac{\sigma}{g\Delta\rho}} \tag{2.25}$$

$$D_{c,max} = 40\sqrt{\frac{\sigma}{g\Delta\rho}} \tag{2.26}$$

Here, the maximum cap bubble limit is based on the Kelvin-Helmholtz and Rayleigh-Taylor instabilities. Many researches in the literature have proposed to use a two-group approach based on these correlations (Hibiki and Ishii, 2000; Ishii and Kim, 2004). In these works, they normally considered $D_{d,max}$ as the transition length scales between Group-1 and Group-2 bubbles, where small

spherical and distorted bubbles with a diameter less than $D_{d,max}$ fall into Group-1; whereas larger cap, Taylor, and churn-turbulent bubbles are categorized as Group-2 bubbles. When larger bubbles grow to such an extent that the bubble size exceeds $D_{c,max}$, they become unstable due to the interfacial instability along the leading nose of the bubble analogous to Kelvin-Helmholtz instability. Thus, bubbles having a size greater than $D_{c,max}$ cannot be sustained and will disintegrate into typically cap or churn-turbulent bubbles very quickly.

Finally, Wang (2010) implemented in his thesis a two-group Interfacial Area Transport Equation (IATE) formulation, and applied it to churn-turbulent flow conditions. The IATE method, instead of transporting an equation for the number density function of the bubbles, it predicts the interfacial area concentration as a function of space and time.

The theoretical interfacial area transport equation was derived from the fluid particle number density transport correlation, established by Kocamustafaogullari and Ishii (1995). In the flow regimes beyond bubbly conditions, the substantial differences in sizes and shapes of bubbles increase the complexity of the bubble interactions, requiring that the one-group IATE be extended to a two-group IATE model (Hibiki and Ishii, 2000; Fu, 2001; Sun, 2001; Fu and Ishii, 2003; Ishii and Kim, 2004; Sun et al., 2004b).

Wang (2010) reported that no satisfactory predictions of phase distributions for the churn-turbulent flow conditions were achieved. Still, the model implementation was able to qualitatively match the interfacial area concentrations. He recommended basing the future work on the turbulence model and interfacial forces in the momentum equations.

A summary of the most important flow and numerical conditions from previously discussed and more relevant calculations for Euler-Euler multi-fluid approach under churn-turbulent flow conditions can be found in Table 2.2.

Table 2.2 Multi-fluid modeling summary.

Published Work	Flow Conditions	Numeric Conditions
Sun et al. (2004)	Adiabatic gas-liquid bubbly, cap-turbulent, and churn-turbulent flow. Air-Water. Vertical pipe flow.	Theoretical Analysis (no validation). Separation between Group-1 and Group-2 bubbles based on the Ishii-Zuber maximum distorted bubble diameter. Bubble-bubble interaction mechanisms considered: coalescence by random collision, coalescence by wake entrainment, turbulence impact, shearing off, and surface instability.

		Group-2 bubble exists for sizes lower than $D_{c,max} = 40\sqrt{\frac{\sigma}{g\,\Delta\rho}}$.
Krepper et al. (2007) Krepper et al. (2008) Krepper et al. (2009)	Gas-liquid bubbly flow. Air-Water / Steam-Water. Vertical pipe flow (DN200 mm) with and without obstacle – TOPFLOW conditions. Relevant information as starting point for churn-turbulent calculations for Montoya et al. (2013).	Euler-Euler polydispersed approach. iMUSIG BPBE from CFX. SST κ – ω with automatic wall functions. 2D Axisymmetric mesh. Two gas-fields. Drag, lift, turbulent dispersion, wall lubrication, virtual mass, and bubble induced turbulence closure laws. Bubble breakup and coalescence (Luo and Svendsen, 2012; Prince and Blanch, 2012).
Guillen et al. (2009)	Adiabatic gas-liquid churn-turbulent flow. Air-Water. Vertical pipe flow (DN200 mm) – TOPFLOW conditions.	Euler-Euler polydispersed approach using NPHASE-CMFD. SST κ – ε with automatic wall functions. 2D Axisymmetric mesh with 40 x 500 cells. Two gas-fields with four bubble groups. Drag, lift, turbulent dispersion, wall lubrication, bubble induced turbulence, and virtual mass. - Bubble breakup and coalescence.
Tselishcheva et al. (2009)	Adiabatic gas-liquid churn-turbulent flow. Air-Water. Vertical pipe flow (DN200 mm) – TOPFLOW conditions.	Euler-Euler polydispersed approach using NPHASE-CMFD. SST κ – ε with automatic wall functions. 2D Axisymmetric mesh with 40 x 500 cells.

		Two gas-fields with three bubble groups. Drag, lift, turbulent dispersion, wall lubrication, bubble induced turbulence, and virtual mass. Bubble breakup and coalescence. Study on changes in the air-density
Wang et al. (2010)	Gas-liquid bubbly and churn-turbulent flow. Air-Water. Vertical bubble column and pipe flow.	Two-group IATE model implemented in FLUENT. $\kappa - \varepsilon$ with standard wall functions. Three-dimensional. One (for bubbly flows) and two gas-fields (for churn-turbulent flows). Drag, lift, turbulent dispersion, wall lubrication, 'transient forces' (Basset and virtual mass forces) Enthalpy equation stablished within the one and two group IATE.
Montoya et al. (2013) Montoya et al. (2014a)	Adiabatic gas-liquid churn-turbulent and slug flow. Air-Water. Vertical pipe flow (DN200 mm) – TOPFLOW conditions.	Euler-Euler polydispersed approach with iMUSIG BPBE from CFX. SST $\kappa - \omega$ with automatic wall functions. 2D Axisymmetric mesh with 40 x 800 cells. Two and three gas-fields with drag, lift, turbulent dispersion, wall lubrication, and bubble induced turbulence closure laws. Bubble breakup and coalescence (Liao, 2012).

2.3 Limitations on the state-of-the-art and suggestions for improvements

As explained in a previous section, one of the main challenges related to the formulation of the closure laws for churn-like bubbles is the fact that the present models have been developed for single bubbles and validated for bubbly flows. A better formulation for the lift force, for example, of these deformable bubbles is particularly challenging, since these bubbles are not stable enough for producing single-rising bubble experimental data. At the same time DNS methods maturity and their computational requirements makes them inapplicable to churn-turbulent flow. As with the lift, other closure forces suffer from the same large number of simplifications and assumptions. An example of these is the fact that as the bubble grows to an equivalent spherical bubble diameter greater than the diameter of the pipe, the effect of the pipe walls on the drag for the gas is not taken into account. These problems could be improved by defining different fluid morphologies for churn-turbulent flows.

When having different fluid morphologies, different interfacial area density formulations could be needed in order to smoothly translate from one set of models to the next. The interfacial area density approach proposed first by Egorov (2004), allows the detection of the morphological form and the corresponding switching of each correlation from one object pair to another. It also provides a law for the interfacial area density and the drag coefficient for a full range of volume fractions between zero and one.

The AIAD concept improved over the previously mentioned approach by refining the physical modeling in the asymptotic limits of bubbly and droplets flows (Höhne et al., 2010). This model is in principle applicable to stratified flows allowing the calculations of droplets and bubbles entrained within each phase, and it was validated by Höhne for horizontal stratified flows and by Deendarlianto et al. (2011) for a model of hot-leg PWR.

Using the basic concept of the AIAD mode, alongside with the inhomogeneous multiple size group, a GEneralized TwO Phase flow concept was first published by Hänsch et al. (2012). The GENTOP approach is based on the use of at least a 3-field-simulation. The flow is represented by a liquid phase, a polydispersed gas phase, and a continuous gas phase. This concept could allow, for example, to fully resolve large churn-like bubbles while maintaining a realistic demand for computational resources.

2.4 Chapter summary

The churn-turbulent flow represents one of the most challenging regimes in the multiphase flow area. Much has been done for the understanding of this flow pattern, but still, the state of the art on theoretical modeling framework of these high-turbulent regimes is very basic.

The understanding of the transition between the different patterns in vertical gas-liquid pipe flows is essential in order to reflect the main behavior of the two-phase flows in the simulations. The transitions from and to churn-regime depend highly on the pipe diameter since the stability of the bubbles along with the behavior of the different bubble breakup and coalescence mechanisms produce different effects from one flow to the other when increasing gas velocities. A reliable model of the churn-turbulent flow must not depend on the specific transition that could occur, but instead, should be able to reproduce these changes by itself depending on the established channel and boundary conditions.

The limitations of zero and one-dimensional approaches have shown that only CFD models could possibly correctly predict highly-turbulent, space and time dependent flows. On the 3D modeling frameworks, it has been shown that possibly the most reliable model in terms of accuracy and computational resources economy is the Euler-Euler modeling approach. This model alone could not predict accurately most of the expected highly-turbulent flow regimes. For this reason, many studies have been proposing 'extensions' that could bring an improvement of the representation on the reality behind these flow regimes. It has been seen that one of the most promising and useful improvements found in the literature is the iMUSIG approach. This allows to accurately relate different physical behaviors to different gas structures that otherwise would have been incorrectly-modelled by the wrong assumption of equal behavior. Another interesting concept is that of the AIAD model, which in combination with the GENTOP concept has been shown to be useful to model the interfacial transfer between phases. This concept could fully resolve large deformable gas-structures as those encountered in churn-turbulent flow.

On the matter of turbulence treatment in the churn-turbulent regime, and in multiphase flow in general, there are many theories but not successfully validated approaches that could predict flow intermittencies as the ones produced by the bubbles encountered on the slug or churn-regime. It is clear that the RANS treatment concept is far away from an accurate prediction on these regimes for reasons that have been stated in this literature review, and through many other research papers. Still, until an improvement is developed, then these approaches at least produce a simple, non-highly resource consuming method to predict some of the turbulence scales presented on the flow. There is no doubt about the extreme importance that future developments of new and more advanced multiphase turbulence-treatment techniques have, such as an hybrid LES method with both filtered and statistical interface concepts, as mentioned by Bestion (2011).

On the closure laws needed for these Euler-Euler approaches, there is a necessity for important further development in the highly-turbulent flow area. There is a series of models and concepts in existence that could predict the expected forces in the studied flow. Still, the fact that these forces have been developed and validated for the physics predicting bubbly regimes, make them in most cases, almost useless for churn or slug-like bubbles.

3 Description of the experimental databases

Most simulations presented in this thesis have been validated using an experimental database for air-water two-phase flows in vertical stainless steel pipes with diameters of 51.2 mm and 195.3 mm, that has been extracted from the thermal-hydraulic test facilities TOPFLOW and MT-Loop at the Helmholtz-Zentrum Dresden-Rossendorf. Choosing both facilities allows considering both, churn-turbulent and slug flow regimes, as well as fastest parametric studies.

3.1 The Measurement Test Loop (MT-Loop) facility

The MT-Loop facility represents a loop in which the liquid phase is supported by a circulating pump in a ring (see Fig. 3.1). The two-phase current is made either by mixing air in, or by vaporization in a tube line section heated electrically.

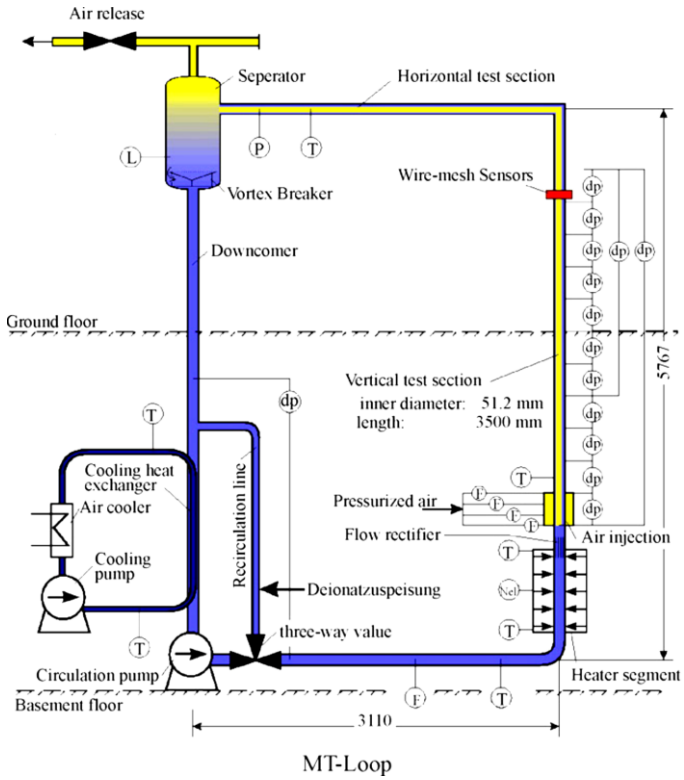

Fig. 3.1 General scheme of the thermal hydraulic vertical test facility MT-Loop (Lucas et al., 2005).

The inner diameter of the pipe is 51.2 mm, and the maximum capacity of the circulation pump is approximately 30 m^3/h. The facility can be operated with steam-water at pressures up to 2.5 MPa, and a maximum temperature of 225 ºC. The maximum length of the vertical test section is about 4 m, but since the air injection is located above a heater section, the maximum inlet length during the tests is limited to about 3.5 m. The injection of the gas was made using 19 equally distributed capillaries, and depending on the superficial gas and liquid velocities chosen for a specific case, different

combinations of the injection needles were used. Stationary flow rates were commonly used, and gas and liquid superficial velocities were varied in a wide range of about 100 different combinations. This included a large range of flow regimes such as stable bubbly flow, finely dispersed bubbly flow, and slug flow, including the observed transition between these flow patterns within the pipe.

The measurement planes consists of a two-level wire-mesh sensor (Fig. 3.2). The lower sensor is used for obtaining data on the gas volume fraction profiles and bubble size distributions, while the second one is to determine gas velocities by cross-correlation of both sensors. The smallest bubble size that can be measured by the wiremesh sensor is about 2 mm. The results of these experiments are, for example, the time averaged radial profiles of the gas fraction, the gas velocity, the time and cross-section averaged bubble size distributions, and the gas fraction data regarding the resolved bubble size and spatial distribution. The distance between the sensor and the air injection varied from 0.03 m to 3.03 m (inlet lengths 0.6 to 59.2 L/D).

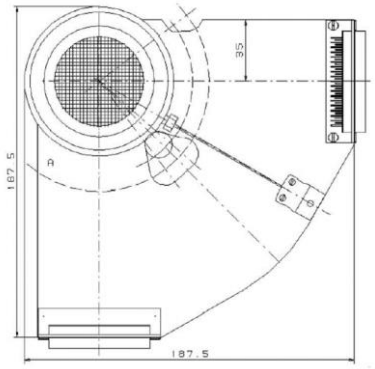

Fig. 3.2 Wire-mesh sensor scheme for the thermal hydraulic vertical test facility MT-Loop (Lucas et al., 2005).

3.2 The TwO Phase FLOW (TOPFLOW) facility

The TOPFLOW facility provides a high-quality database for air/water and steam/water two-phase flows in vertical pipes with nominal diameters of 50 mm and 200 mm (Fig. 3.3). The superficial gas velocities (J_G) vary from 0.0025 to 18.97 m/s, and the liquid superficial velocities (J_L) vary from 0.0405 to 4.047 m/s.

The pressure at the gas injection is kept constant at 0.25 MPa. The advantage of such boundary condition lies in that the measured data represents the evolution along the pipe as if the gas injection was in a fixed position and the measurement plane varies. The temperature in the system was also kept constant at 30°C for adiabatic conditions.

The test section DN200 is the one used for validations in this thesis. This section is equipped with six gas inlet locations which allowed the injection of air or steam via orifices in the pipe wall. Having such injection via wall orifices allows the two-phase flow to rise smoothly to the measurement plane without having any influence from the feeder within the tube at any other location along the flow. The liquid phase was supplied from the bottom of the test section.

The number of parameters resulting from the TOPFLOW experiments are the same as those from its predecessor (MT-Loop), and are based on the bubble size distribution, velocity profiles, and radial void fraction profiles, which are obtained also with a similar technique as those from the MT-Loop data (Prasser et al., 2007). The distance between the sensor and the air injection varied from 0.221 m to 7.802 m (inlet lengths 1.1 to 39.9 L/D).

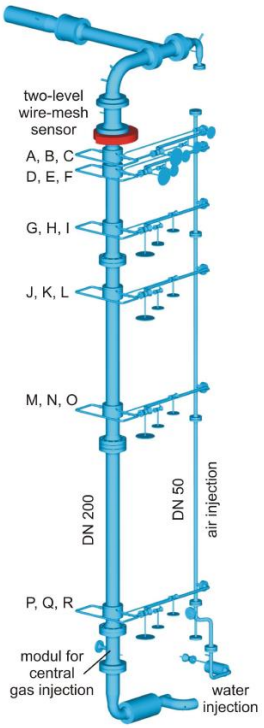

Fig. 3.3 Vertical test section of the TOPFLOW facility with a variable gas injection system (Lucas et al., 2010).

3.3 Chapter summary

Most simulations present in this dissertation have been validated using the previously described experimental database for air-water two-phase flows in vertical stainless steel pipes with diameters of 51.2 mm, and 195.3 mm obtained at the thermal-hydraulic test facilities TOPFLOW and MT-Loop in HZDR. These databases provide information about the evolution of the two-phase flow along the pipe height. Several measurements with varying distances between the gas injection and the measurement plane were made for different combinations of gas and water flow rates. Both facilities have been briefly described here. While the MT-Loop experiments were discontinued, they represent a large amount of data which can be extremely useful for validation of fast CFD calculation models and parametric studies, as well as for nuclear related systems because of its relatively small dimensions and its large databank of steam-water and air-water experiments. More information about these experimental facilities can be found in Lucas et al. (2005), Krepper et al. (2005), Prasser et al. (2007), and Frank et al. (2008).

4 Study of the current limitations on theoretical modeling for high void fraction regimes

In this chapter a series of mechanistic models, which have been developed and validated for bubbly flows, are described and further applied for higher void fraction regimes. The effects and limitations of modeling via these approaches for bubbly-to-churn transitional flow as well as for churn-turbulent flow regime, are study in-depth.

4.1 HZDR baseline models for bubbly flows

The Computational Fluid Dynamics Department of the Helmholtz-Zentrum Dresden-Rossendorf (HZDR) has tested and successfully validated a baseline formulation for polydispersed closure laws for Euler-Euler calculations in multiphase bubbly flows (Ziegenhein et al., 2015; Rzehak et al., 2014; Liao et al., 2015). Based on Eq. 2.17, this baseline model will be presented in the current section, and represents the starting point for the research of this doctoral dissertation.

The drag force model was given in Eq. 2.18, and for the drag coefficient ($C_{D,k}$) calculation, the expression proposed by Ishii and Zuber (1979) has been selected. The next correlations (Eq. 4.1, Eq. 4.2, and Eq. 4.3) represents the drag coefficient for cap, elliptical, and distorted bubbles respectively. The drag coefficient for spherical particles used in this correlation, is given by Schiller and Naumann (1935) as shown in Eq. 4.4, and the final regime selection is given by Eq. 4.5.

$$C_{D,k(cap)} = \frac{8}{3} \tag{4.1}$$

$$C_{D,k\,(ellipse)} = \frac{2}{3} Eo^{\frac{1}{2}} \tag{4.2}$$

$$C_{D,k\,(distorted)} = \min(C_{D,k\,(ellipse)}, C_{D,k\,(cap)}) \tag{4.3}$$

$$C_{D,k\,(sphere)} = max\left(\frac{24}{Re}(1 + 0.15\, Re^{0.687}), 0.44\right) \tag{4.4}$$

$$C_{D,k} = \max(C_{D,k\,(sphere)}, C_{D,k\,(dist)}) \tag{4.5}$$

The correlations presented before are only valid for sparsely distributed particles. Once the gas velocity increases, there is a large probability of swarms of bubble moving together effectively reducing the overall drag. This effect is accounted within the drag coefficient, by the addition of a reduction factor multiplier, as in Eq. 4.6 to Eq. 4.8.

$$C_{D,k(cap)} = \left(\frac{8}{3}\right)\left(1-\alpha_{d,k}\right)^2 \tag{4.6}$$

$$C_{D,k\,(ellipse)} = \left(\frac{2}{3}Eo^{\frac{1}{2}}\right)\left(\frac{1+17.67\left(\frac{\mu_c}{\mu_m}\left(1-\alpha_{d,k}\right)^{\frac{1}{2}}\right)^{\frac{6}{7}}}{18.67\left(\frac{\mu_c}{\mu_m}\left(1-\alpha_{d,k}\right)^{\frac{1}{2}}\right)}\right) \tag{4.7}$$

$$C_{D,k\,(sphere)} = \frac{24}{Re_m}\left(1+0.15\,{Re_m}^{0.687}\right) \tag{4.8}$$

Where,

$$Re_m = \frac{\rho_c|\boldsymbol{V}_d-\boldsymbol{V}_c|D_p}{\mu_m} \tag{4.9}$$

$$\frac{\mu_m}{\mu_c} = \left(1-\alpha_{d,k}\right)^{-2.5\frac{\mu_d+0.4\mu_d}{\mu_c+\mu_d}} \tag{4.10}$$

The regime selection for the drag coefficient with swarm factor correction is given by Eq. 4.11.

$$C_{D,k}\begin{cases} C_{D,k\,(sphere)} & if \quad C_{D,k\,(sphere)} \geq C_{D,k\,(ellipse)} \\ \min\left(C_{D,k\,(ellipse)}, C_{D,k(cap)}\right) & if \quad C_{D,k\,(sphere)} < C_{D,k\,(ellipse)} \end{cases} \tag{4.11}$$

The interfacial lift force was represented by Eq. 2.20, and the lift coefficient ($C_{L,k}$) is calculated as proposed by Tomiyama et al. (2002).

$$C_{L,k}\begin{cases} \min\left(0.288\tanh(0.121Re_k), f(Eo_k)\right) & if \quad Eo_k < 4 \\ f(Eo_k) & if \quad 4 \leq Eo_k \leq 10 \\ -0.27 & if \quad Eo_k > 10 \end{cases} \tag{4.12}$$

Where $f(Eo_k)$ is defined as shown in Eq. 4.13.

$$f(Eo_k) = 0.00105{Eo_k}^3 - 0.0159{Eo_k}^2 - 0.0204Eo_k + 0.474 \tag{4.13}$$

The modified Eötvös number or Eo_k is calculated as in Eq. 4.14.

$$Eo_k = \frac{g(\rho_c-\rho_d){D_{h,k}}^2}{\sigma} \tag{4.14}$$

From an empirical correlation by Wellek et al. (1966) for the aspect ratio of an elliptical shape bubble, the maximum horizontal dimension of the particle, $D_{h,k}$, can be calculated as in Eq. 4.15.

$$D_{h,k} = D_b \sqrt[3]{1 + 0.163 {Eo_k}^{0.757}} \tag{4.15}$$

The critical bubble diameter at which the lift force changes sign can be found by solving the roots of Eq. 4.13. It gives a value of 5.8 mm under atmospheric pressure and room temperature for air bubbles in water.

The model used for the turbulent dispersion force is known as Favre average drag (FAD) proposed by Burns et al. (2004), and it was shown in Eq. 2.19. In that correlation, $C_{D,k}$ represents the interface drag force coefficient. Therefore, this model depends on the drag force correlation that is being used. The term σ_{tc} refers to the turbulent Schmidt number for the continuous phase volume fraction, which is commonly taken to be 0.9 (CFX-Theory User Manual, ANSYS V14.0). The coefficient for turbulent dispersion (C_{TD}) is taken as 1.0.

For the wall lubrication force the model by Tomiyama (1998) is used as it was presented in Eq. 2.22. The wall coefficient (C_W) used there, was the one proposed by Hosokawa et al. (2002), as shown in Eq. 4.16.

$$C_W = \max\left\{\frac{7}{{Re_k}^{1.9}}, 0.0217Eo\right\} \tag{4.16}$$

While the virtual or added mass force has not been used in this thesis for reasons stated in Section 2.2.4, this is still part of the HZDR bubbly flow baseline model and it is represented by Eq. 2.21. The virtual mass coefficient ($C_{VM,k}$) is given to be equal to 0.5 (Krepper et al., 2005).

All calculations within the HZDR baseline framework, take into consideration two velocity groups by means of the inhomogeneous multiple size group approach. This is done in order to consider the separation of small and large bubbles due to the Tomiyama lift coefficient sign change given by Eq. 4.12. Furthermore, these subdivisions using the iMUSIG model, allows to consider better bubble breakup and coalescence. The Liao et al. (2011) model was proposed to be part of the HZDR baseline approach. Since this model is still in a testing and developing phase, in the calculations presented in this chapter the Luo-Svendsen / Prince-Blanch as well as the Liao model were used, obtaining rather indistinctive results.

In terms of turbulence treatment, the dispersed zero equation is used for the dispersed gaseous phases, while the SST *k*-ω approach is used for the continuous phase. One of the advantages of the *k*-ω model over the *k*-ε is the treatment when in low Reynolds numbers for a position close to the wall. This model does not need the complex non-linear damping functions required for the *k*-ε, and for that

matter can be considered as more accurate and robust. While the *k*-ε model need a near-wall resolution of at least $y^+ = 0.2$ in low Reynolds number, the *k*-ω model would require at least $y^+ = 2$. While this is still too rough for most industrial applications, commercial codes may use a near wall treatment model that allows for a smooth shift from a low-Reynolds number to a wall function formulation. The *k*-ω based SST model accounts for the transport of the turbulent shear stress and produces accurate predictions of the onset and the amount of flow separation under adverse pressure gradients. Inside the RANS turbulence treatments, it is expected that the SST model along with the automatic wall function produces acceptable results on the treatment of turbulent scales for bubbly flows.

Finally, in order to account for the effect of the bubbles on the turbulence of the continuous phase, additional source terms proposed by Rzehak and Krepper (2012) are added to the two equation turbulence model. The source terms describe the bubble effects for the *k* and ε-equations and are formulated on the assumption that all energy lost by the bubble due to drag is converted to turbulent kinetic energy.

4.2 Computational grid and boundary conditions

Three experimental flow cases from TOPFLOW, summarized in Table 4.1, were adopted for validation of the presented approach and are discussed in this chapter. Cases 127 and 129 are both under churn-turbulent flow regime conditions, while case 118 is considered to be a transition from bubbly to churn-turbulent flow.

Table 4.1 Test cases superficial velocities description.

Run number	Superficial liquid velocity (m/s)	Superficial gas velocity (m/s)
118	1.017	0.219
127	0.405	0.342
129	1.017	0.342

The data which corresponds to the inlet boundary conditions for the liquid continuous phase (turbulent kinetic energy, and turbulent eddy dissipation) was taken from fully developed single phase calculations made on the same computational grid as the multiphase simulations. The liquid velocity profile is calculated from the TOPFLOW experiments as a correlation which takes into account the possible displacement of the liquid velocity as a function of the gas data.

The importance of these parameters comes as consequence of applying the boundary conditions of the gas phase from L/D = 1.1, including gas velocity, mass flow rate, and size fractions, in order

to avoid the modeling of the inlet of the facility. Modeling of this part would need a very fine nodalization to be appropriately represented (72 x 1 mm orifices). Furthermore, the current models would almost certainly be unable to represent the intense turbulence and bubble breakup and coalescence which occur at the first millimeters after injection.

Following the HZDR bubbly flow baseline framework, the TOPFLOW data has been arranged into two velocity groups. The first velocity group contains six bubble size fractions up to 5.8 mm, while the second group is organized into twelve to fourteen bubble size fractions larger than the limit size of the first velocity group. The defined number of size fraction is dependent of the specific test case. A logarithmic distribution has been used for the calculation of the different size groups.

The computational setup in this chapters replicates the experimental conditions established in the TOPFLOW air-water experiments. An axisymmetric 40 x 800 grid with refined cell size of 1.5 mm near the wall, and 0.5 mm near the inlet, was used to represent the 0.09765 m x 8 m system. Taking advantage of the axisymmetric, only a 4 degrees segment of the pipe was modeled, establishing a so-called 2D axisymmetric approximation with its respective symmetry planes (Fig. 4.1). This mesh was developed using the ICEM CFD meshing tool.

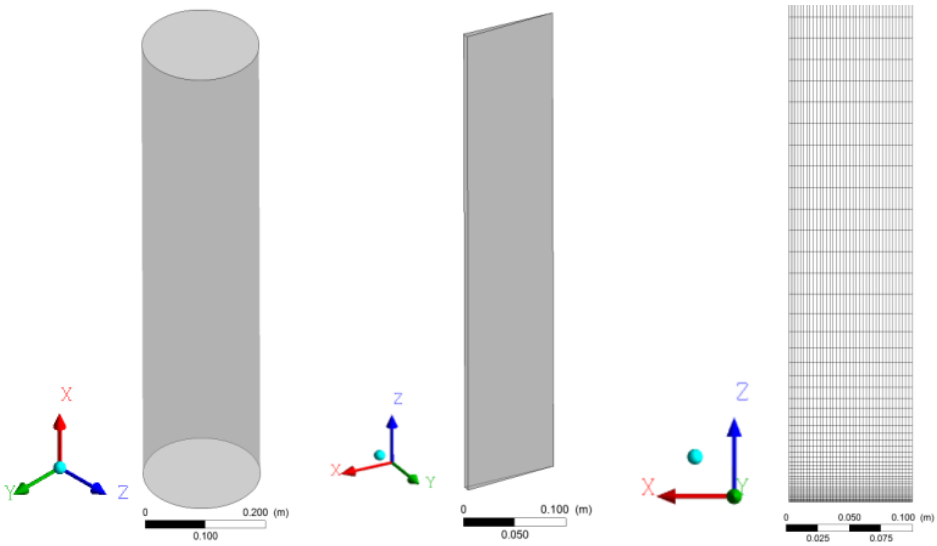

Fig. 4.1 3D pipe geometry, 2D axisymmetric approximation, and 2D axisymmetric mesh with unequal node distribution (segmented in the axial direction).

At the wall boundary, a no slip condition was enforced for the continuous phase and a free slip condition for the gas. A symmetry boundary condition was established along the pipe centerline. The mesh unequal distribution, with a finer spacing at the inlet and at the wall of the pipe was established with the intention of capturing the developing flow at the inlet as well as the effect of higher gradients of velocity and bubble concentration near the wall of the tube. All calculations were tested against two other different grids, which were refined by a factor of 2 each, in order to prove grid independency.

- **Validation and mesh statistics for the single phase boundary condition calculations**

A series of single phase calculations was performed in order confirm mesh independency and to validate the simulation approach against experimental data reported by Shawkat et al. (2008). The superficial velocity value chosen for this comparison was 0.45 m/s for its similarity to the superficial liquid velocity from case 127 from the TOPFLOW experiments. Tests with 0.2 m/s and 0.68 m/s were also performed, showing no particular deviation, and have been omitted in this section.

In Fig. 4.2, a comparison between the experimental values and three different mesh sizes is given for both the turbulent kinetic energy (represented by its square root) and velocity profiles. Each next mesh represents double nodalization in both radial and axial directions, being Mesh 2 the original grid previously described.

In terms of the turbulent kinetic energy, the results of the calculations converged to similar values as the ones from the experiments and slightly diverge when getting closer to the wall. In terms of the mesh statistics, all the results converged to similar values, showing mesh independency from the coarser mesh. In terms of the velocity profile, it can be observed that all three results from the different meshes converge to similar values as the one from the experiments. As the mesh is refined and nodes are added closer to the wall, the velocity values keep decreasing in the near-wall-cells, due to the non-slip boundary condition. A similar trend was observed in Fig. 4.2a, but was not shown due to comparison purposes, since the experimental measurements did not reach such radial values.

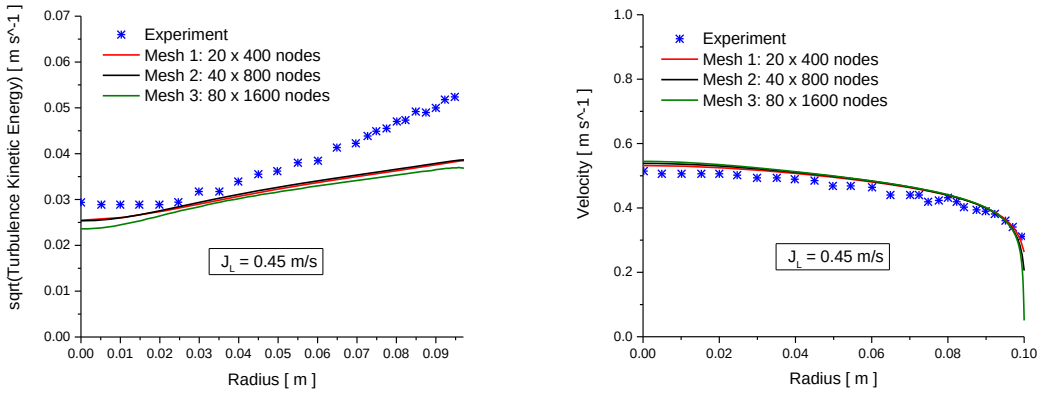

Fig. 4.2 Validation and mesh statistics for A) square root of turbulence kinetic energy radial profile and B) velocity radial profile for fully developed flow at J_L = 0.45 m/s.

4.3 Results and discussion on 2-iMUSIG group parametric studies

Extensive testing was performed on the proposed modeling approach using the experimental conditions from TOPFLOW. The objective of the work was to validate a number of models previously proposed for bubbly flows, and now implemented on churn-turbulent regime.

The radial concentrations of the different defined gas fields, as well as the gas and liquid velocity magnitude profiles can be seen in Fig. 4.3 and Fig. 4.4 for the complete channel. In order to plot the whole channel, an unequal ratio of height to length has been used in the presented images. The left side in each of the domains represents the wall boundary. For both cases, it can be seen that the gas field represented by the small bubbles or "Gas 1", remains near the wall along the channel, while the gas field represented by the largest gas structures or "Gas 2" is distributed in a way in which the maximum value of volumetric concentration is higher at the center of the pipe. It can also be observed in the images how the highest velocity values appear at the center of the pipe. Case 118 presents a very similar quantitative profile as 129, and so only the contour representation of the last one is shown here. Lowering the superficial liquid velocity in experiment 127, on the other hand, shows a much wider distribution for the second gas field across the whole domain.

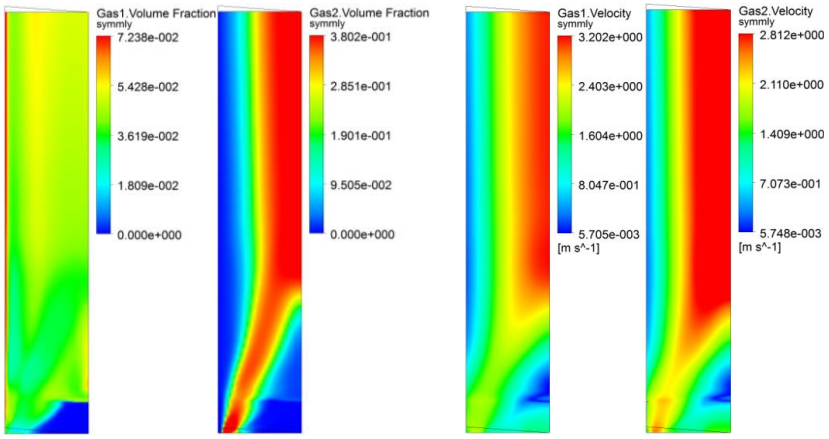

Fig. 4.3 Contour representations for the distribution of A) void fraction and B) velocity for each dispersed field in experiment 129.

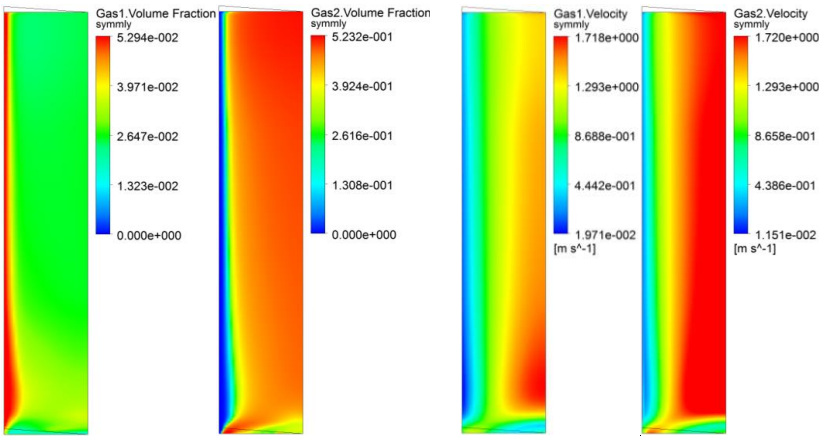

Fig. 4.4 Contour representations for the distribution of A) void fraction and B) velocity for each dispersed field in experiment 127.

A quantitative comparison of the experiments in terms of the total radial void fraction, shows an acceptable general agreement between case 127 and the corresponding simulation (see Fig. 4.5a), especially when compared against experiment 129 and 118 (higher liquid superficial velocity). Once the liquid superficial velocity increases in experiment 129 (see Fig. 4.5b), a good fit with the

calculation can be found for the lower levels (L/D = 1.7), but a peak appears between the wall and the center of the pipe for the next higher measurement plane (L/D = 7.9). For posterior higher measurement positions (L/D = 39.9) this deviation diminishes obtaining a similar trend as in experiment 127. While maintaining the same liquid superficial velocity and decreasing the gas velocity in experiment 118, an analogous behavior of the total radial void fraction as with case 129 was encountered.

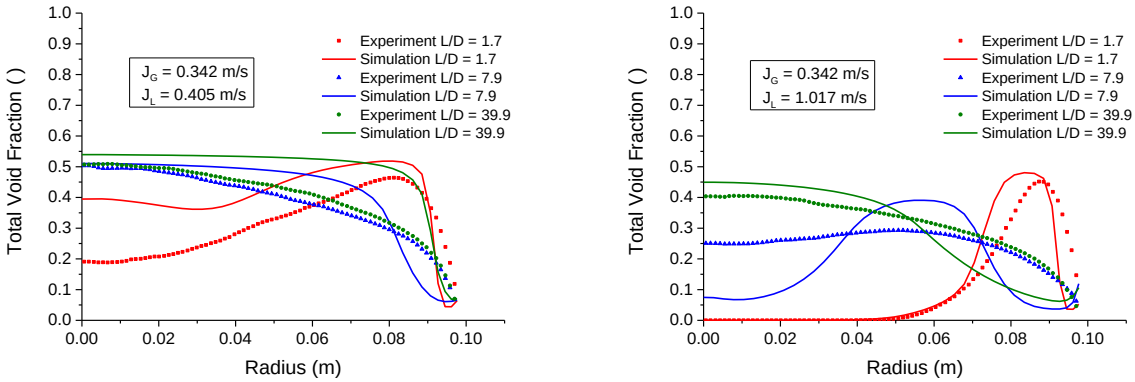

Fig. 4.5 Validation of the radial total void fraction against A) experiment 127 and B) experiment 129.

In principle, it appears as if this deviation at L/D = 7.9 for cases 118 and 129, could be caused by a too large lift force in comparison with the turbulent dispersion force. Furthermore, parametric sensitivity studies made by Tselishcheva et al. (2010) have shown that both a negative lift coefficient and a too low drag force coefficient (which would lower the turbulent dispersion force as it can be inferred from Eq. 2.19) could produce similar behaviors in the total void fraction as the one observed for the highest level of the studied system.

A study of the averaged gas velocities for the three experimental cases was also prepared. The observed behavior of the trend in the gas velocities for the three cases is analogous to the overall radial void fraction in terms of the expected deviations (Fig. 4.6).

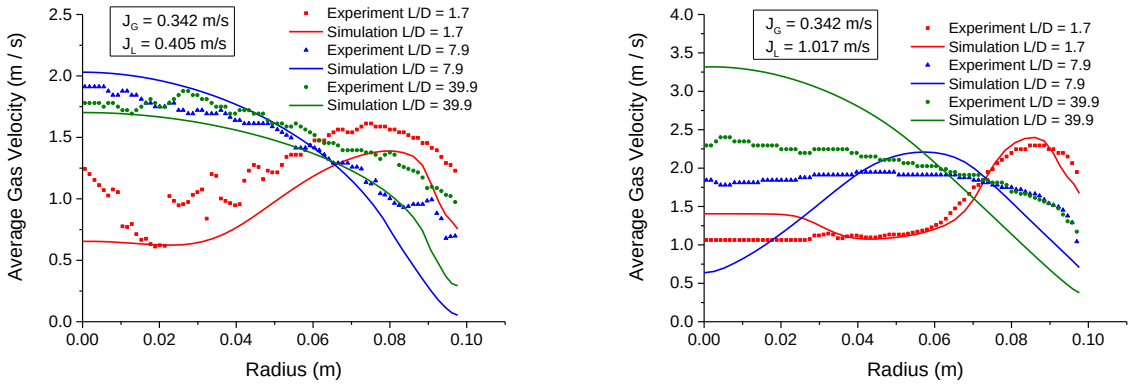

Fig. 4.6 Validation of gas averaged velocities against A) experiment 127 and B) experiment 129.

For experiment 127, the velocities for the whole evolution of the flow through the pipe qualitatively fit the experimental data very well (see Fig. 4.6a). For both, experiment 118 and 129 (see Fig. 4.6b), the simulation fits almost perfectly the experiments for the height which is closer to the inlet boundary as expected, but the agreement diminished for bubble sizes larger than 40 mm. For the measurement level L/D = 7.9, the velocity presents a similar peak as the one seen in Fig. 4.5b, which attenuates eventually before achieving higher positions (L/D = 39.9).

In terms of bubble size distribution for case 129 (see Fig. 4.7), generally an overall acceptable prediction of the experimental trend with a constant under prediction of bubbles with smaller sizes is shown. This is then followed by an overprediction of bubbles ranging from about 10 to 35 mm. This last deviation is more visible closer to the inlet boundary (L/D = 1.7), and gradually decreases until the highest measurement level (L/D = 39.9). Bubbles whose sizes are larger than 40 mm are constantly under predicted for all measurement heights. The behavior observed for the values smaller than 35 mm can be explained in part due to too high coalescence at the beginning of the pipe, which in turn creates an under prediction of the smaller bubbles. This could be improved, for example, by diminishing the coefficient for wake entrainment in the Liao coalescence model. When the superficial gas velocity is increased in experiment 118, the behavior of the bubble size distribution remains similar as in 129. The only difference is that the under prediction observed for the smaller bubble size distribution peak increases, compared to the observations of experiment 129.

Once the superficial liquid velocity decreased in experiment 127 compared to 129 (see Fig. 4.8), there is the appearance of even larger bubbles in the experimental data. In turn, an overprediction of smaller bubble sizes close to both the inlet boundary (L/D = 1.7) and the outlet (L/D = 39.9) is observable on this case, in contrast to the typical under prediction found in the prior two simulations. This last deviation results from the effect of reducing the liquid superficial velocity to less than half, which in turn also increase the turbulence parameters, and for that matter increase the breakup over the whole domain.

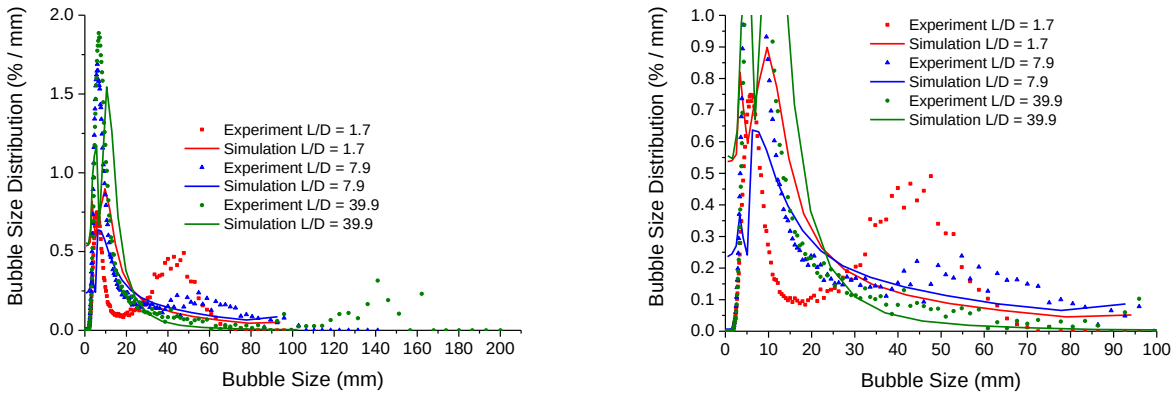

Fig. 4.7 Experiment 129 A) validation and B) zoom-in observation to the simulated results for bubble size distribution.

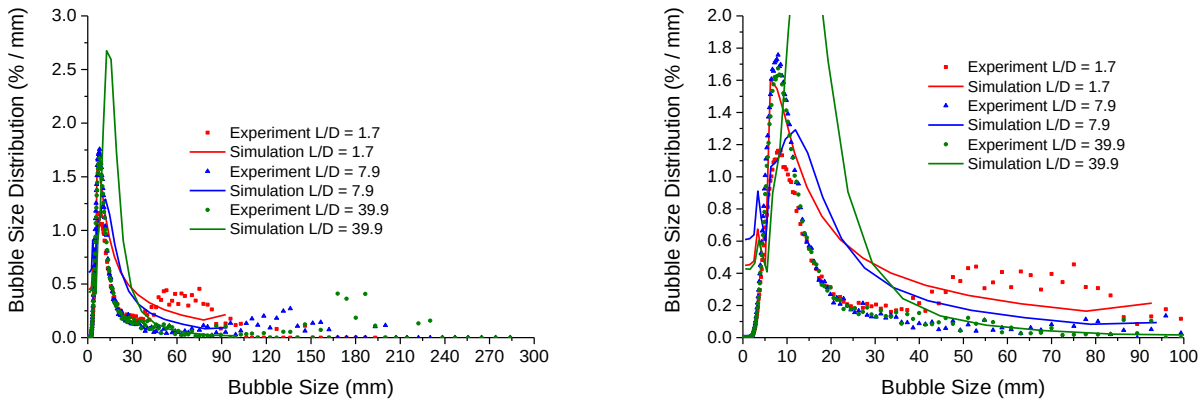

Fig. 4.8 Experiment 127 A) validation and B) zoom-in observation to the simulated results for bubble size distribution.

It is already possible to observe that many of the deviations appear to have their base in the misconception that the largest bubbles behave in the same way as it is expected from bubbly flow conditions. In this respect, an approach will be shown in the next chapter in which a third dispersed velocity field is used for further subdivision of the overall gas phase.

For mesh statistics purposes, the void fraction and velocity profiles are plotted in Fig. 4.9 and Fig. 4.10, respectively. The results based on the three prior described meshes has been given at L/D = 7.9 and L/D = 39.9 for case 129. In terms of radial void fraction profiles, it can be observed that for the lower measurement plane the coarser mesh strongly diverged from the refined ones. For the highest measurement plane all three results converged to the same value. The same trend can be seen for the averaged gas velocities, where the coarser mesh differs from the refined ones only at L/D = 7.9. As it was stated in the previous section, the mesh used during all shown analysis was mesh number 2.

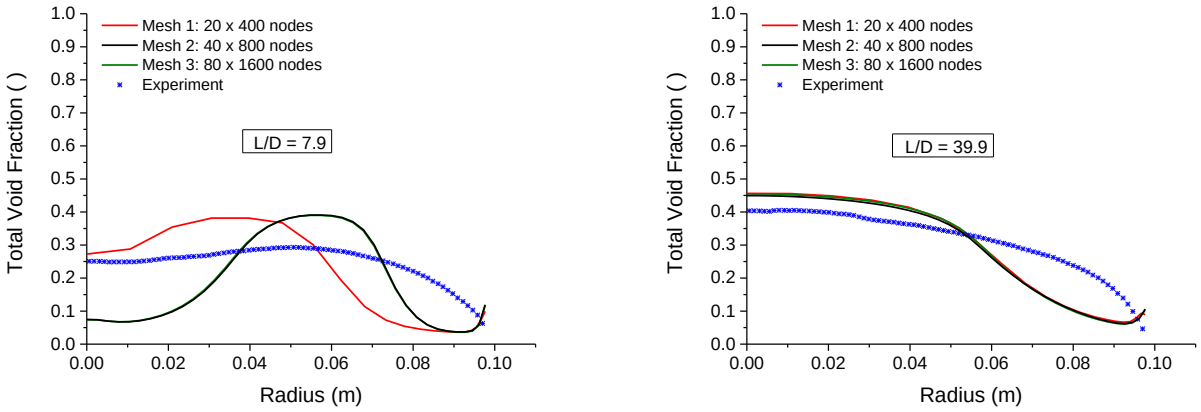

Fig. 4.9 Mesh statistics for radial void fraction profiles at A) L/D = 7.9 and B) L/D = 39.9.

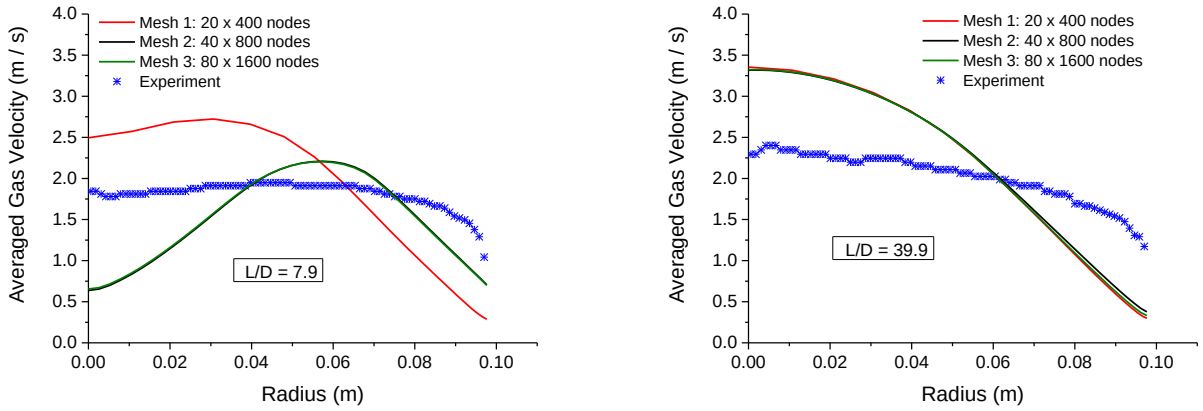

Fig. 4.10 Mesh statistics for averaged gas velocity radial profiles at A) L/D = 7.9 and B) L/D = 39.9.

4.4 Chapter summary

A series of closure relations known as the HZDR baseline model have been implemented and tested against a series of multiphase flow calculations under transitional bubbly-to-churn and churn-turbulent flow in a large diameter pipe. The calculations have been compared to experimental data from the TOPFLOW facility for bubble size distribution, radial void fraction and velocity profiles.

It was shown that while results using a bimodal gas distribution and bubbly flow closure laws produce promising and relatively adequate results for the highest measurement planes, they cannot yet predict the expected physical behavior for this flow regime. The discrepancy is more evident when lower measurement levels are studied, showing a very slow migration of the second gas-field towards the center of the pipe. This produced an unphysical peak in the quantitative results when compared against experimental data.

It evident that the results suffer from the assumption that the same physical representation developed for small bubbles could be extended to represent churn-like and slug bubbles. A more promising approach could be represented by modeling these high void fraction regimes based on at least a three gas field approach or trimodal distribution based on small spherical bubbles, larger spherical bubbles, and large distorted bubbles. This would allow a proper, or at least improved, separation of the physics behind the churn-like deformable gas structures.

5 Establishment of a baseline model at high void fraction regimes for simulations using the Eulerian-Eulerian approach

This chapter describes the methodology behind the extension of the HZDR baseline model to include higher void fraction regimes such as churn-turbulent and slug flow. This is done through implementing, studying, and applying different closure relations by adding a third gas-field as a new velocity group via the iMUSIG approach. Achievements and limitations of the proposed set of closure models will be discussed by further comparisons to the MT-Loop and TOPFLOW data.

5.1 Calculations using a third gas-field for churn-like bubbles and the HZDR closure laws for bubbly flows

A first set of calculations was initially performed following the findings of the previous chapter, and implementing an extra gas-field for the separation of very large deformable bubbles. In this case, a third velocity group is defined based on the maximum distorted bubble limit diameter correlation (Eq. 2.25) proposed by Ishii and Zuber (1979). This diameter was calculated to be 10.8 mm for the current simulated conditions. This reduced the second gas field to a mere three gas size fractions and left the third gas-field with eleven size fractions.

In terms of radial concentrations of the different gas fields and its velocity magnitudes, experiment 129 has been chosen in order to study the general qualitative and quantitative effect (Fig. 5.1). Here, "Gas1" represent the smallest bubbles ($d_b \leq 5.8$ mm), which maintain its higher concentration mostly closer to the wall as expected. The real difference occurs between "Gas2" (5.8 mm $< d_b <$ 10.8 mm) and "Gas3" ($d_b \geq 10.8$ mm), where it can be observed that the third gas field contains most of the void contribution to the system. This shows that most of the behavior within these high void fraction cases depends on this new gas field. As expected, "Gas2" dispersed in a wider manner across the radius of the pipe, while "Gas3" is mostly concentrated at the center.

In terms of radial total void fraction, it can be observed that the peak encountered at L/D = 7.9 in Fig. 4.5b, is no longer visible for the three-field simulation (see Fig. 5.2a). This comes at the cost of accuracy for the radial total void fraction at the lower measurement levels (L/D = 1.7). The addition of a third gas phase in terms of averaged gas velocity follows a similar trend as in the void case, and so the unphysical peak is no longer observable (Fig. 5.2b). A constant overprediction of gas velocities for the values at the center of the pipe, and a constant under prediction close to the wall can be seen in this case. As observed in Fig. 5.1, the higher contribution of the total radial void fraction for the whole length comes from the third gas field. In order to properly study this effect, it is a much better

approach to separate the different contributions of the total radial void fractions allowing a deeper analysis of the influence of the third gas field. It can be observed from Fig. 5.3a, that from early stages in the pipe (L/D = 7.4), there is an unphysical push of the void fraction representing the largest bubbles ("Gas3"), towards the center of the pipe. This same behavior maintains itself until the last measurement plane at L/D = 39.9 (Fig. 5.3b).

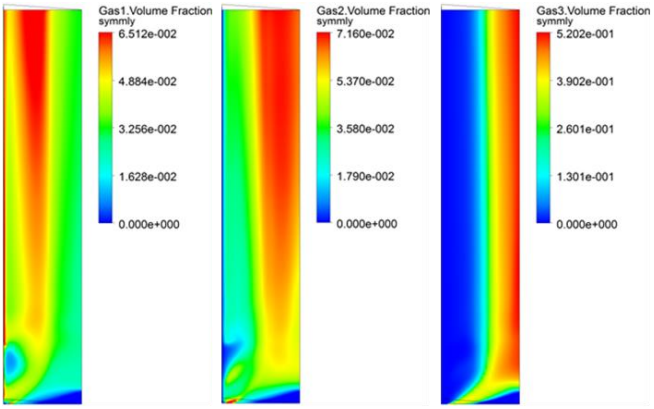

Fig. 5.1 Contour representation of void fraction distribution for each dispersed field in experiment 129.

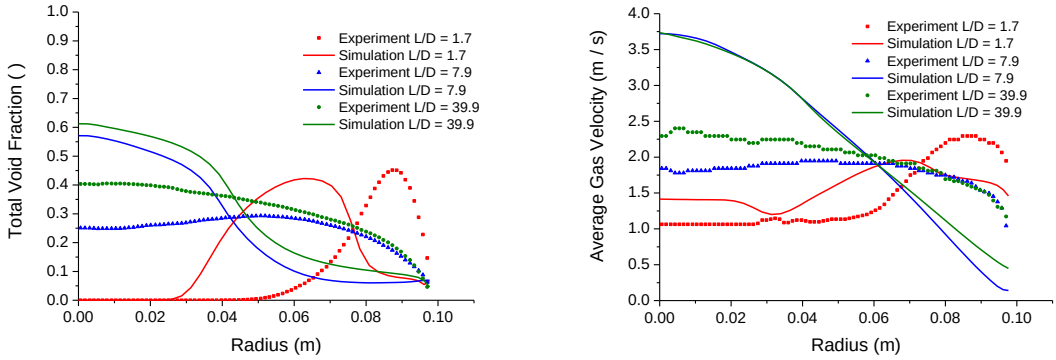

Fig. 5.2 Validation against experiment 129 using a three gas field model for A) radial total void fraction and B) gas averaged velocity profiles.

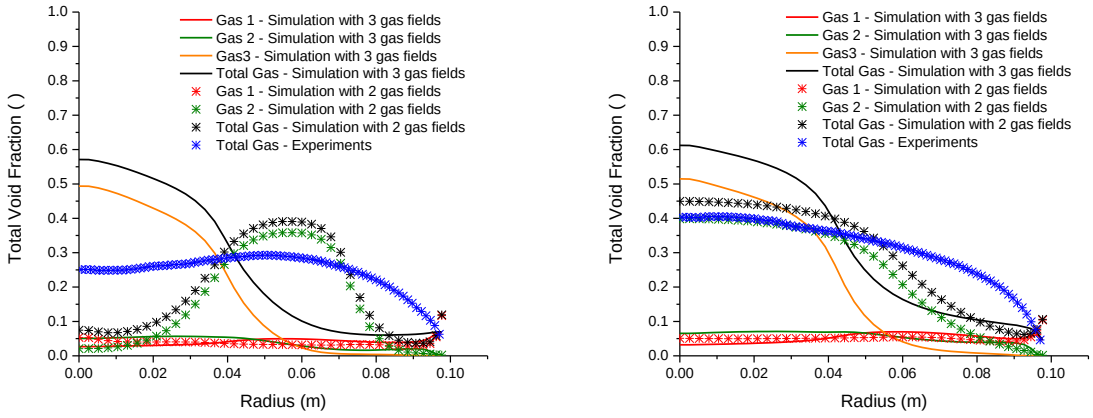

Fig. 5.3 Validation of the radial total and individual contributions of void fraction against the experiment 129 using a two and three gas field model for A) L/D = 7.4 and B) L/D = 39.9.

As expected, the velocity individual contributions for both measurement planes (Fig. 5.4), do not differ much one from the other, and do follow a similar trend as the highest void fraction. It is still observable, that the velocity associated to the third gas field for L/D = 39.9 is around 0.5 m/s higher in comparison to what was observed when the two-field model was used.

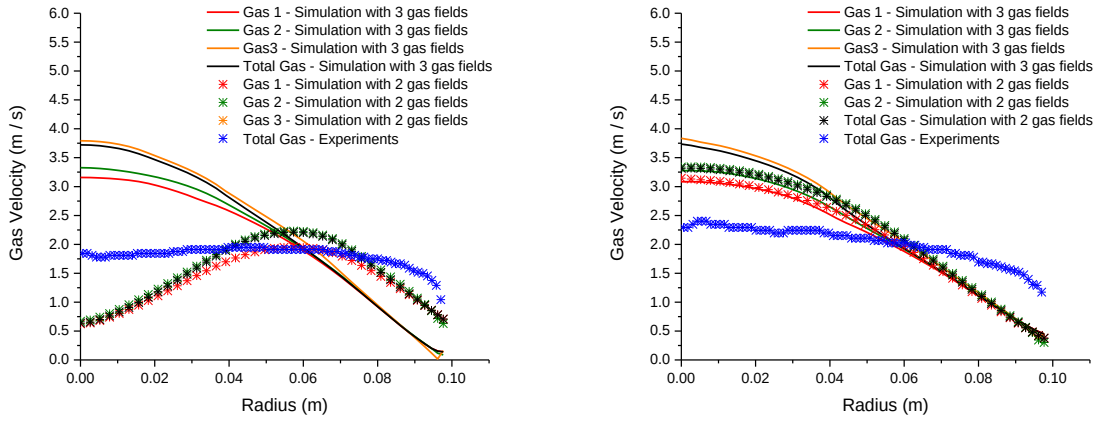

Fig. 5.4 Validation of the gas averaged and individual contributions of velocities against the experiment 129 using a two and three gas field model for A) L/D = 7.4 and B) L/D = 39.9.

The observed behavior led to believe that one of the closure laws which were developed for bubbly flows, is acting too intensely within the third gas-field. At the same time, this is producing a very strong migration of void fraction towards the center of the pipe from an early measurement plane position. Still, deviations were expected when using bubbly flow closure relations for this kind of gas structures. At this point, it seems as if the lift force contribution for the largest bubbles is producing a too strong effect in comparison with the turbulent dispersion force for the present calculations.

Finally, in terms of the bubble size distribution, it seems as if the addition of a third gas field improves the bubble distribution in terms of the over prediction encountered with the two gas field approach for 10 to 40 mm bubble sizes (Fig. 5.5).

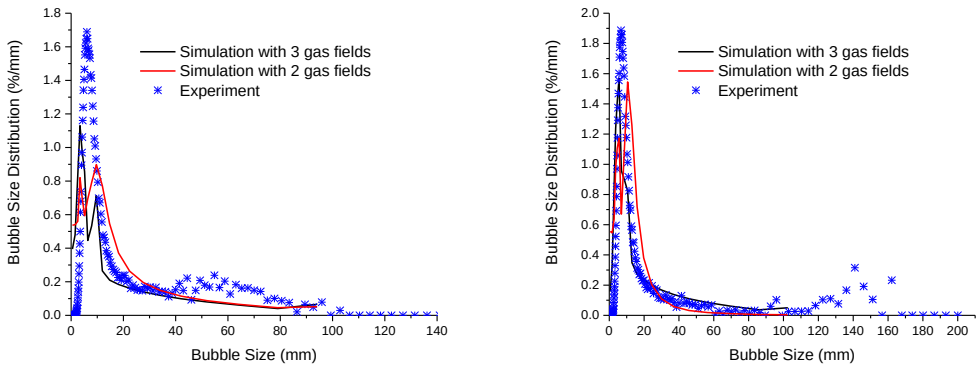

Fig. 5.5 Validation of bubble size distribution against the experiment 129 using a two and three gas field model for A) L/D = 7.4 and B) L/D = 39.9

5.2 Study and modification on the closure laws

5.2.1 Nullification of the lift force contribution in the third gas-field.

As it has been stated before, the strong migration of the third gas-field towards the center of the pipe, seems to derive from an unphysically high lift force. To test this hypothesis, the lift force was completely neglected for the third polydispersed field. The effect on the individual contributions for the radial void fraction can be observed in Fig. 5.6a and 5.6b for an L/D = 4.7 and L/D = 39.9, respectively.

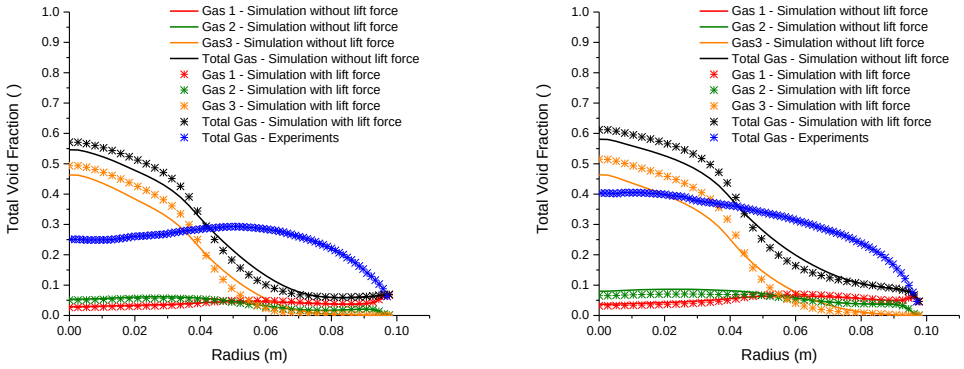

Fig. 5.6 Validation of the radial void fraction contributions against experiment 129 using a three gas field model with and without lift force contribution for A) L/D = 7.4 and B) L/D = 39.9.

In principle, it is quite difficult to see any difference between these results and the ones presented in section 5.1. There has been only a decrease of around 5% in the void fraction core, maintaining the same unphysically strong migration of the third-gas field void towards the center of the pipe for both measurement planes. An expected corresponding effect can be observed regarding the individual and averaged gas velocities as shown in Fig. 5.7. In this case, no decrease in velocity can be observed when compared to the calculation with the complete lift contribution.

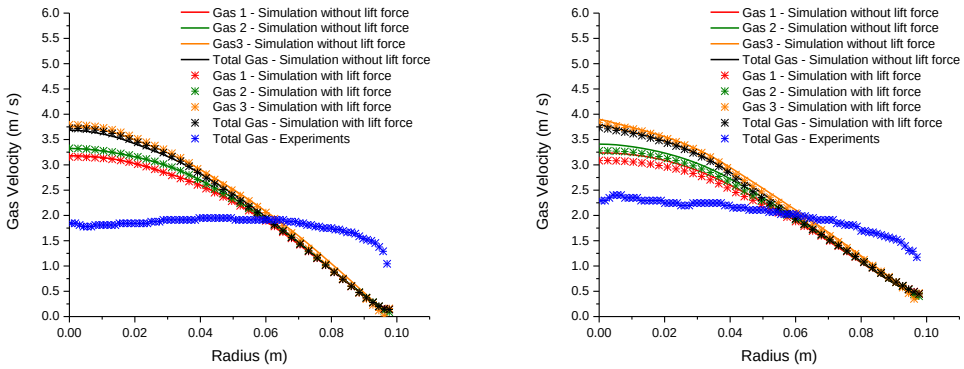

Fig. 5.7 Validation of the gas velocity contributions against experiment 129 using a three gas field model with and without lift force for A) L/D = 7.4 and B) L/D = 39.9.

Since neglecting the lift force appears to have such a small influence over the third gas-field simulations, studies need to be made in order to consider the effect of other forces that could be producing the higher concentration of "Gas3" at the center of the pipe independently of the lift force. An example of this would be the wall lubrication or the turbulent dispersion force.

5.2.2 Nullification of the wall force in addition to the lift contribution for the third gas-field.

Surprisingly, in case of neglecting the wall force, the unphysical void fraction peak vanishes from the beginning to the end of the pipe (Fig. 5.8). The accumulation of gas at L/D = 7.4 close to the wall indicates a too slow transition towards the center of the pipe, contrary to what has been shown in the last sections.

For L/D = 39.9, the void profile converged to a closer value to the experimental data in comparison with the prior calculations. At this last measurement plane, there is still a clear lack of gas in the center-core of the pipe. This correspondingly produces an accumulation of void at the wall, translating into a very flat profile.

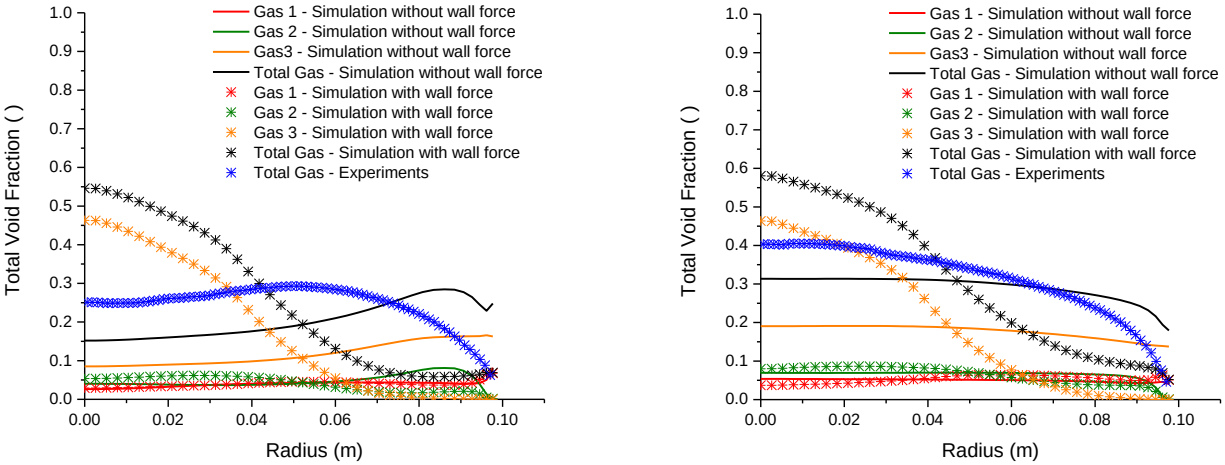

Fig. 5.8 Comparison of the void fraction profiles for each gas field in the three-field model for case 129 with and without wall force and no lift contribution at A) L/D = 7.4 and B) L/D = 39.9.

For the velocity profiles (Fig. 5.9) for the lower measurement plane there is a relatively strong accumulation of "Gas3" at the wall side. This produced an over prediction of gas velocities in this area, and an under prediction when moving towards the center of the pipe. Contrary to that, for higher measurement planes, the averaged gas velocity agreed quite well with the experimental data.

An interesting observation has been spotted regarding bubble size distributions (Fig. 5.10), where there is a clear improvement on the under predictions of the peak produced by the smaller bubbles ("Gas1") from the last calculations in comparison with the experimental data for L/D = 7.4. For L/D

= 39.9, the two calculations are rather similar, with a slight over prediction observed when the wall force is neglected, for bubble sizes from 20 to 60 mm. Furthermore, the current bubble breakup and coalescence models seem unable to achieve bubbles larger than 100 mm, underpredicting the largest bubble sizes for higher measurement planes.

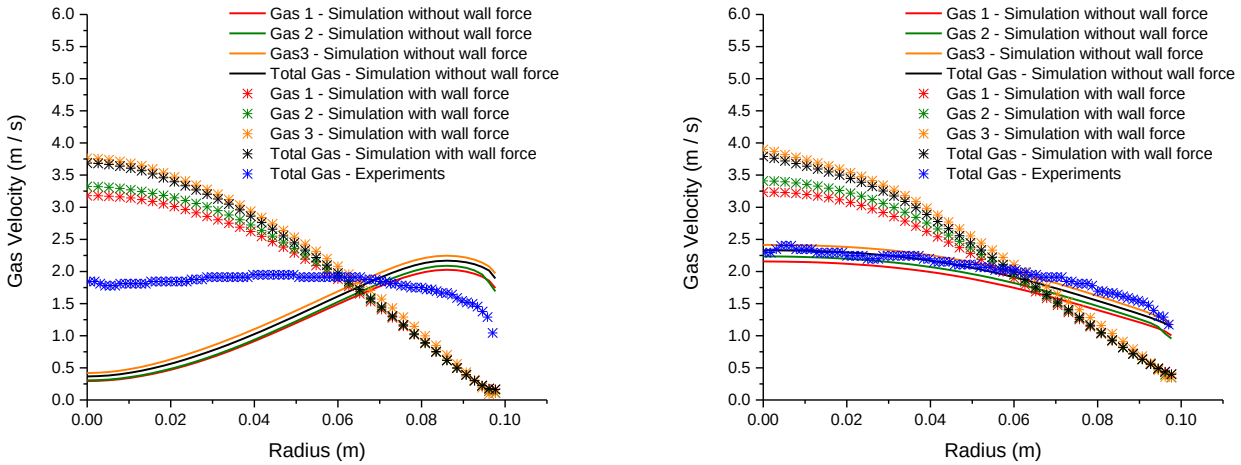

Fig. 5.9 Comparison of the averaged gas velocity for each gas field in the three-field model for case 129 with and without wall force and no lift force contribution at A) L/D = 7.4 and B) L/D = 39.9.

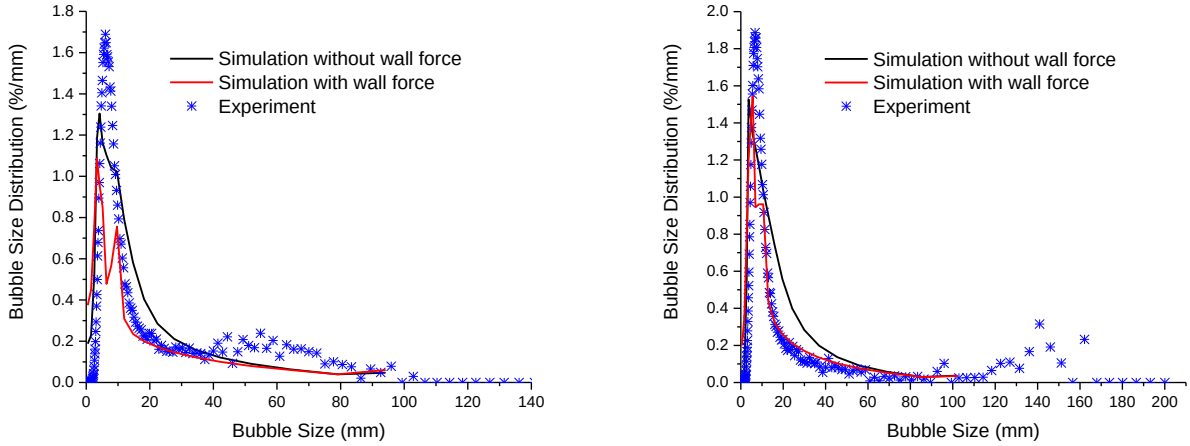

Fig. 5.10 Validation of bubble size distribution against the experiment 129 using a three gas field model with and without wall force and no lift force contribution at A) L/D = 7.4 and B) L/D = 39.9.

Calculations following the same modeling approach for experiments 127 and 118 were also completed in order to confirm the findings observed with case 129.

Clearly from Fig. 5.11a, case 127 follows the same trend as 129 at L/D = 7.4, with a very slow transition from the injection point at the wall side towards the center of the pipe. This also produced a too flat velocity profile. (Fig. 5.12a). When the position of the last measurement plane is analyzed

(L/D = 39.9), a better fit is observed, both for void fraction and velocity profiles, in comparison to the experiments (Fig. 5.11b and Fig. 5.12b). In terms of bubble size distribution, there is slight improvement for bubble smaller than 30 mm, especially for L/D = 7.4, in comparison to the 2 gas fields calculations (Fig. 5.13).

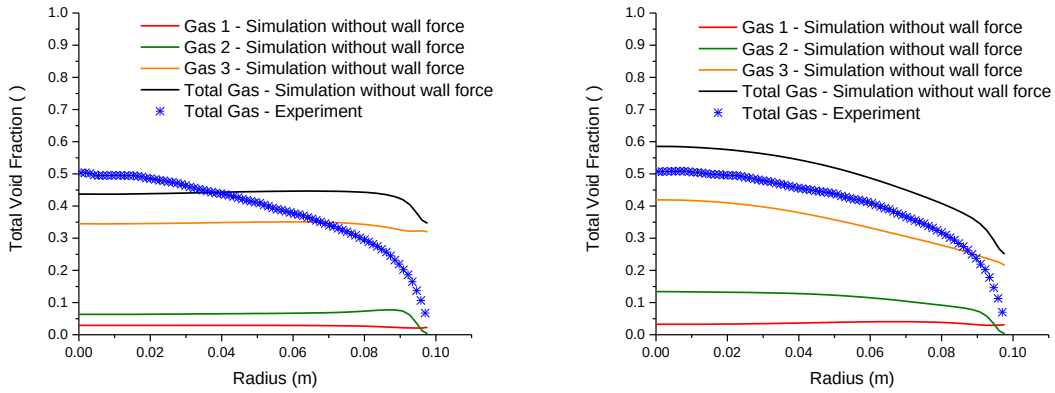

Fig. 5.11 Comparison of the void fraction profiles for each gas field in the three-field model for case 127 without wall nor lift contribution at A) L/D = 7.4 and B) L/D = 39.9.

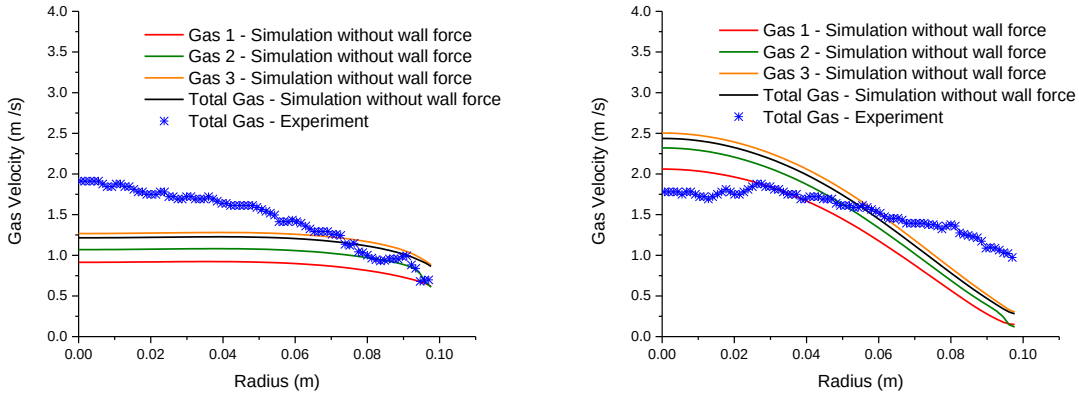

Fig. 5.12 Comparison of the averaged gas velocity for each gas field in the three-field model for case 127 without wall nor lift contribution at A) L/D = 7.4 and B) L/D = 39.9.

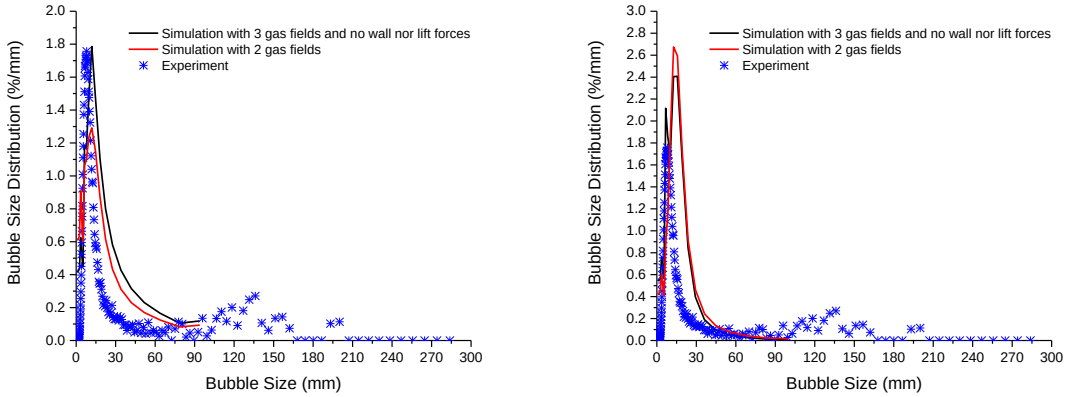

Fig. 5.13 Validation of bubble size distribution against experiment 127 using a two and three gas field model without wall nor lift force contribution at A) L/D = 7.4 and B) L/D = 39.9.

The simulation regarding experiment 118 shows the same trend as the other two cases. Since the overall results are mostly comparable to the ones from experiment 129, the plots for this case are being omitted in this section. Clearly from the previous results, the Hosokawa wall force leads to an unphysical effect for the third gas field, not only acting outside the expected range of the wall lubrication force, but strongly pushing the third gas field towards the centerline of the domain. For that matter, no wall force should be used for the large distorted gas structures.

One more calculation with the latest approach was made using the MT-Loop experiments case 118. This is a developing slug-flow, and the idea was to show that this analysis applies not only to large bubbles in churn-turbulent flow regime (e.g. large distorted bubbles in large pipes), but that the theory applies also to large gas structures in general, including Taylor-like bubbles. Since the MT-Loop vertical test section is significantly smaller than TOPFLOW, the mesh used here is based in a full 3D geometry. Identical dimensions as the base facility were used along with a uniform cell size of 3 mm. This mesh was developed using the ANSYS Design modeler and ANSYS Mesh tools. In terms of the boundary conditions, the same procedure was followed, initializing the liquid inlet boundary using turbulence and velocity parameters from single phase calculations.

As it can be observed from Fig. 5.14, the same behavior applies in this case as it has been discussed in the last section. When no lift nor wall forces are applied, there is an overall overprediction at the wall sides of the pipe, and under prediction of the center-core based on the total void fraction. This is a behavior which is maintained until the last measurement plane for this experiment.

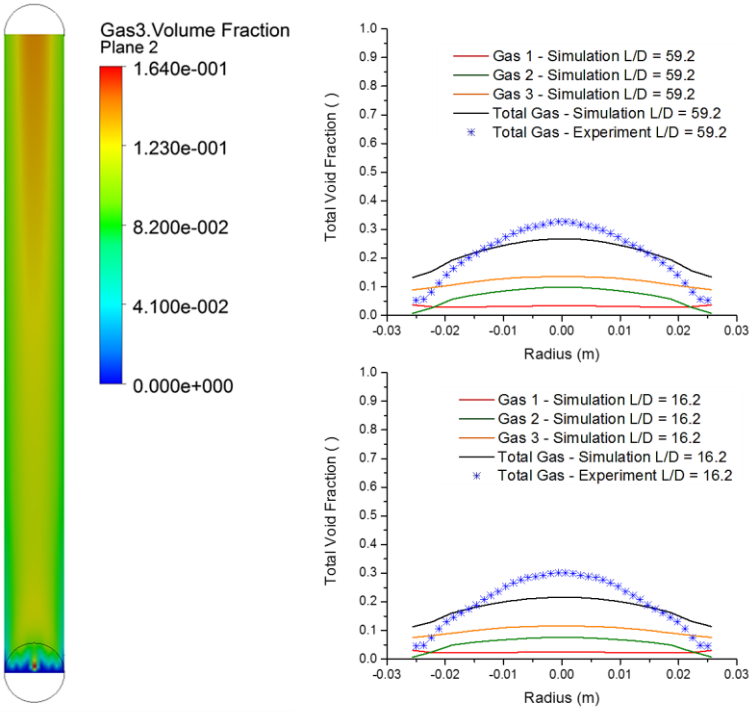

Fig. 5.14 Qualitative and quantitative comparison of the total void fraction in the three-field model for the MT-Loop case 118 without wall nor lift contribution at L/D = 16.2 and L/D = 59.2.

The individual and averaged gas velocity contributions can be seen in Fig. 5.15. While the velocity radial profiles seems to fit the experimental data more accurately, the strongest deviation occurs closer to the center, once again observing a similar trend as with the void fraction profiles.

A similar overall trend as in the TOPFLOW case 118 and 129 can be observed in terms of the bubble size distribution. In this case, a strong under prediction of bubbles smaller than 15 mm can be detected, followed by an over prediction from 20 to 30 mm, finally underpredicitng larger than 30 mm bubble sizes. For lower measurement planes (L/D = 16.2) there is a miss prediction in the calculations of bubbles larger than 25 mm which is not consistent with the experimental data (Fig. 5.16). Based on the difference of accuracy between void and bubble size distribution in comparison to the experimental data, it can be inferred that while the total gas volume fraction distribution (composed by "Gas1", "Gas2", and "Gas3") is acceptably calculated, the coalescence and breakup models are unable to predict the correct bubble size distribution of the sub-size bubble classes within each iMUSIG group.

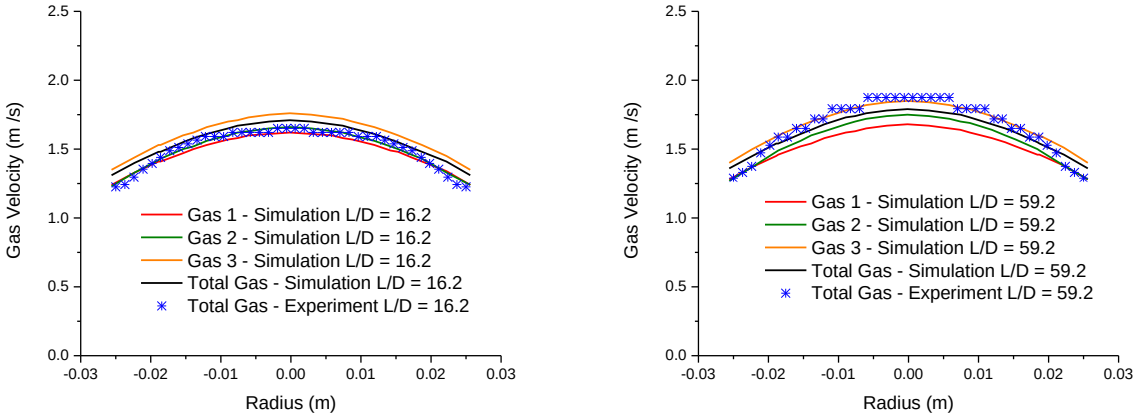

Fig. 5.15 Comparison of the averaged gas velocity for each gas field in the three-field model for the MT-Loop case 118 without wall nor lift contribution at A) L/D = 16.2 and B) L/D = 59.2.

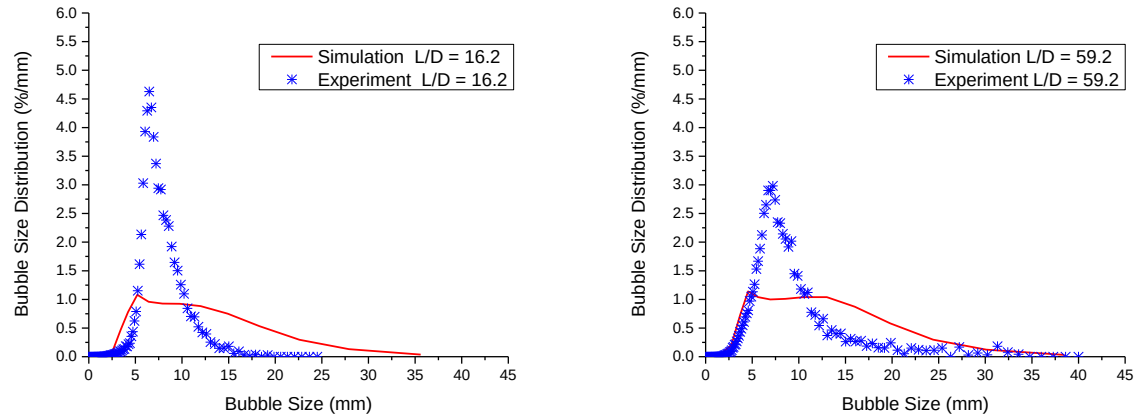

Fig. 5.16 Comparison of the bubble size distribution in the three-field model for the MT-Loop case 118 without wall nor lift contribution at A) L/D = 16.2 and B) L/D = 59.2.

5.2.3 Study of the lift force effect without wall lubrication contribution for the third gas-field.

As shown in the previous sections, nullifying both wall and lift forces leads to an underprediction of the void fraction at the centerline of the tube for all cases. In principle, the lift force should be counteracting this effect. The objective of this section is to study if the lift force contribution alone, could have a significant effect on the third gas field allowing an early push of these bubbles towards the center of the pipe and improving the overall under prediction of void at the center core. A calculation was done based on the MT-Loop case 118, adding the full lift contribution of -0.27 for the third gas field which corresponds to the value provide by Tomiyama et al. (2002) for large bubbles (Eo > 10).

In comparison with the bubble size distribution observed when no wall nor lift is considered, Fig. 5.17a shows a small improvement for lower measurement levels of the overprediction of bubble sizes from 15 to 25 mm. There is still an appearance of bubbles larger than 25 mm, which are not encountered in the experimental data. As the flow developed in the axial direction within the pipe, a closer trend to the experiments is reached (Fig. 5.17b).

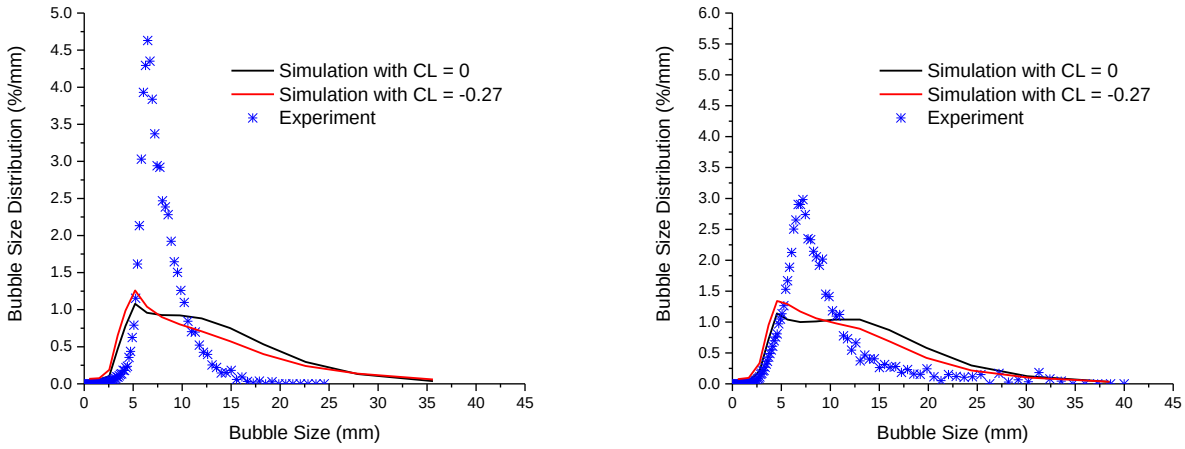

Fig. 5.17 Comparison of the bubble size distribution in the three-field model for the MT-Loop case 118 with a lift coefficient (CL) of -0.27 at A) L/D = 16.2 and B) L/D = 59.2.

The quantitative results regarding total and individual radial void fractions can be seen in Fig. 5.18. Here, it is clear that there is a non-negligible effect of the lift force since very early in the pipe. Coalescence started occurring close to the inlet boundary, and already by the measurement plane located at L/D = 16.2, there is a clear overprediction of the total radial void fraction at the center of the pipe. This overprediction is caused by the third gas field, which shows a very strong concentration of "Gas3" at the center of the pipe close to the inlet. As observed in the analysis of the bubble size distribution for this case, as the flow developed in the axial direction, the coalescence effects increase

and for that matter, the overprediction of the total void fraction is expected to be larger for L/D = 59.2 than for L/D = 16.2. In terms of individual and averaged gas velocities, there is an overprediction at the center core, which, as expected from the latest calculations, follows the trend of the radial void fraction in this area (Fig. 5.19).

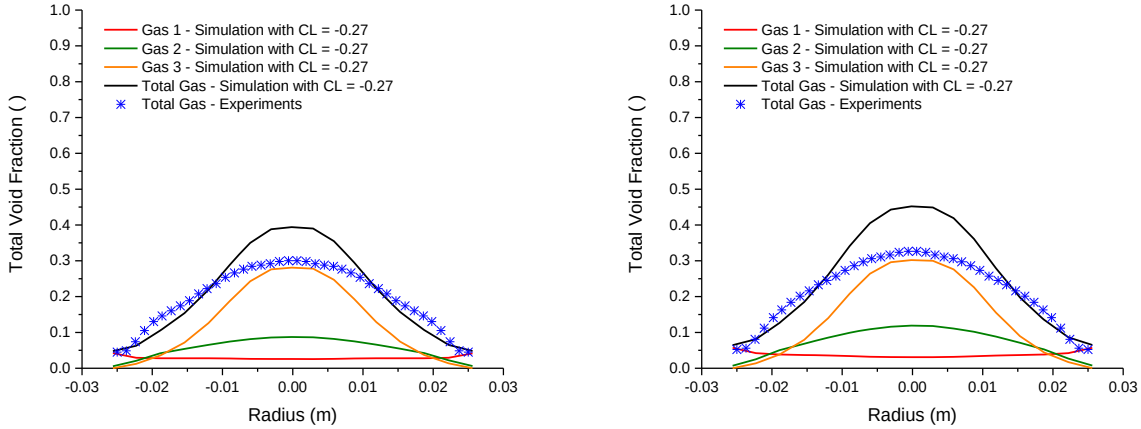

Fig. 5.18 Comparison of void fraction radial profiles in the three-field model for the MT-Loop case 118 with a lift coefficient (CL) of -0.27 at A) L/D = 16.2 and B) L/D = 59.2.

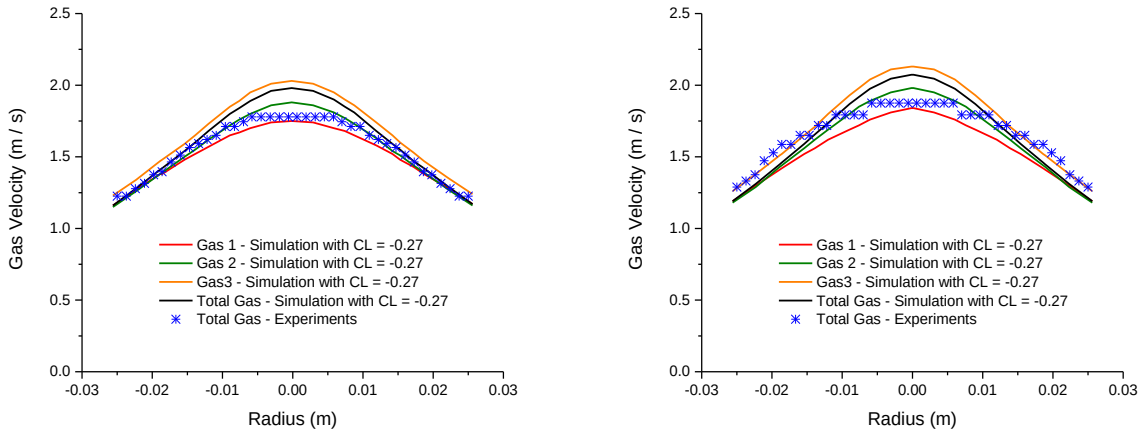

Fig. 5.19 Comparison of velocity radial profiles in the three-field model for the MT-Loop case 118 with a lift coefficient (CL) of -0.27 at A) L/D = 16.2 and B) L/D = 59.2.

These results show that the lift force appears to be acting too strongly in comparison to the turbulence dispersion forces for bubbles which are equivalent to Eo > 10. This comes as a no surprise, since Tomiyama et al. (1998) developed this correlation using experimental data for Eo < 10, and based the -0.27 coefficient as an elegant guess based on his findings for the largest tested bubbles. For this, it is expected that lowering the lift coefficient value for this third gas field, will decrease the migration of these bubbles towards the center of the pipe and further reduce the overprediction of

radial void fraction in comparison to the experiments. If this is true, then it would prove that the coefficient value of -0.27 is simply too large for all sizes which are represented by Eo > 10.

The first test case consisted in lowering the coefficient to -0.14 (half of its original value). Observing Fig. 5.20, it is obvious that the increase of void fraction of the third gas field in the center of the pipe occurs slower for the newer coefficient. It also shows a better quantitative agreement of the radial void fraction when compared to experimental data for lower measurement planes, while displaying still a too strong lift force for the higher positions in the pipe. The velocity profiles (Fig. 5.21), follow once again the same trend as the void fraction radial profiles. Here, the largest divergence in velocity occurs at the center of the pipe where the over prediction of total void fraction was observed. The higher the measurement plane, the stronger the disagreement against experimental data.

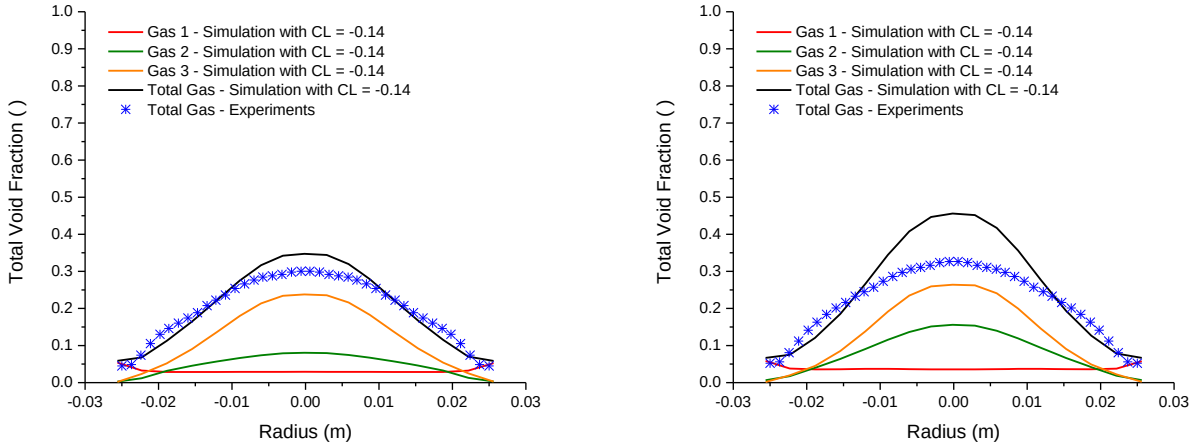

Fig. 5.20 Comparison of void fraction radial profiles in the three-field model for the MT-Loop case 118 with a lift coefficient (CL) of -0.14 at A) L/D = 16.2 and B) L/D = 59.2.

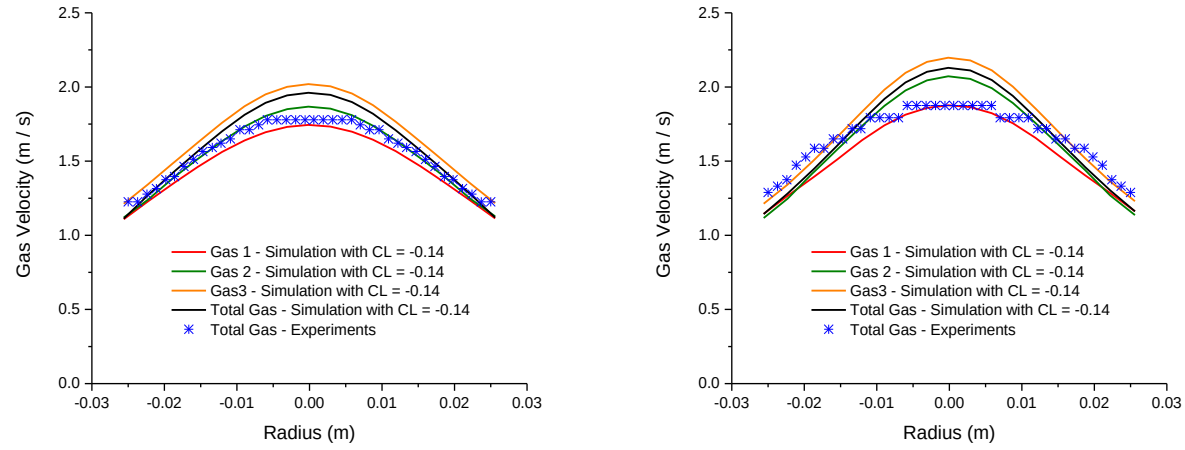

Fig. 5.21 Comparison of velocity radial profiles in the three-field model for the MT-Loop case 118 with a lift coefficient (CL) of -0.14 at A) L/D = 16.2 and B) L/D = 59.2.

In terms of the bubble size distributions (Fig. 5.22), it shows a very similar trend as before for lower levels, accompanied by a relatively higher increase of coalescence for bubble sizes from 5 mm to 20 mm.

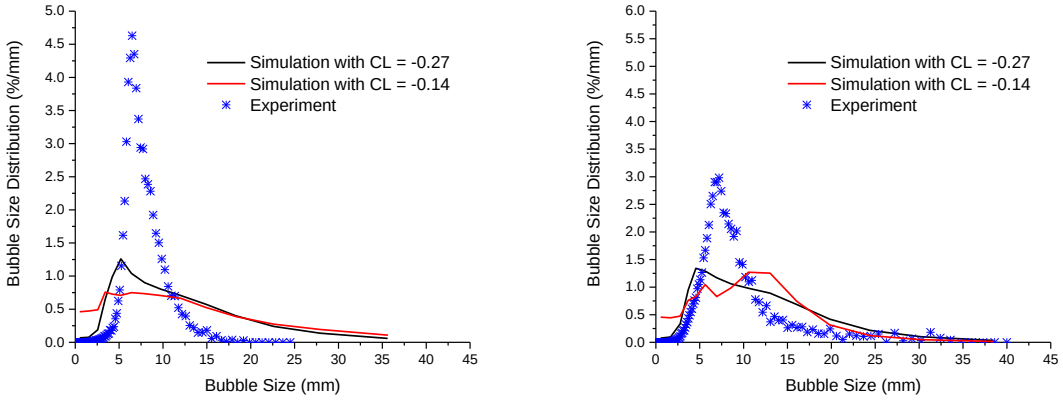

Fig. 5.22 Comparison of the bubble size distribution in the three-field model for the MT-Loop case 118 with a lift coefficient (CL) of -0.14 at A) L/D = 16.2 and B) L/D = 59.2.

As a secondary study for the lift contribution of this third gas-field, the coefficient was lowered to a quarter of its original value (C_L = -0.07). As expected, it can be seen in Fig. 5.23 that the concentration of "Gas3" on the whole domain was significantly decreased. When the individual and total contribution of the void fraction radial profiles are plotted, a significant improvement over the latest calculation (C_L = -0.14) against experimental data is observed. Gas velocity radial profiles (Fig. 5.24) show the same behavior as before, following the same trend of the radial void fractions. An almost perfect match for the lower measurement planes can be seen, while a slight over prediction is observed for higher measurement plane positions (L/D = 59.2). In terms of bubble size distributions, since there is an almost imperceptible change, the plots are not shown here.

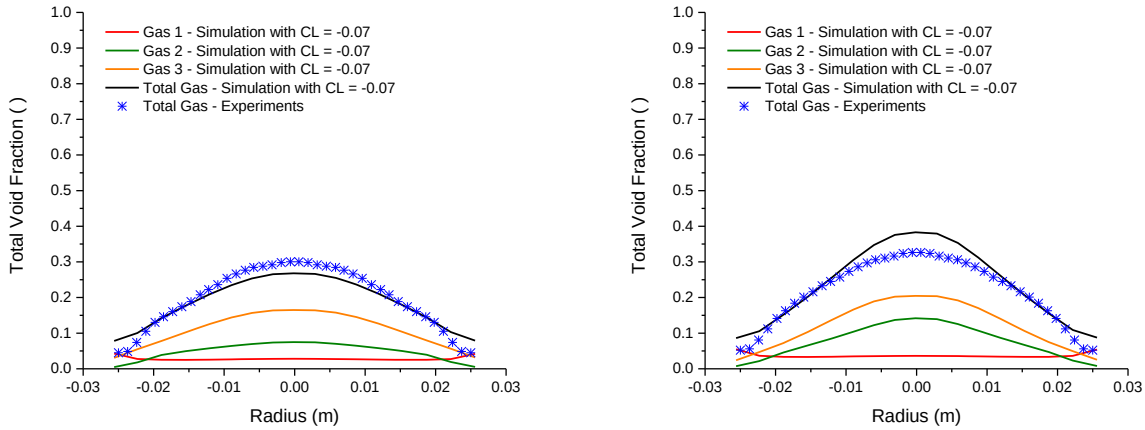

Fig. 5.23 Comparison of void fraction radial profiles in the three-field model for the MT-Loop case 118 with a lift coefficient (CL) of -0.07 at A) L/D = 16.2 and B) L/D = 59.2.

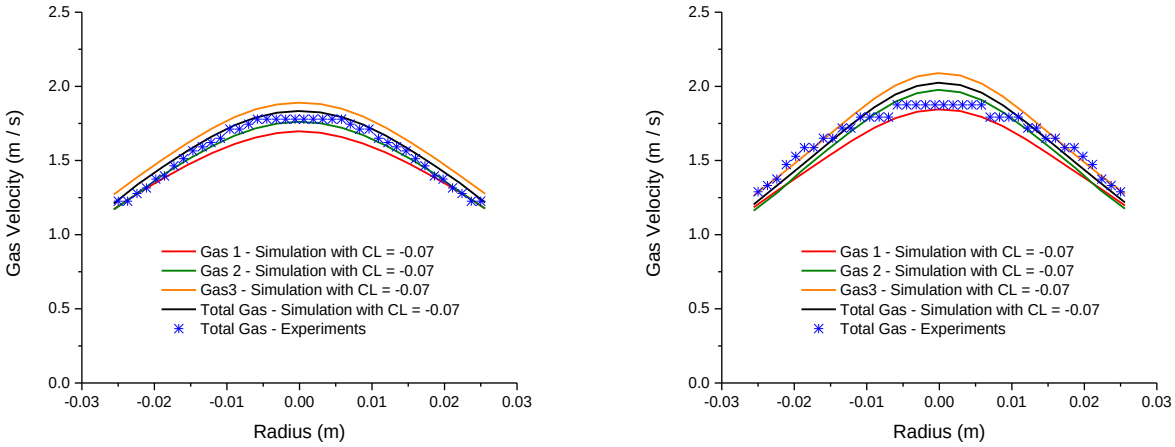

Fig. 5.24 Comparison of velocity radial profiles in the three-field model for the MT-Loop case 118 with a lift coefficient (CL) of -0.07 at A) L/D = 16.2 and B) L/D = 59.2

This trend for the last two calculations, clearly shows how over predicted is the Tomiyama lift coefficient for Eötvos numbers greater than 10, and how large this force is in comparison with the turbulent dispersion.

Of course, there is always the possibility of improving the coefficient for a specific case in order to improve the results. For example, there is a clear relation with the void fraction from the latest calculations. As the void fraction increases in the experiments, the overprediction in the numerical simulation also increases for all previous tests. So, in principle, as the void fraction increases, the lift coefficient for bubbles with Eo > 10 ("Gas3") should decrease. Furthermore, all previous tests also show that the lift force needs to be stronger in lower levels, and then slowly decreases as the concentration of "Gas3" at the center core increases. After some tests, a relation using a hyperbolic tangent function was found to be the most suitable, showing an almost perfect match between experimental data and calculations (Fig. 5.25).

For mesh statistics purpose, the total gas radial profile for three different meshes is also plotted in the same figure, where "Mesh 2" represents the one used for the analyses in this chapter. Each mesh is refined in the radial and axial direction by a factor of 2.

Still, this results belongs, most probably, to a case-dependent solution, and so this is as close as we can get to the question of "which is the real lift coefficient for bubbles with Eo > 10?"

To study the answer of that question in an experimental facility is very challenging since churn-like bubbles are very unstable when they travel alone, and are commonly accompanied by a swarm of bubbles in their wake and surroundings.

In terms of getting the answer from the computational point of view (DNS calculations), it is not a realistic idea with the state-of-the-art computational power.

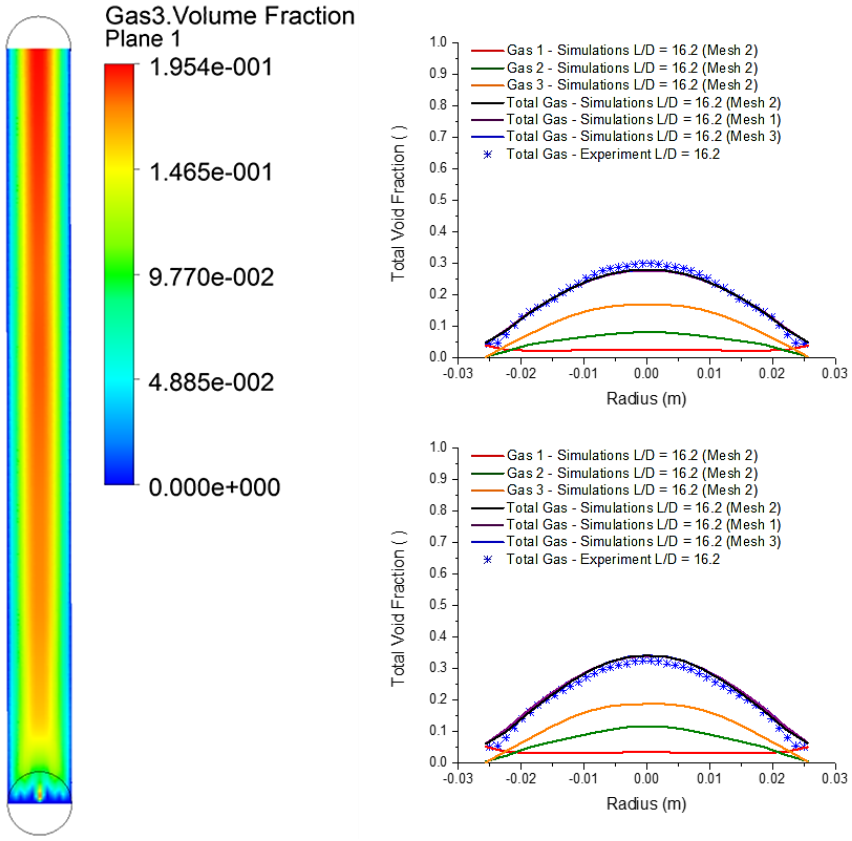

Fig. 5.25 Qualitative and quantitative comparison of the void fraction in the 3-field model for case 118 with lift coefficient -0.27*(tanh(-6*α_{G3})+1) at L/D = 16.2 and L/D = 39.9

5.3 Chapter summary

The inclusion of a third gas field to extend the traditional bimodal distribution for the churn regime (Krishna et al., 2001) was evaluated, and demonstrated, as expected, considerable improvements in the physical representation of churn flow conditions. Nevertheless, results were far from optimal and evidenced considerable limitations. In order to better understand the effect of the model components, separate tests were performed allowing a more complete understanding of the mechanisms behind the churn flow regime, which significantly differ from the bubbly flow conditions.

While considerable improvements are achieved in comparison to the HZDR modeling baseline for high void fraction conditions, an evident limitation is still present in the representation of the large deformable bubbles. These limitations are also amplified by the limitation of the bubble breakup and coalescence models, which are only applicable up to 10mm bubbles.

Promising potential is expected by the adoption of hybrid concepts, such as GENTOP, which relies on the direct resolution of the large scale churn and slug-like gas structures, while modeling the smaller bubbles. This modeling concept would be expected to improve agreement with experiments and physical trends with limited increase in the computational resources.

6 Study on the current limitations of the GEneralized TwO Phase flow (GENTOP) concept for high void fraction regimes

Eulerian-Eulerian multi-fluid approaches are commonly used to predict dispersed flows patterns such as bubbly or droplet flows which are characterized by scales of interfacial structures that are smaller than the grid size. For flow situations where large-scale interface like film, annular, or horizontal stratified flows occurs, usually interface tracking methods can offer a significant resolution advantage. In principle, the interface capturing methods should be utilized for interfacial length scales several times larger than the grid size, while for an averaged two-fluid approach, bubble sizes smaller than the grid size are required.

The clear limitations of using the Euler-Euler approach for simulating high void fraction regimes have been stated and thoroughly studied in this dissertation. The main challenge encountered in these cases is represented by the difficulty of establishing closure laws that can successfully characterize the physics behind the highly deformable large bubbles encountered in these regimes.

Since in the case of high void fraction flows, dispersed gas structures, and large interfaces occur simultaneously, a combination of these modeling concepts is an interesting option to leverage both strengths (Fig. 6.1). While Tomiyama et al. (2006) addressed the open questions regarding the gap in the scales for intermediate range of interfacial structures, combinations of these two basic computational techniques has been proposed by many authors. Černe (2001) explicitly coupled a VOF-method and an interface capturing algorithm with the Eulerian two-fluid model using a switching criterion based on the error of the VOF-method, which depended on the dispersion of the interface. Unfortunately, they were not able to predict the transition from dispersed to stratified flow. Tomiyama and Shimada (2001) proposed a hybrid method using a level-set approach for capturing the interface along with a multi-fluid method, but did not consider bubble breakup and coalescence. Minato et al. (2000) proposed an extended two-fluid model, where large scales were treated with a VOF-method differencing scheme. Later on Strubelj et al. (2009) combined the two-fluid model with a conservative level set method. Within this concept that Strubelj proposed, the interface sharpening method as well as a surface tension model (Brackbill et al., 1992) were validated, but no transitions between small- and large scale gas phases were considered.

A novel concept based on a two-phase four-field modeling technique with continuous and dispersed gas, which also considers phase transfer between different gas morphologies as well as bubble coalescence and breakup, has been developed and validated qualitatively against well-known

cases such as dam-break (Hänsch et al., 2013), impinging jet, and bubble-columns (Hänsch et al., 2012).

This chapter will present the limitations and further development of the current modeling of the concept based on different parametric studies, as well as qualitative and quantitative comparisons of pipe flow cases from experiments at the TOPFLOW and MT-Loop facilities.

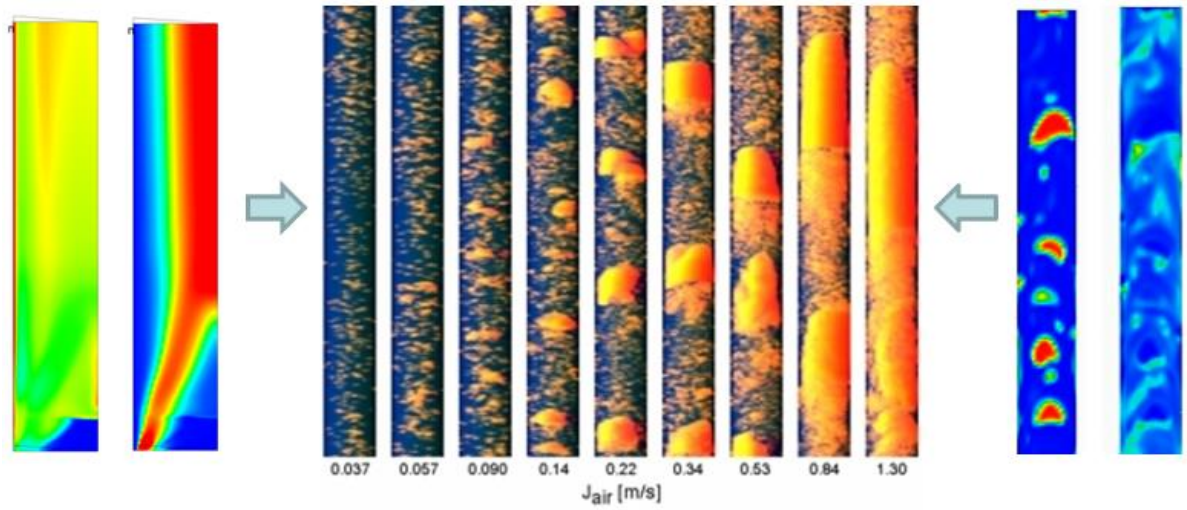

Fig. 6.1 Exemplification of the modeling of different interfacial scales using an Eulerian averaging multi-fluid approach and the GENTOP concept on churn-turbulent flow regime.

6.1 The GENTOP -concept

GENTOP considers the definition of a fully-resolved continuous gas phase where the continuous gas includes all gas structures which are sufficiently large to be resolved within the computational mesh. The concept works as an extension to the iMUSIG concept.

6.1.1 Extending the inhomogeneous MUSIG approach

As already mentioned, the GENTOP –concept has been developed in principle as an extension to the inhomogeneous MUSIG approach, by adding a continuous gas phase. The mass transfer between dispersed and continuous gas is modelled depending on the flow situation, and as a first step to demonstrate the principle, the last velocity group included within the MUSIG framework is considered as the new continuous gas. Later on, more advanced transition models between the dispersed and continuous gas, different from breakup and coalescence inside the dispersed gas fractions via MUSIG definition, have to be developed.

This mentioned "largest" velocity group represents all gas structures which are larger than an equivalent spherical bubble limit diameter $d_{dg,max}$. Early formulations (Hänsch et al., 2012) used a grid dependent threshold diameter $d_{dg,max}$, since it was expected that a complete resolution of the gas-liquid interface occurs only if the continuous gas structure contains several grid cells. A maximum diameter

of $d_{dg,max} = z\Delta x$ was chosen, where z = 4 is based on the knowledge of the smearing of the interface in between 2-3 cells when using the Eulerian approach. In this chapter, it is shown that z = 2, and even z = 1 are acceptable values to obtain a suitable representation of the physical behavior behind the continuous gas.

6.1.2 Tracking of the Interface

In order to resolve the gas structures within the GENTOP concept, the first step is to localize the interface. An appropriate blending function φ_{fs} is used in order to identify the local interfacial structure. Due to the averaged treatment of the Euler-Euler approach, the expected volume fraction discontinuity at the interface has been replaced by a gradient of volume fraction. For that reason, a free surface region is defined using the volume fraction gradient of the continuous gas $|\nabla\alpha_{cg}|$. The interface between the gas and the liquid is characterized by a variation of the volume fraction of $\nabla\alpha_{cg}$ from 0 to 1 over a number of n grid cells of a Δx size, which leads to a critical value $|\nabla\alpha_{cg}|_{crit} = 1/(n\Delta x)$ which allows a definition of the interface. The free surface function is defined as in Eq. 6.1.

$$\varphi_{fs} = 0.5 \tanh\left[a_{fs}\Delta x\left(|\nabla\alpha_{cg}| - |\nabla\alpha_{cg}|_{crit}\right)\right] + 0.5 \tag{6.1}$$

6.1.3 Clustering-method

A clustering force has to be defined, in order to consider transitions from the dispersed towards the continuous gas phase using an aggregative effect within the volume fraction of the continuous gas. The clustering influence has been defined as an additional interfacial force acting exclusively between the continuous gas and liquid phases, and it is included within the interfacial momentum transfer. This force acts proportionally to the gradient of the volume fraction of the liquid, as given in Eq. 6.2.

$$\mathbf{M}_l{}^{clust} = \mathbf{M}_{cg}{}^{clust} = c_{clust}\varphi_{clust}\rho_l\nabla\alpha_l \tag{6.2}$$

The constant defined as c_{clust} was originally proposed to be adaptable to flow regime variations. The validation work, including the ones in the present chapter, have instead indicated that the full clustering force is suitable for very different flow conditions. A constant value of $c_{clust} = 1$ is therefore recommended for the GENTOP application (Montoya et al., 2015). The blending function φ_{clust} is originally defined as in Eq. 6.3, where $\alpha_{clust,min}$ and $\alpha_{clust,max}$ has been originally adjusted based on different qualitatively studied calculations (Hänsch et al., 2012).

$$\begin{aligned}\varphi_{clust} = &\left(0.5 \tanh\left[a_B\left(\alpha_{cg} - \alpha_{clust,min}\right)\right] + 0.5\right) \\ &\cdot \left(0.5\, x \tanh\left[a_B\left(\alpha_{clust,max} - \alpha_{cg}\right)\right] + 0.5\right)\end{aligned} \tag{6.3}$$

6.1.4 Interfacial Transfers

In order to define an accurate interfacial transfer model depending on the corresponding amount of volume fraction presented, transitions between dispersed and continuous gas must be considered. This can be achieved by detecting the local gaseous morphology and by using a similar concept to that of the AIAD-model (Höhne et al., 2011). A transition approach between the closure models is defined by introducing new formulations for the interfacial area density A_D and drag coefficient C_D in order to consider free surfaces for the interfacial transfer of mass and momentum.

The switch between morphologies was originally set to an $\alpha_{cg,crit} = 0.3$, based on the knowledge that bubbly flow rarely exceeds a void fraction between 0.25 and 0.35 when a transition to resolved structures occurs (Griffith et al., 1961; Taitel et al., 1980; Murzyn et al., 2009). Based on a blending function φ_{morph} (Eq. 6.4), the formulations for interfacial area density and drag are defined in Eq. 6.5 and Eq. 6.6.

$$\varphi_{morph} = 0.5 \tanh\left[a_B\left(\alpha_{cg} - \alpha_{cg,crit}\right)\right] + 0.5 \tag{6.4}$$

$$C_{D,cg} = \left(1 - \varphi_{morph}\right)C_{D,bubb} + \varphi_{morph}C_{D,cont} \tag{6.5}$$

$$A_{D,cg} = \left(1 - \varphi_{morph}\right)A_{D,bubb} + \varphi_{morph}A_{D,cont} \tag{6.6}$$

Finally, in order to account for the lift effect on bubbles which are larger than the pre-established limit bubble diameter based on the last iMUSIG group but still have not reached a continuous morphology ($\alpha_{cg,crit} < 0.3$), a lift coefficient formulation has been introduced as shown in Eq. 6.7. This should be set to zero at the moment in which the dispersed gas within the secondary gaseous phase reaches a continuous morphology (Montoya et al., 2014a).

$$C_L = \left(1 - \varphi_{morph}\right) \cdot (-0.27) \tag{6.7}$$

Further details on the original formulation of the interfacial transfer for the GENTOP concept can be found in (Hänsch et al., 2012; Montoya et al., 2014a).

6.1.5 Complete Coalescence

A special coalescence method for complete gaseous mass transfer is included in the model and represents a practical approach to enforce complete coalescence inside a resolved gas structure. This is a simple approach, to enforce the basic principle that small bubbles cannot occupy the same space where large gas structures exist. More information about the original implementation of the complete coalescence model can be found in (Hänsch et al., 2012; Montoya et al., 2014a).

6.2 Computational grid and boundary conditions

Two cases from TOPFLOW (experiment 129) and MT-Loop (experiment 118) were selected for the validation of the present model. Consistently with previous simulations, the data corresponding to the inlet conditions at the liquid continuous phase in the multiphase modeling (turbulent kinetic energy, and turbulent eddy dissipation) were taken from fully developed single phase simulations performed on the same computational grid, while the velocity profile was calculated from the experiments. The inlet boundary conditions for the gas phase have been taken from the experimental data given by TOPFLOW at L/D = 1.1 and by MT-Loop at L/D = 0.6, including gas velocity, mass flow rate, and size fractions.

The experimental data regarding the gas phase was arranged in principle into three velocity groups in the same manner as with the polydispersed calculations. It was then found that the first limitation of the concept for both the MT-Loop and TOPFLOW cases, is the fact that neither the Luo-Svendsen / Prince-Blanch nor the Liao bubble coalescence and breakup models, were able to produce enough coalescence from "Gas1" and "Gas2" into "Gas3" in order to allow the formation of the continuous structures. For that matter, all future cases from GENTOP based on the MT-Loop and TOPFLOW experiments will consider instead two gas fields. The first one ("Gas2"), a polydispersed field with bubble sizes up to 5.8 mm based on the change of sign from the Tomiyama lift coefficient, and the second one ("Gas3") representing the continuous gas based on everything larger than 5.8 mm.

The computational models have been constructed to replicate the experimental conditions of both the TOPFLOW and MT-Loop experiments. Two different meshes are therefore used for the calculations shown in this chapter, and are based on full 3D geometries of the experimental setup. The first of them is based on the TOPFLOW facility, and used structured meshes with a constant size of 7 mm, while the second one is based on the MT-Loop facility, and adopts a cell size of 3 mm. The meshing software utilized were ANSYS ICEM CFD, ANSYS Design Modeler, and ANSYS Mesh (Fig. 6.2).

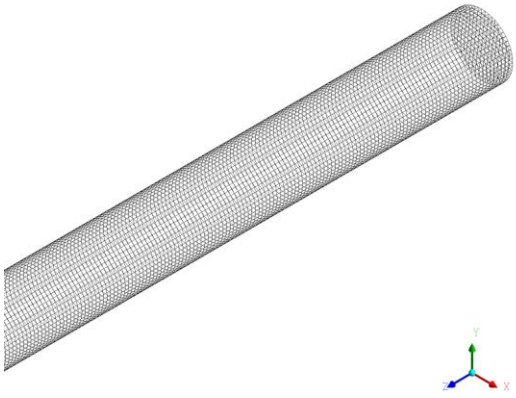

Fig. 6.2 Section of the 3D homogeneous mesh for the MT-Loop calculations with 3 mm cell size.

6.3 Results of the calculations and discussions

A first set of calculations for the TOPFLOW case 129 were performed to evaluate the effect of symmetry conditions within the GENTOP concept. It was shown, as expected, that only full 3D transient calculation could produce accurate results using this approach. While the study on the symmetry conditions is not shown here, for brevity, details are available in Montoya et al., (2014a).

When qualitatively observing the 3D calculations from TOPFLOW case 129, some important features typically encountered in the churn-turbulent flow regime can be seen. As it can be observed from Fig. 6.3, continuous (left side) and dispersed (right side) gas was injected at the wall sides of the pipe. As the dispersed gas grows to the last MUSIG group becoming continuous, the negative lift coefficient starts increasing, and the gas starts moving towards the center of the wall. Here potentially-continuous gas entrains and coalesces forming larger deformable churn-like bubbles. As these bubbles churn through the pipe, they entrain dispersed gas in their wake, as it has been observed also from the experimental data. Some striping seems to occur with the volume fraction of the potentially continuous gas before moving towards the center, but it does not seem to be significant.

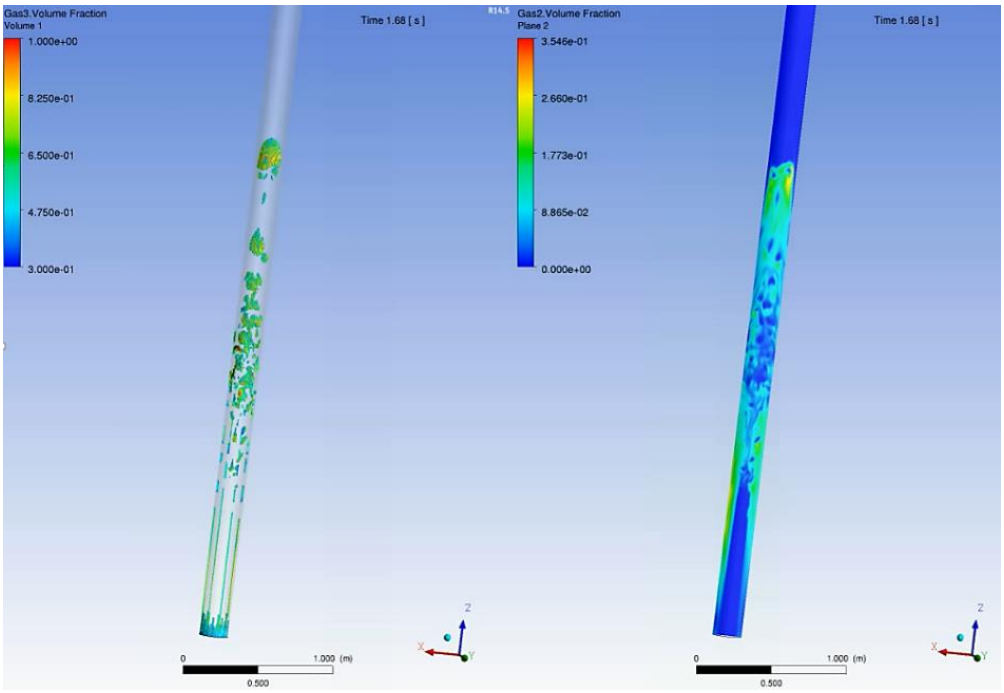

Fig. 6.3 Representation of A) iso-volume ($0.3 < \alpha_{cg} < 1.0$) of the potentially-continuous "Gas3" and B) plane contour of the dispersed-field "Gas2" from TOPFLOW case 129 (t = 1.68 s)

A qualitative view of MT-Loop case 118, allows to observe a very different behavior than that of the TOPFLOW simulations (Fig. 6.4). In this case, for the first half of the axial domain, instead of obtaining a relatively quick dispersion of the inlet gas injection from the sparger, there is an increase of the void fraction in the center of the pipe.

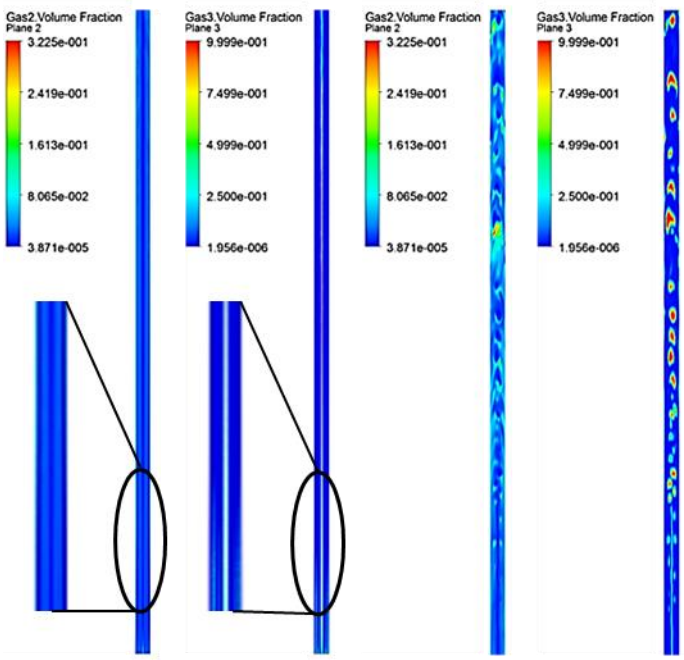

Fig. 6.4 Representation of A) Plane contour of the first half and B) second half of the pipe on an MT-Loop simulation based on case 118 using the GENTOP –concept.

When comparing against the experimental data for quantitative analysis, a good prediction in terms of the bubble size distribution for the polydispersed gaseous phase ("Gas2") can be observed (Fig. 6.5). As expected, as the bubble size increases, the experiment and simulations start diverging from each other due to the inability of current bubble breakup and coalescence models for predicting large bubble sizes, as it was shown in previous chapters. Later on in this dissertation, a more complete analysis of the bubble sizes will also be given by studying the distribution of the continuous gas.

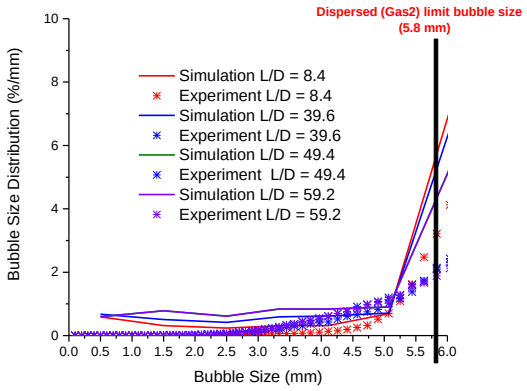

Fig. 6.5 Validation of dispersed gas ("Gas2") bubble size distribution against the MT-Loop experimental data case 118.

In terms of radial void fraction, the strong peaks observed before in the qualitative analysis for almost half of the pipe, can also be seen in the quantitative comparison (Fig. 6.6). While in the experiments, the total void fraction is almost completely dispersed by an L/D = 8.4, it is not until an

L/D = 39.6 that the total void fraction in this simulation begins to disperse. An acceptable agreement against the experimental data is obtained until L/D = 49.4, which further improved by L/D = 59.2. In terms of averaged and individual gas velocities as expected, the higher peaks occur where the maximum of larger bubble sizes ("Gas3") are, and improved when increasing the height of the measurement plane position.

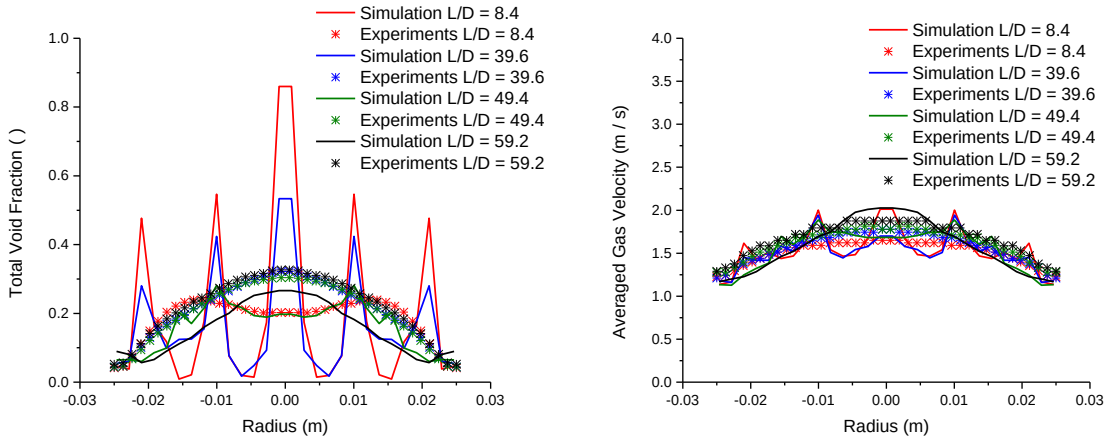

Fig. 6.6 Comparison of A) the radial total void fraction and B) averaged gas velocity against the MT-Loop experimental data case 118.

In the beginning, it was thought that the striping effect was being caused by the clustering force acting too strongly in the direction of the gradient of liquid volume fraction, and for that matter, pushing too strongly the continuous gas towards the center of the domain. It was thought that a possible solution could have been to consider lowering the coefficient C_{clust} which, as it was explained before, allows to control the intensity of the clustering force. A test case was considered, lowering this coefficient from 1.0 to a value of 0.1 (Fig. 6.7). As it can be seen, there is nearly no change in the overall profile in terms of the lack of void fraction radial dispersion, having a decrease at the center of the domain of only $4 \cdot 10^{-2}$.

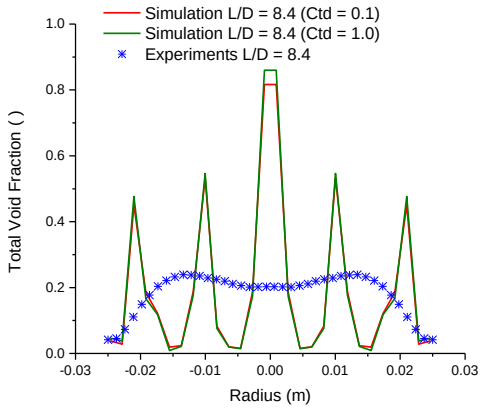

Fig. 6.7 Validation of the radial total void fraction considering a C_{clust} = 0.1 and C_{clust} = 1.0.

Another possible reason for the long stripes observable in the simulations, could be due to the idealized conditions in the URANS models, and so the problem is expected to vanish if large eddies would be resolved. Another possible solution could be considering the time dependent cross section averaged void fraction from the measurements which can have a certain important perturbation at the inlet boundary condition. The dependency on the frequency of such perturbation was investigated and will be discussed in the next chapter.

Another problem that was observed in prior implementations of the concept, as for example in bubble column cases, was that the continuous structures after being resolved used to lower their velocity, and then increase it again. After a complete check of the implementation, it was found that in the complete coalescence model, a misconception of the momentum of the continuous phase was made. Here, after the complete coalescence was activated, the dispersed gas that remained in the cell was transformed into continuous gas, transferring all the mass from dispersed to continuous morphology but the velocity was set to zero. This defined velocity produced an unphysical behavior within the continuous structures in the domain.

The deviation was corrected by considering a velocity equal to the dispersed gas local velocity, being able now to conserve momentum. This is a behavior which is easier to observe in a qualitatively frame per frame analysis, than in a time averaged velocity comparison. As an example, a slightly faster slug for the same time value can be observed in Fig. 6.8 in a 3D iso-volume representation of the flow for the same case based in void fraction of continuous structures ($0.3 < \alpha_{cg} < 1.0$).

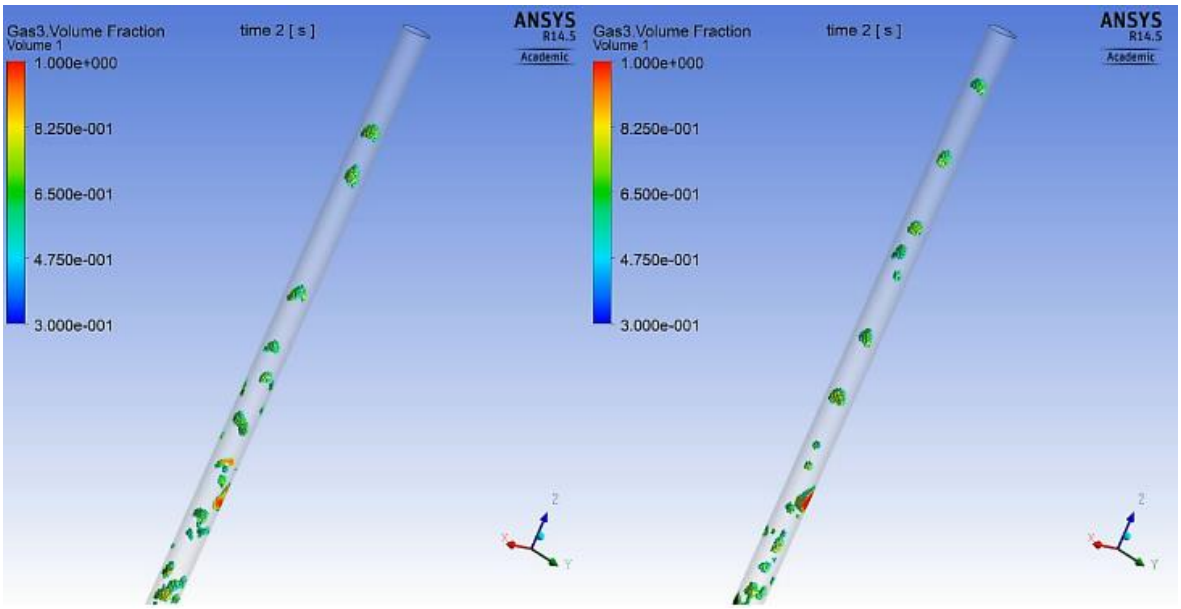

Fig. 6.8 Iso-volume representation of $0.3 < \alpha_{cg} < 1.0$ A) without and A) with the correct implementation of the complete coalescence method.

Another important effect that can be observed in all the studied cases is the increase of void fraction near to the wall of the pipe (Fig. 6.9a). It can be seen that in every calculation, when a bubble gets too close to the wall, the interface disappears, and the gaseous continuous structure gets a void fraction close or equal to unity. This occurs because there is a lack of surface tension at the free surface region, and so there is nothing to push the bubble away from the wall once that goes in contact with that boundary. While this effect can only be observed as a small peak close to the wall side when studying the radial void fraction of higher measurement levels (Fig. 6.9b), this could also be producing an underprediction of void fraction at the centerline of the pipe in time, since the bubble is, in theory, not expected to move during a long time at the side of the boundary wall layer.

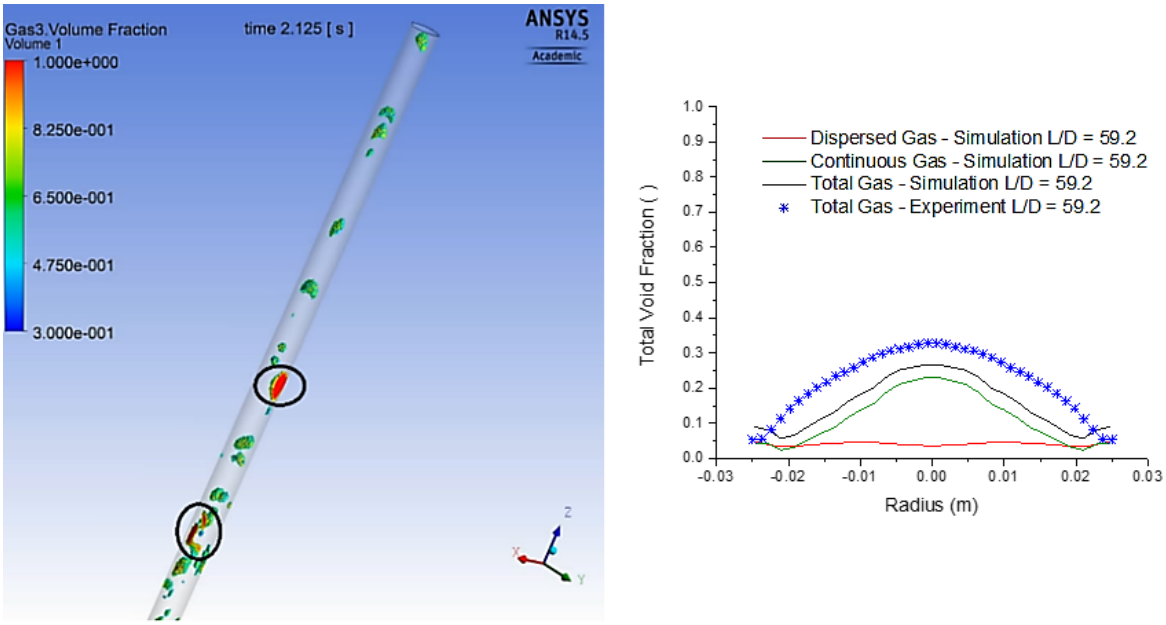

Fig. 6.9 Representation of A) iso-volume where a void fraction equal to one can be found at the wall boundary layer, and B) void fraction radial distribution where the overprediction of void is observable at the wall sides for case 118 of MT-Loop.

Another assumed condition in prior calculations, is that of a free-slip boundary condition for all gaseous phases. This assumption allows the gas to move freely at the wall cells without lowering its velocity. While this condition is applicable for the polydispersed gas, at the moment in which the secondary gas phase becomes a continuous structure, then the condition should not be applied anymore, since as a continuous fluid, a wall friction effect is supposed to occur, lowering the corresponding velocity of the continuous structure close to the wall.

For that matter, a no-slip boundary condition has been established for the continuous gas. In order to study the effects of this change, the radial velocity profile for the total gas phase, and the radial profile for the void fraction are shown (Fig. 6.10a, and 6.10b). In those cases, only the last two measurement levels are shown, not taking into account the “transitional or striping zone” mentioned

earlier in the discussion. Furthermore, even for L/D = 49.4 unphysical peaks are observed, which comes as a consequence of this prior striping of void fraction.

As it can be observed from these figures, the effect of considering a non-slip boundary condition affects the whole radial profile, diminishing the values of velocity for the continuous gas, especially when getting closer to the center of the domain. As expected, since the continuous gas represents the higher void fraction within the domain, it dominates the velocity within the pipe, and so the values of velocity with or without considering the dispersed gas are almost equal. Furthermore, the effect of the no-slip boundary condition, not only affects the radial profile of the gas velocity, but it also has an effect in the volume fraction radial distribution of the gas, slightly reducing the total void fraction in the center of the pipe.

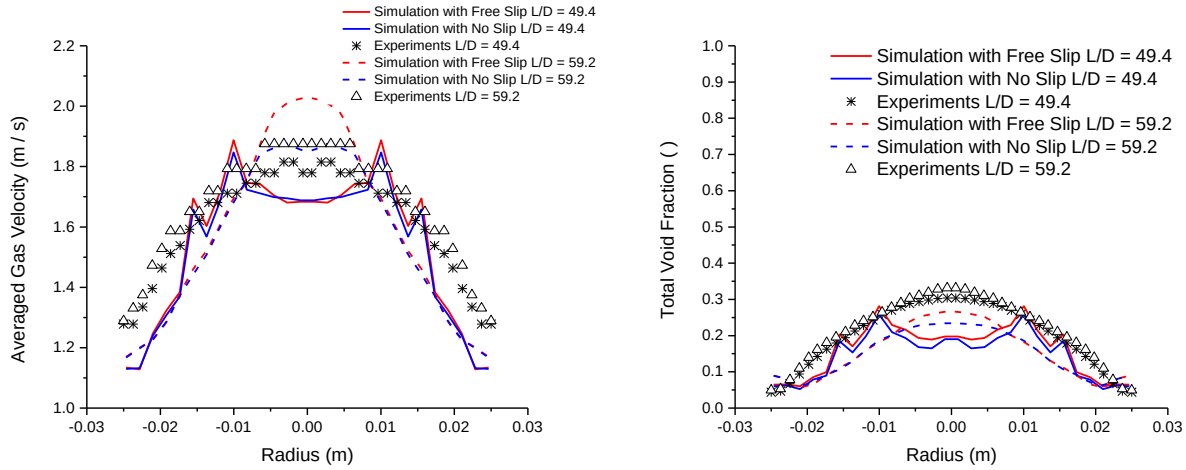

Fig. 6.10 Comparison of A) averaged gas velocity and B) total void fraction profiles against the last two measurement levels for case 118 of MT-Loop.

Finally, another important aspect to discuss is the resolution of the continuous structures. Theoretically, it is assumed that a continuous bubble is completely resolved when it contains a non-trivial number of cells within its domain where the void fraction is equal to, at least, 0.9999. This resolution has been proven difficult to achieve since the beginning of the concept. Commonly, apparently-resolved bubbles contain values of void fraction of around 0.9700 to 0.9900. While with these values, the apparently-resolved structures have been able to reproduce the expected behavior of the flow, especially for higher measurement planes in pipe flows, the problem needs to be addressed and solved in order to improve the morphology, and for that matter the behavior of the continuous gas.

A possible solution would be to consider a fourth field in order to fully model the possible dispersed liquids or drops forming inside the continuous gas. Since that is not a trivial task, an intermediate step in order to improve the resolution of the bubbles could be to lower the drag

coefficient for the drops, in order to make the liquid within the continuous gas fall towards the liquid wall-film of the bubbles. Two calculations were made in order to consider a parametric study, where the drag coefficient of the drops is lower than its original value of 0.44, to 0.22 and 0.001. While in both cases, the apparent resolution of the bubble considering a void fraction inside the continuous gas of 0.97, 0.99, and 0.9999, seems to improve (Fig. 6.11), the refinement is rather insignificant for the destabilization effect that lowering this drag coefficient produces in the overall calculation.

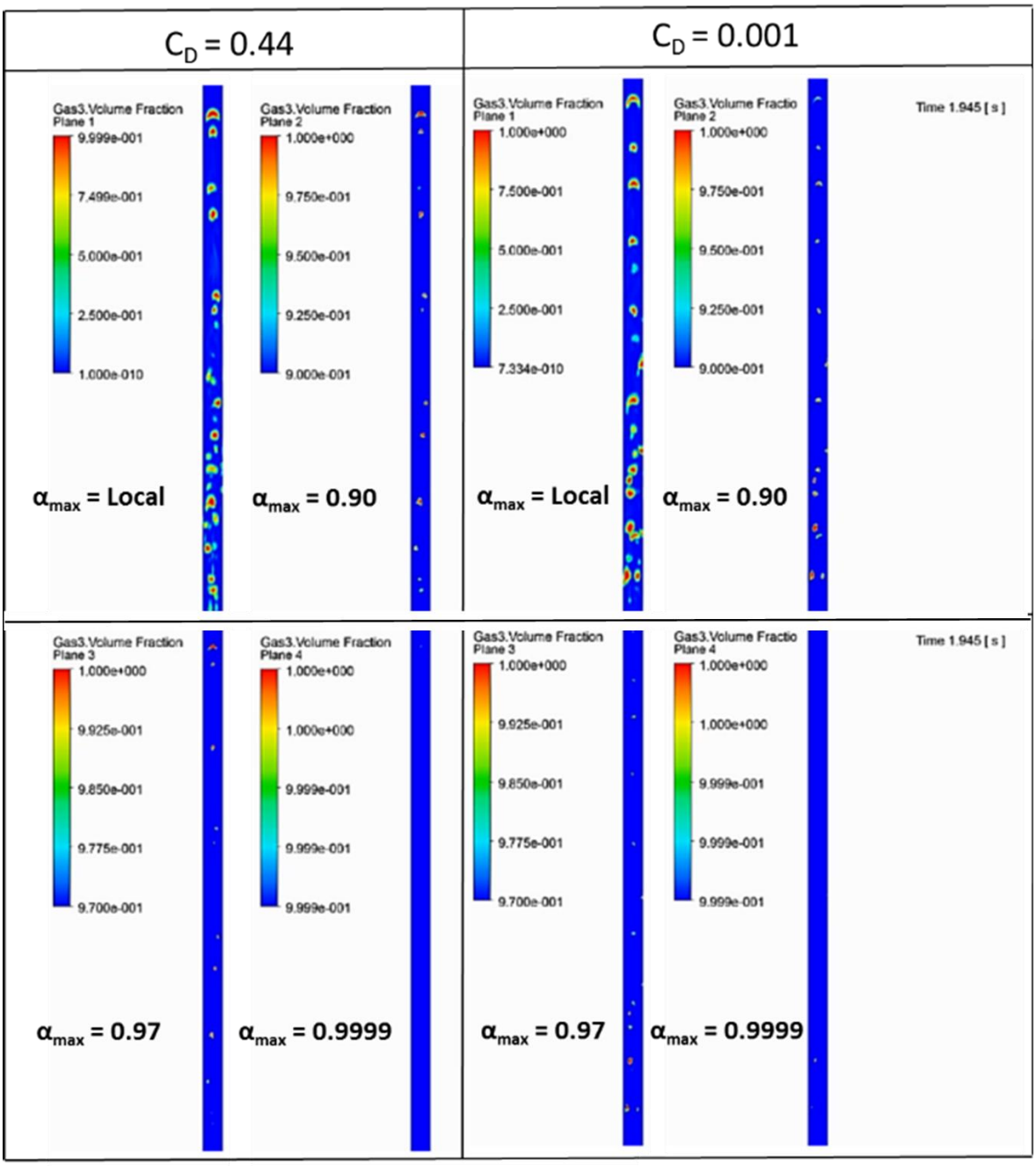

Fig. 6.11 Plane contour representation of the continuous gas for the study of bubble resolution.

6.4 Chapter summary

This chapter has shown a series of studies for high void fraction regimes when treated as multi-scale problems. The results have shown that a multi-scale approach to multiphase simulations, where large deformable gas structures are explicitly resolved on the base of physical subgrid models, has the potential to reproduce the experimentally observed flow behavior both in a quantitative and qualitative way. Here, acceptable predictions for the fully developed flow region of the experimental setup was shown, while shortcomings were still observed during the flow development.

The evidenced limitations have been discussed here, and preliminary solutions have been proposed and are being assessed. It has also been noticed that the specific challenges observed in the first half of the pipe (transition zone), are accented with the specific sparger injection in the small diameter pipe. This does not seem to represent a strong issue in the larger TOPFLOW vertical test section. At the same time the physical approach behind the clustering method and the other forces within the original concept must also be updated, in order to produce a more general implementation independently of a critical value of volume fraction.

Finally, while previous works (Hänsch et al., 2012) had proposed a switch between morphologies at $D_B = 4\Delta x$, the previous results seem to suggest that the concept has sufficient grid independency to consider even $D_B = \Delta x$, and still obtain acceptable resolution of the flow at an L/D = 59.2. These findings indicated that the GENTOP concept might be applicable to relatively low computational resource analyses for fast industrial scale turnaround times.

7 Improvements on the GEneralized TwO Phase flow (GENTOP) concept for high void fraction regimes

This chapter deals with a series of important enhancements over the original GENTOP formulation, with the objective of improving the physical representation and increase the generality and robustness of the concept. These improvements includes changes on the closure components, generalization of key formulations, and addition of surface tension and wetting angle for the free surface region. Furthermore, all modification are then validated against a large number of empirical and analytical data. The enhancements shown here improve on all and every limitation observed in the previous chapter for high void fraction regimes.

7.1 Improvements on the GENTOP general formulation

The most important changes made within the main model can be separated into three main categories: discretization, interface transfer, and clustering force.

7.1.1 Discretization

In terms of discretization problems, there used to exist two main limitations within the model, one based on time and the other on space discretization. The space discretization problem of the model was related to the algorithm for the definition of the free surface area, also known as φ_{surf}. This algorithm completely depends on the characteristic length of the cell Δx. If the value of the characteristic length is over predicted or under predicted, then φ_{surf} could detect a false interface. This problem has been significantly limiting the GENTOP model to homogeneous meshes, which made it completely useless for complex geometries, and for that matter for industrial applications. Since the aim of this project is to model high void fraction regimes with possible future applications to boiling in safety systems and nuclear reactors, the issue must be resolved.

One possible method was to use a CFX internal function called “Volume of Finite Volumes”, which in principle should give the real control volume of a cell as it is used by CFX for the resolution of the continuity and momentum equations. If the mesh is of cubic-like shape, then an approximation based on the cubic root of the function gives a good estimation of the characteristic length. If the mesh is instead cylindrical the calculation largely diverged from the beginning. The problem is that the “Volume of Finite Volumes” function is evaluated on the vertices of the mesh. Then, the routine which used this information is called in the center of the elements and not in the integration points. For this variable in particular, CFX cannot interpolate this information from the vertices to the center (or from the vertices to the integration points), and then it crashes after the initialization. A functional workaround to this issue was found by post-processing the initialization file, and extracting the correct

information of the volume of finite volumes for the whole domain. Finally, this table can be initialized with the previous simulation in order to read all the control volume information from it. This improvement allows the use of more complex meshes for the rest of this thesis such as O-grid and finer nodalization close to boundary conditions.

The second problem based on time discretization was related to the algorithm for the complete coalescence model for which the time step had to be given explicitly. This highly limited the model's robustness, as for example, when a non-equal nodalization is defined within the mesh. When that occurs, then it is more advantageous to define a time-adaptive discretization method for the transient calculation. This problem was resolved by explicitly defining a function for the time step value in each iteration.

7.1.2 Interface transfer

The first change within the interface transfer model which is worth mentioning has to do with the drag force coefficient for the dispersed part of the potentially-continuous gas phase. Up to this point, the drag force coefficient for "Gas3" before it reaches a specific critical void fraction value, was defined based on the Ishii-Zuber correlations but taking into account the swarm effect correction. While the swarm factor effect is absolutely necessary for "Gas3" when this phase is modeled as polydispersed gas, it is completely inconsistent when using GENTOP. As the void fraction increases, the swarm factor correction will effectively decrease the drag coefficient in order to account for the probability of groups of bubbles moving together. In case of a resolved GENTOP-like gas structure, that means that the drag would be reduced not only by the morphology blending function (φ_{morph}), as accounted by the AIAD model, but also by the swarm factor effect. Furthermore, φ_{morph}, as it has been stated before, it depends on a critical void fraction value for blending in and blending out. This value could not necessarily agree with the formation of the interface. That means that the dispersed drag coefficient could be used inside the free surface, producing a larger underprediction of the effective drag coefficient. All this could bring large discrepancies in the velocities of the resolved structure as a whole, and even compromise the integrity of the bubble.

This becomes clearer when the void fraction in both cases is observed. The main difference between Fig. 7.1a and Fig. 7.1b, is the quantity of bubbles which can be observed in the domain for exactly the same time step. It is clear that there is a larger number of resolved continuous structures when the drag correction is avoided. Furthermore, while most of the continuous gas structures in Fig. 7.1b appeared to be coherent and have a defined interphase, Fig. 7.1a shows several diffusive structures where the void fraction ranges from 0.25 to 0.75 but without the clear characteristic morphology of the resolved bubbles.

A quantitative analysis of the radial void fraction distribution by time-averaging (Fig. 7.2a) shows nearly the same profile for the dispersed gas with and without the swarm correction. In terms

of the continuous gas, on the other hand, an increase of the maximum value in the core of the pipe when avoiding the swarm factor correction for Gas3 can be observed. This gives a clear improvement in the prediction at the center of the pipe when compared to experimental data. Since the drag is no longer reduced for the continuous gas, the velocities are expected to drop compared to when using the swarm correction. This is observed in Fig. 7.2b, showing a better approximation for the centerline of the pipe to the averaged gas velocity from the experimental data. Furthermore, as some of the dispersed gas is entrained in the wake of the continuous bubbles, its velocity is also expected to be reduced at the core of the pipe, while maintaining similar values at the walls. This behavior is also observable in the quantitative data from Fig. 7.2b.

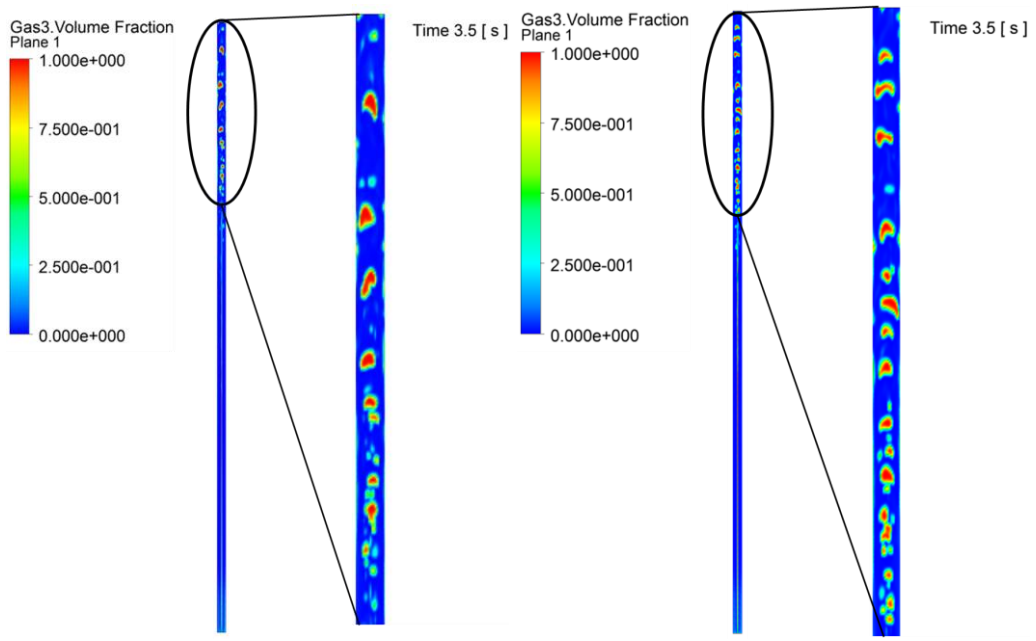

Fig. 7.1 Plane contour representation for the last quarter of the continuous gas for MT-Loop case experiment 118 A) with and B) without swam correction.

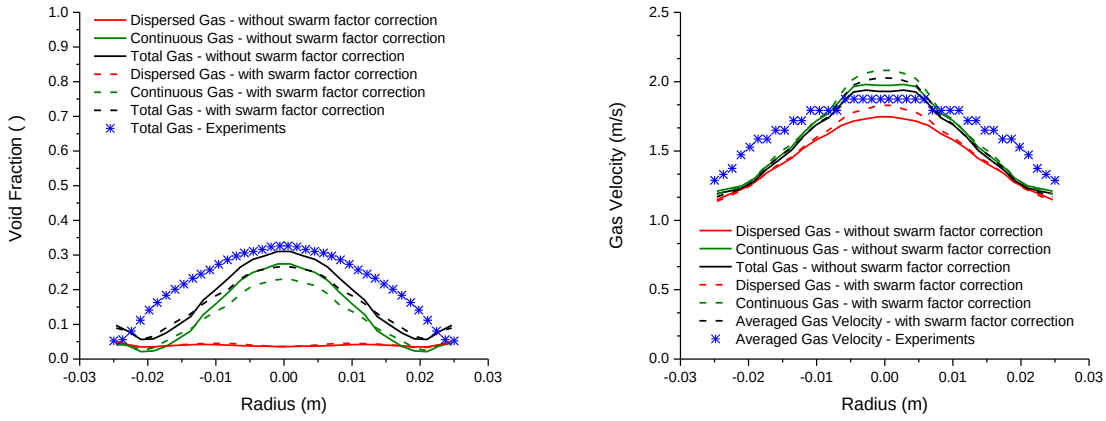

Fig. 7.2 Radial profile distribution of A) void fraction and B) gas velocity for MT-Loop calculation case 118 with and without swarm factor correction (L/D = 59.2).

The second, larger, problem regarding the interface transfer section of the GENTOP concept has to do with the definition of the limits which are given for the detection of the local gas morphology (φ_{morph}). An investigation which started when an unphysical behavior was observed for the lift force as originally defined within the concept, showed an important improvement on the overall behavior of the continuous gas when the limits where no longer dependable on the critical value of volume fraction ($\alpha_{cg,crit}$). The complete study can be found in Montoya et al. (2014b).

As it was stated in Chapter 6, the switch of morphologies was originally set to a critical void fraction value of 0.3 based on the knowledge that bubbly flows rarely exceed a void fraction between 0.25 and 0.35. While this may seem a good approximation, there is no need for such assumptions since there is a clear stablished limit based on the φ_{fs} function. It is known from its definition, where the free surface exactly starts and the dispersed gas ends. Furthermore, these discrepancies between the different formulations within the concept could introduce important deviations in the simulation by defining the interfacial area density and drag coefficient formulations for the free surface within the dispersed-bubbly region and vice-versa. Such discrepancy in the formulations can be easily observed with a simple single rising bubble (Fig. 7.3), where the region calculated by the interface detection algorithm (φ_{fs}), it is clearly not necessarily in the same range of $\alpha_{cg,crit} = 0.3$.

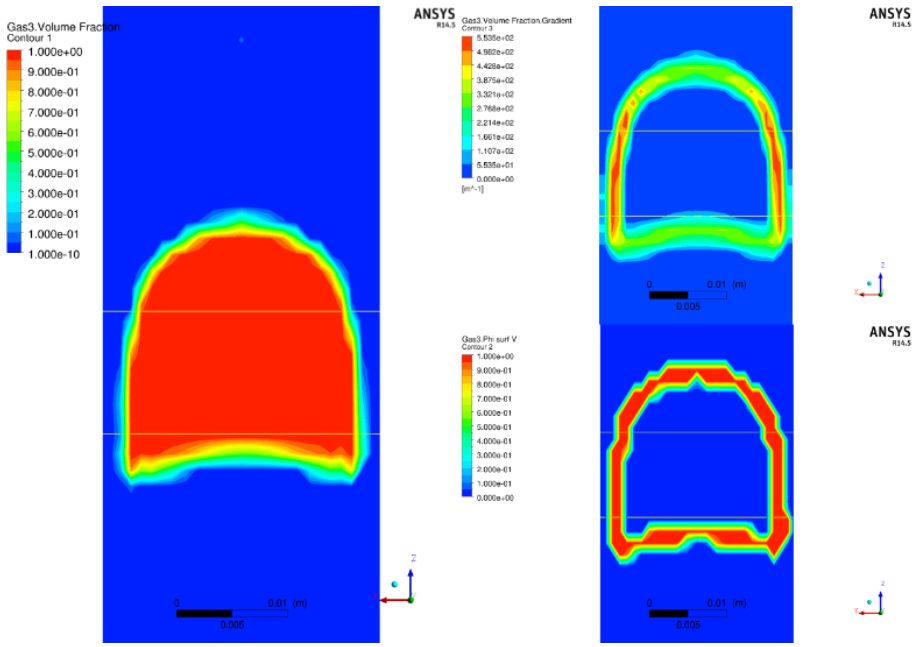

Fig. 7.3 Single rising bubble (D_P = 25 mm) represented by void fraction, gradient of volume fraction and detected interface.

The morphology switch criterion φ_{morph} has been reformulated in a more general manner as in Eq. 7.1. This correlation now maintains the dependency on the interface blending function φ_{fs}. The variable α_{cg} is only used to ensure that φ_{morph} remains within the free surface region after reaching

$\varphi_{fs} = 1$ and the gradient of volume fraction starts decreasing when moving towards the droplet region.

$$\varphi_{morph} \begin{cases} 0 & if \quad \varphi_{fs} < 0.5 \\ 0.5 * \left(\tanh\left(-5 * \left(0.5 - \varphi_{fs}\right)\right) + 0.5\right) & if \quad 0.5 \leq \varphi_{fs} < 1.0 \\ 1 & if \quad \varphi_{fs} = 1.0 \text{ or } \alpha_{cg} > 0.5 \end{cases} \tag{7.1}$$

7.1.3 Clustering force

Equally important, the clustering algorithm has been reformulated in a similar manner in order to have the affected region consistent with the critical gradient of volume fraction of the gas, and for that matter, with the φ_{fs} formulation. Before, it was simply blended in at $\alpha_{cg} = 0.2$ and blended out at $\alpha_{cg} = 0.8$. As it can be observed from Eq. 7.2, the force now acts outside the interface region, agglomerating the gas, and starts blending out as soon as the critical gradient of volume fraction has been reached, quickly disappearing as soon as a fully formed interface occurs ($\varphi_{fs} = 1$). The blending out is done very fast in order to reduce the dependency of the concept on this artificial algorithm. The formulation also takes into account that the force is not reactivated within the continuous structure (Fig. 7.4).

$$\varphi_{clust} \begin{cases} 1 & if \quad \varphi_{fs} < 0.5 \\ 0.5 * \left(\tanh\left(10 * \left(0.6 - \varphi_{fs}\right)\right) + 0.5\right) & if \quad 1.0 \leq \varphi_{fs} < 0.5 \\ 0 & if \quad \varphi_{fs} = 1.0 \text{ or } \alpha_{cg} > 0.5 \end{cases} \tag{7.2}$$

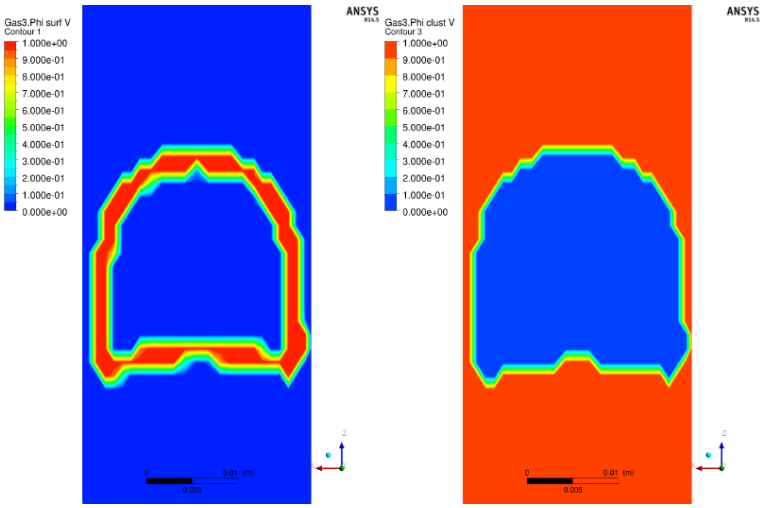

Fig. 7.4 Contour representation of A) interface detecting function φ_{fs}, and B) new clustering force limits φ_{clust} of a single rising bubble (D_P = 25 mm).

7.2 Determination of the bubble size distribution for the continuous gaseous phase

In order to analyze the full bubble size distribution in GENTOP, a software had to be created for extracting the data regarding the information of the continuous gas as a post processing step. The algorithm requires a point cloud with equal distant points containing the coordinates, the void fraction and optionally the free surface function (φ_{fs}) for the detection of the interface. The point cloud must be created in CFX and extracted as a text file, which is then read by the algorithm (Fig. 7.5). These points are then indexed by a hash table, and sorted using an associative function based on the second vector norm as shown in Eq. 7.3.

$$f_{hash}(Point) = \sqrt{Point_x{}^2 + Point_y{}^2 + Point_z{}^2} \tag{7.3}$$

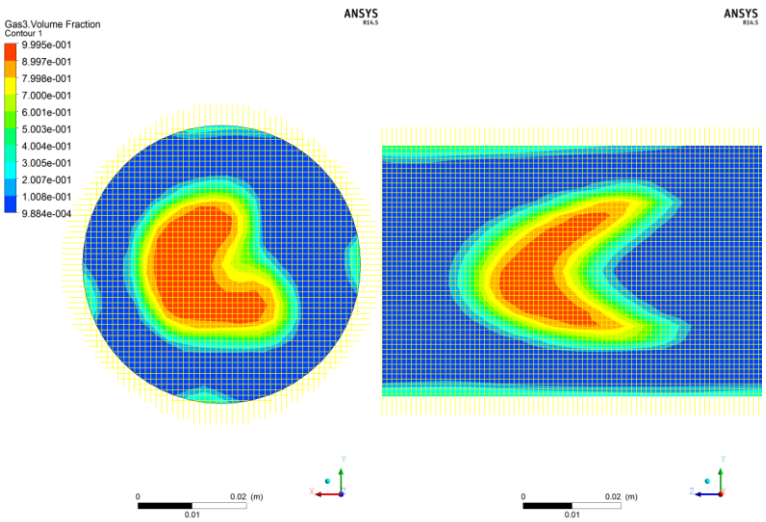

Fig. 7.5 Exemplification of the equally distributed point cloud in the axial and radial direction over the domain corresponding to a specific measurement level.

The separation between the points is then defined. Since all the points should have the same distance, the separation between them is assumed to be the shortest distance between two neighboring points. This point is then searched by getting the first value from the sorted hash table, called the seed point. The vicinity of the seed point is defined by the distance between the seed point and an arbitrary point with the same hash value. All the points in this vicinity are included in a new hash table with the hash function as shown in Eq. 7.4, where SP represents the seed point. The smallest hash value is defined as the cell size distance.

$$f_{hash,SP}(Point) = \sqrt{(Point_x - SP_x)^2 + (Point_y - SP_y)^2 + (Point_z - SP_z)^2} \tag{7.4}$$

The next step is the definition of the continuous phase. This can be done by using the φ_{fs} function, or a void fraction threshold. If the φ_{fs} function is used, then the user must define a value for α_{cg} and φ_{fs} where absolutely no bubble could exist. The standard values which were defined in the program were $\alpha_{cg} = 0.01$ and $\varphi_{fs} = 0.01$. Then, the first point in the hash table which has smaller values than the pre-defined one is chosen as the seed point for the vicinity. From that seed point, a region growing algorithm is started. This algorithm grows in certain directions until the threshold for φ_{fs} is reached. The growing is controlled by the user through the definition of the vicinity, where the search algorithm would be searching for points and the count of maximum neighbors the algorithm is taken into account. The region growing is done by a recursive algorithm based on the hash table.

When defining the continuous phase without using φ_{fs}, the user must define a void fraction threshold. All points which are above this threshold are defined as gas points inside a bubble or a surface point of the bubble. Same as before, a region growing algorithm is started, but the seed point is defined now inside the bubble. Here, all points which are greater than the void fraction threshold and are connected to the seed point, are defined as part of one bubble.

Once the continuous phase has been defined, the next step is the removal of that phase from the point cloud. When the method with φ_{fs} is used, then the points which were found are removed from the hash table. When α_{cg} is used instead, then all points which were not found before, are removed from the hash table.

After that, the bubbles are segmented. Since no points of the continuous phase are inside the hash table, all other points belong to another bubble. The region growing algorithm described earlier, is started with an arbitrary point from the hash table as seed point. All points that are connected to this seed point, are defined as one bubble and are removed from the hash table. This procedure is repeated until no points are left in the table.

Finally, the data is written out. The outputs consist of the geometry volume, the alpha weighted volume, the geometry diameter, and the alpha weighted geometry diameter. The geometry volume is defined as the count of the points inside the bubble multiplied by the cube cell size defined in the beginning. The alpha weighted volume represents the arithmetic average of the volume fraction inside the bubble multiplied by the geometry volume. Afterwards, the sphere equivalent diameter is calculated and defined as the geometry diameter. Finally, the alpha weighted geometry diameter represents the calculation of the spherical equivalent diameter of the alpha weighted volume.

An example of the raw data obtained by the algorithm can be seen in Fig. 7.6. Here the bubble volume and number is compared qualitatively to the CFX observation of an iso surface of all continuous structures for L/D = 59.2 from the MT-Loop experiment 118. The raw data extracted from

the software is shown in the ParaView visualizer due to the difficulties of CFX Post to work with txt extensions.

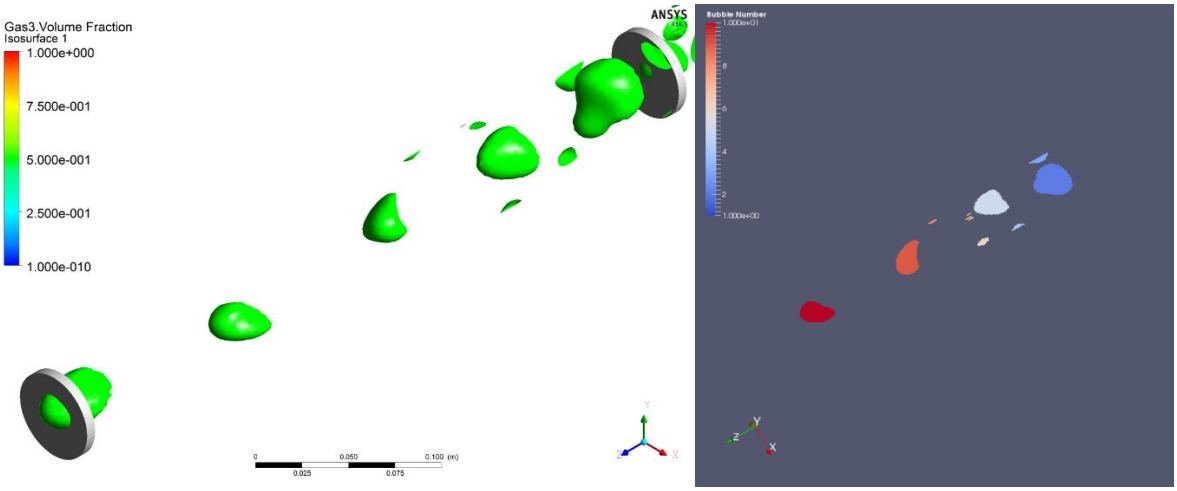

Fig. 7.6 Exemplification of a comparison of the gaseous continuous structures as A) an iso surface and B) the raw data from the bubble size distribution for the MT-Loop case 118 at L/D = 59.2 (t = 2.1s).

The alpha weighted geometry diameter is then used to calculate the equivalent spherical volume of the specific count contribution for each bubble size. Then, the volume fraction contribution to each of these bubble sizes is determined, and finally the bubble size distribution is calculated and presented in a logarithmic scale in order to better observe the contribution over the large range of bubble sizes. Such as with the velocity and void radial profiles, the GENTOP bubble size distribution is then averaged over a significant number of time steps in order to capture the transient behavior.

The bubble size distribution for the highest measurement plane can be observed in Fig. 7.7a. Contrary to the figures shown in previous chapters, the experimental data is not presented here as a scattered curve in order to better appreciate the higher bubble size peaks. These were irrelevant in previous calculations due to the inability of the polydispersed Eulerian-Eulerian and coalescence models to achieve such large bubble sizes.

An important point is that in these calculations, there is a certain amount of gas which is not being resolved but is still part of the potentially-continuous gas-field. When this void is not taken into account, there is a clear strong decrease of the bubble size distribution after the last iMUSIG group has been reached (red curve). That amount of void which does not belong to the continuous or the iMUSIG dispersed phase must be allocated somewhere. Since this work has shown that churn-like bubbles must be resolved after reaching the Ishii-Zuber maximum distorted bubble equivalent limit diameter (around 10.8 mm for normal atmospheric and temperature conditions), this value has been chosen as the limit from which bubbles can be resolved. For that matter, the quantity of void which does not belong to the iMUSIG nor the continuous gas field, has been allocated in a group which includes the bubble sizes from the last iMUSIG group to the Ishii-Zuber maximum distorted

equivalent limit bubble diameter (blue continuous curve). After the allocation of void, the first half of the curve largely resembles the one presented in Chapter 5, where bubbles where treated only as polydispersed gas (blue segmented curve). After that point, the curve used to flat out almost completely, and were unable to obtain any accurate information on sizes larger than 20 mm. It can be observed from Fig. 7.7a that this is not the case anymore. It is clearly shown how some characteristic peaks and trends from 20 to 35 mm are currently represented with a slight over prediction of only 0.25 %/mm. When moving to the next lower measurement plane (Fig. 7.7b), there is again a similar behavior for lower than 10.8 mm sizes as observed when using only the polydispersed gas. For higher sizes, there is a very accurate prediction of peak values and trends from 15 to 28 mm, followed by a clear under prediction of larger sizes. Since the void fraction radial distribution for this measurement level was still unable to represent the correct void gradients from the experiments, showing a lower gas core at the center and an overprediction of void at the sides of the pipe, the underprediction on larger bubble sizes was expected.

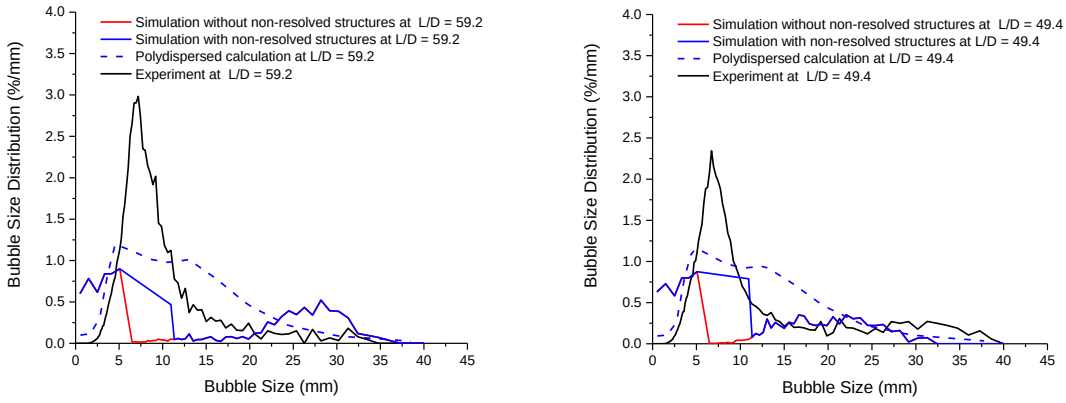

Fig. 7.7 Validation of bubble size distribution against the experiment 118 using the GENTOP concept for A) L/D = 59.2, and B) L/D = 49.4.

As we move towards lower positions in the pipe (Fig. 7.8a), the GENTOP phase is under the "transitional" zone which is mainly dominated by a striping behavior of the volume fraction of the gas. This cheated the bubble size distribution algorithm to believe that there were bubbles with larger sizes which are only large stripe-like structures which cover a large area of the axial direction. Moving to further lower positions (Fig.7.8b and 7.9a), these deviations and over predictions for larger sizes due to the striping worsen. Finally, close to the boundary condition (Fig. 7.9b), this deviation seems to attenuate since the stripes in the analyzed area are significantly thinner in comparison to the upper measurement levels. This is due to the specific profile given at the boundary condition which are a consequence of the thin needles at the injection site.

The technique developed and shown in this section gives a proper manner to obtain a complete bubble size distribution of the full GENTOP concept (iMUSIG and resolved structures). It is clear

that GENTOP is able to capture some of the expected distribution trends for the largest structures (with certain non-trivial deviations), which was not possible with the polydispersed Eulerian-Eulerian approach. The largest deviation observed of the bubble size distribution here seems to depend more on the striping behavior, which in turn does not allow the gas phase to properly develop until the highest measurement plane at L/D = 59.2. Neither the bubble breakup nor coalescence modeling along with the polydispersed iMUSIG approach, nor the GENTOP concept seem to be able to correctly predict the size distribution for sizes between 5.8 to 10.8 mm.

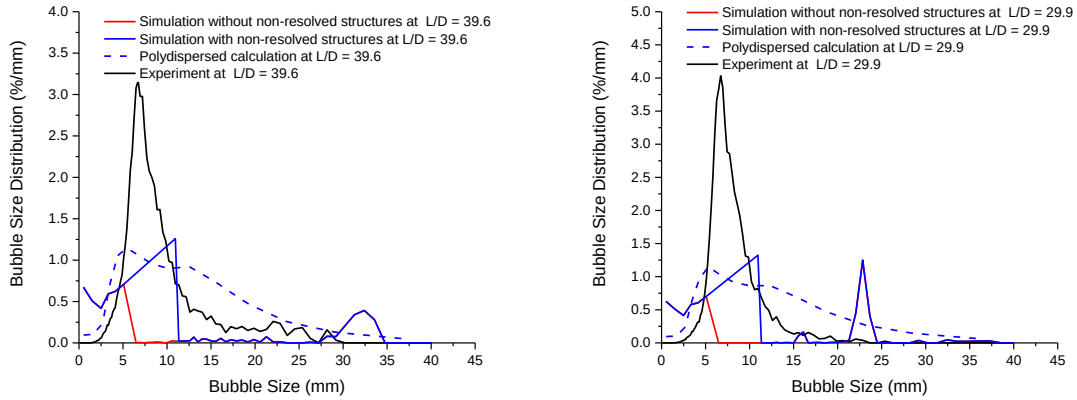

Fig. 7.8 Validation of bubble size distribution against experiment 118 using the GENTOP concept for A) L/D = 39.6, and B) L/D = 29.9.

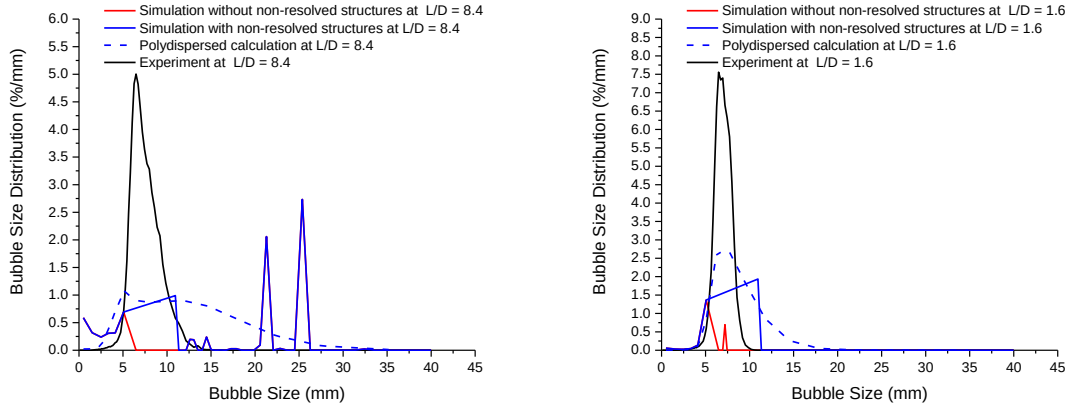

Fig. 7.9 Validation of bubble size distribution against experiment 118 using the GENTOP concept for A) L/D = 8.4, and B) L/D = 1.6.

7.3 Development and validation of a surface tension model for GENTOP

The results discussed in Chapter 6, clearly show an intrinsic limitation within the GENTOP concept which exists due to the lack of a surface tension model within the free surface. This produced an unphysical increase of void fraction near the wall of the pipe. It is expected that a larger deviation

could occur in other cases, such as with impinging jets, where the surface tension plays a dominant role in both circular and planar jumps (Liu et al., 1993). It is clear that the implementation of a proper surface tension model within the free surface region of the GENTOP concept is, at this point, absolutely essential. The objective of this section is to present the development and implementation of surface tension and wall adhesion models for the free surface region of the GENTOP concept. Furthermore, the model is validated against a large number of analytical and experimental cases on different flow scenarios.

7.3.1 Surface tension and wall adhesion for the GENTOP -concept

When the molecules of a certain fluid are on or near a liquid surface, they experience uneven molecular forces of attraction which cause the liquid surfaces to possess an elastic skin. This is known as surface tension, and since there are abrupt changes in the molecular forces when the fluid properties change discontinuously, it is considered an inherent characteristic of the material interfaces. This force wields itself on fluid elements at interfaces in both the normal and tangential directions. In general, the fluid interfacial motion induced by the surface tension force plays a fundamental role in both, natural and industrial phenomena. For example, capillarity, low-gravity fluid flows, hydrodynamic stability, surfactant behavior, cavitation, and droplet dynamics in clouds and in fuel sprays used in internal combustion engines (Levich, 1962; Osher and Sethian, 1988; Sussman et al., 1994; Williams et al., 1998; Francois et al., 2003; Berthelsen, 2002). A characterization of surface tension dominant flows can be done via the use of two dimensionless numbers: the capillary number (Eq. 7.5), and the Weber number (Eq. 7.6). A flow is considered surface tension dominant when Ca << 1 (for Re << 1), or We << 1 (for Re >>1).

$$Ca = \frac{\mu \mathbf{v}}{\sigma} \tag{7.5}$$

$$We = \frac{\rho \mathbf{v}^2 D_p}{\sigma} \tag{7.6}$$

Brackbill et al. (1992), proposed the Continuum Surface Force (CSF) method for modeling surface tension. While other methods exist such as the Continuum Surface Stress (CSS), the Ghost Fluid Method (GFM) and the Continuum Surface Tension (CST), for this study the CSF method has been chosen, especially due to the difficulties that other approaches have when modeling topologically complex interfaces.

For a curved interface, the surface tension as proposed by Brackbill can be separated into a normal and tangential component as shown in Eq. 7.7.

$$\boldsymbol{M^{ST}} = \boldsymbol{M^{ST}}_{\boldsymbol{n}} + \boldsymbol{M^{ST}}_{\boldsymbol{t}} \tag{7.7}$$

Where the normal component is given by Eq. 7.8.

$$\boldsymbol{M^{ST}}_{\boldsymbol{n}} = \sigma * \kappa_n \tag{7.8}$$

Here, σ represents the surface tension coefficient, and n is the unit vector to the free surface and directed from the main to the secondary fluid. The mean curvature of the free surface is given by *k*.

The tangential component (Eq. 7.9), also known as the Marangoni effect, acts exclusively when the surface tension varies along the surface, which is generally caused by changes in temperature. For a constant surface tension coefficient, the tangential component is zero, and the surface tension force works only normal to the interface.

$$\boldsymbol{M^{ST}}_{\boldsymbol{t}} = \frac{d\sigma}{dT} T = \nabla\sigma * |\nabla\alpha_i| \tag{7.9}$$

In the CSF model, a smooth field of the primary phase volume fraction is used to calculate a vector normal to the interface as shown in Eq. 7.10.

$$n = \nabla\alpha_i \tag{7.10}$$

Then, the curvature of the interface is calculated in terms of the divergence of the normal vector as in Eq. 7.11.

$$\kappa = -\nabla \cdot \left(\frac{\nabla\alpha_i}{|\nabla\alpha_i|}\right) \tag{7.11}$$

Finally, the normal component of the surface tension force is given by Eq. 7.12.

$$\boldsymbol{M^{ST}}_{\boldsymbol{n}} = -\sigma * \nabla \cdot \left(\frac{\nabla\alpha_i}{|\nabla\alpha_i|}\right) * \nabla\alpha_i \tag{7.12}$$

The wall adhesion on the other hand, describes the forces acting on the fluid interface along the line of contact with a solid wall. Very complex microscopic phenomena act in this region, resulting in an angle of equilibrium θ_w. This angle is a function of different surface free energies which are characteristic of the different interfaces such as γ_{SL} for the solid-liquid interface, γ_{LG} for the liquid-gas interface, and γ_{SG} for the solid-gas interface.

The contact angle, θ_w, characterizes the wetting of the wall by the fluid where wetting occurs for $\theta_w < 90°$, and non-wetting for $\theta_w > 90°$. For that matter, the contact angle is not an intrinsic property of the fluid, but depends of the contact system, and it can be measured only when the fluid is at rest (Fig, 7.10).

In order to account for the wall adhesion, a modification of the averaged normal vector at nodes in contact with the boundary is made. The normal vector, n, which is used in order to compute the surface tension forces, is modified at each node which belongs to the free surface contour as shown in Eq. 7.13.

$$\hat{n} = \hat{n}_w cos\theta_w + \hat{t}_w sin\theta_w \tag{7.13}$$

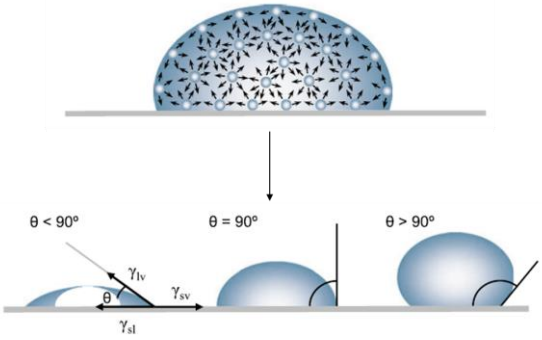

Figure 7.10 Illustration of the surface tension as a microscopic force, and the behavior of a drop for different Young contact angles [Yuan and Randall, 2013].

It is known (Bartosiewicz et al., 2008) that when the Brackbill model is implemented in the two-fluid Euler-Eulerian approach, the force must be divided between the two fluid phases occupying each cell. The reason for this is that both momentum equations are solved in the system (Eq. 7.14).

$$\boldsymbol{M_k}^{\boldsymbol{ST}} = \beta_k \boldsymbol{M^{ST}} \tag{7.14}$$

The pressure gradient in the two fluid model is calculated by the sum of the momentum equations. This gradient should be the same as the one in the single-fluid (homogeneous) model (Eq. 7.15). This means that the sum of both averaged factors (β_1,β_2) must be one.

$$(\boldsymbol{\alpha_1} + \boldsymbol{\alpha_2}) = (\beta_1 + \beta_2)\boldsymbol{M^{ST}} \tag{7.15}$$

Bartosiewicz et al. (2008) proposed two models for β_k, the first one based on mass average, and the second based on volume average in the cell. Strubelj et al. (2009) studied both models by analyzing the pressure jump over a droplet and concluded that the best results were given by the volume averaging model.

The model in GENTOP has been implemented in the CFX code as a general momentum source in a similar manner as with the clustering algorithm, where the separation between the two fluids is given by this volume averaging model, as proposed by Bartosiewicz and validated by Strublj.

7.3.2 Qualitative analysis of a cubic water droplet

This case refers to a very simple test based on a droplet of water with a pre-established cubic shape suspended in air. The walls of the domain need to be at least 2*D_T in order to avoid parasitic currents of air which could destabilize the interface of the drop (Canot and Caltagirone, 2004). This case would be used to compare the current implementation of the Brackbill CFS model in CFX v14.5 and my own implementation for the free surface of the GENTOP model. The first mesh used in this case, was a very coarse one with only around 104425 nodes as shown in Fig. 7.11. The water droplet was 5 mm in length with an equal nodalization of 0.5 mm. The surrounding air domain had a minimum

cell size of 0.5 mm, and a maximum closer to the walls of around 2.5 mm. The walls of the air domain were modeled as opening in order to avoid the restriction of flow at this boundary.

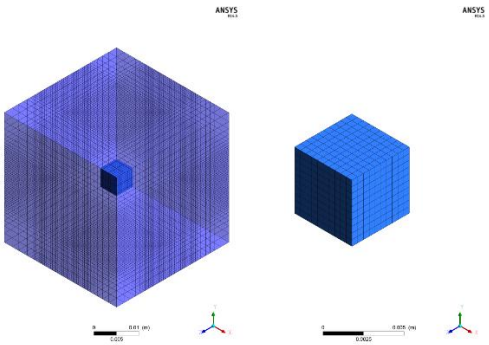

Figure 7.11 Nodalization of the drop of water (right side), and the surrounding.

The first two tests were made using the original CSF implementation of CFX. Both of them were made under the so-called "Free Surface" model, which utilizes the gradient of the void fraction to track the interface of the gas. This model highly differs from GENTOP since only continuous gas can be defined. The Free Surface option can be set based on homogenous velocity options (VOF), or inhomogeneous velocities (Euler-Euler with interface tracking and sharpening). In both cases, an interface compression level 2, also known as aggressive compression scheme, was chosen in order to avoid any possible diffusive effect at the interface. The initialization of the droplet was made in a way in which the interface is smeared in around three to four cells using a hyperbolic tangent function to allow a better behavior of the surface tension force due to a softer initial gradient distribution.

It can be observed from Fig. 7.12, how in the homogenous model, even when using the most "aggressive" available compression scheme, there is clearly a strong diffusion at the interface of the free surface for the VOF calculation. This issue significantly worsens when the inhomogeneous model is used, showing at exactly the same time step, how the diffusive effect in this case disturbs the interface in such way that there is a significant loss of mass.

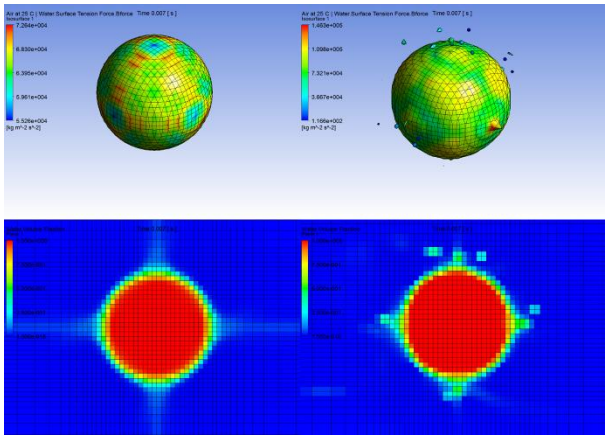

Figure 7.12 Cubic drop test case using A) the original CSF implementation from CFX with the Free Surface model at homogeneous velocities and using B) inhomogeneous velocities at t = 0.007 s.

The drop in the inhomogeneous case is not able to return later to the expected spherical shape. Furthermore, it is known that the drop is supposed to oscillate with certain periodicity, as it will be shown in a later test case. In the VOF test, the oscillation of the drop is rather fast before achieving the final spherical shape. This may seem as a positive aspect due to the fast stabilization of the drop, but it is not physical.

It can be observed from Fig. 7.13, how at the same time step as shown for the previous calculation, the drop is still oscillating when the implementation proposed here is used. Furthermore, the calculation shows that even at t = 0.022 s, while the oscillation magnitude seems to decrease, the drop is still not completely stable. This test case is shown for the inhomogeneous case, and no diffusion at all is observed at the interface. It is clear, that even if this implementation is not included in the discretization of the code, it seems to behave qualitatively better than the current original CFX implementation. Also in this case, the direction of the surface tension force has been illustrated.

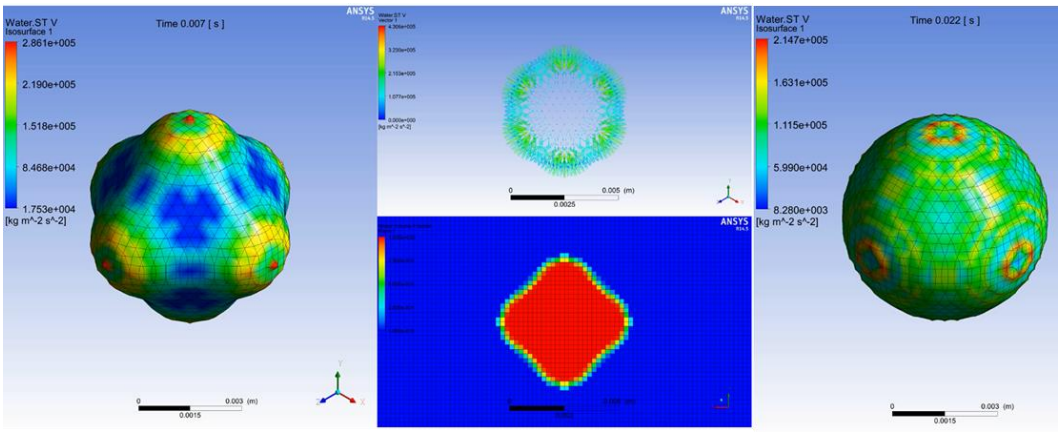

Figure 7.13 Cubic drop test case using the proposed CSF implementation for the GENTOP concept using the Free Surface model and inhomogeneous velocities at t = 0.007 s (right side) and t = 0.022 s.

In order to show independence from the code, the same model was also implemented in STAR-CCM+ v8.06, obtaining very similar qualitative results, as can be observed in Fig. 7.14.

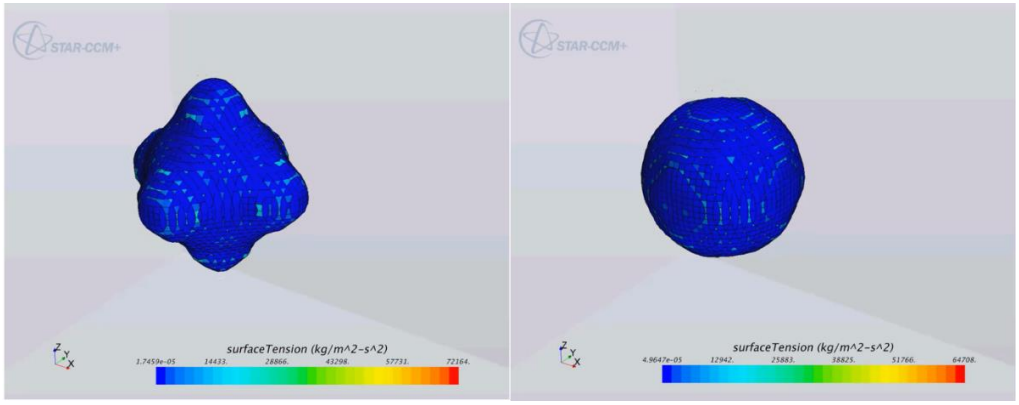

Figure 7.14 Cubic drop test case using the proposed CSF implementation for the GENTOP concept for the two-fluid approach at A) t = 0.007 s and B) t = 0.022 s in STAR-CCM+ v8.06.

In principle, this case should represent more of a challenge, since no interface compression nor tracking interface scheme is used, but instead, only a dispersed Eulerian-Eulerian gas phase has been defined, were the integrity of the drop is maintained exclusively by the implemented surface tension force.

7.3.3 Analytical study of spherical, cubic, and ellipsoidal ethanol droplets

Based on the work of Strubelj et al. (2009) and Canot and Caltagirone (2004), the first quantitative calculation cases are centered on analytical studies of oscillating droplets. Instead of the two-dimensional calculations as presented by both Strublj and Canot, three dimensional ethanol square (l = 40 mm), spherical, or ellipsoidal droplets ($r_{averaged}$ = 22.56 mm) are initially centered in a square cavity of L = 75 mm surrounded by air, where a zero-gravity field is imposed. The flow is isothermal, and there is no change on the surface tension coefficient. The fluid properties are $\rho_l = 787.88\ kg/m^3$, $\mu_l = 2.4x10^{-2}\ Pa\ s$ for the ethanol, and $\rho_g = 1.1768\ kg/m^3$, $\mu_g = 2x10^{-3}\ Pa\ s$ for the air. The objective behind increasing the viscosity values by a factor of 20 compared to the real viscosities, is to achieve higher damping of spurious velocities as well as a faster stabilization of the bubble shape oscillations. The surface tension between the ethanol and air is $\sigma = 0.02361$ N/m.

The oscillation period in the calculations of three-dimensional droplets with initially spherical (n = 2), ellipsoid (n = 2), and square shape (n = 4) is compared to the approximated analytical solution from Canot and Caltagirone (2004) given by Eq. 7.16 and Eq. 7.17.

$$\omega_0{}^2 = \frac{(n^3 - n)\sigma}{(\rho_l + \rho_g)R^3} \tag{7.16}$$

$$\tau_0 = \frac{2\pi}{\omega_0} \tag{7.17}$$

Where ω_0 is the oscillating frequency and τ_0 is the oscillating time period. The highest point in the Z direction or "north pole" has been tracked in order to determine the oscillating period.

The first calculation was based on the spherical initial shape (Fig. 7.15). For a relatively coarse mesh (32 x 32 cells within the droplet), the difference between the analytical and simulated solutions is only of 0.74 %, where the oscillating period of the calculation is 0.536 s, and in the analytical solution 0.540s (Fig. 7.16).

As expected, for the case in which an initial cubic shape is chosen, the oscillating period is dramatically smaller than in the ellipsoidal case, stabilizing almost completely after 2 seconds (Fig. 7.17). For a relatively coarse mesh (32 x 32 cells within the droplet), the difference between the analytical and simulated solutions is only of 1.68 %, where the oscillating period of the calculation is 0.526 s, and in the analytical solution 0.535 s (Fig. 7.18).

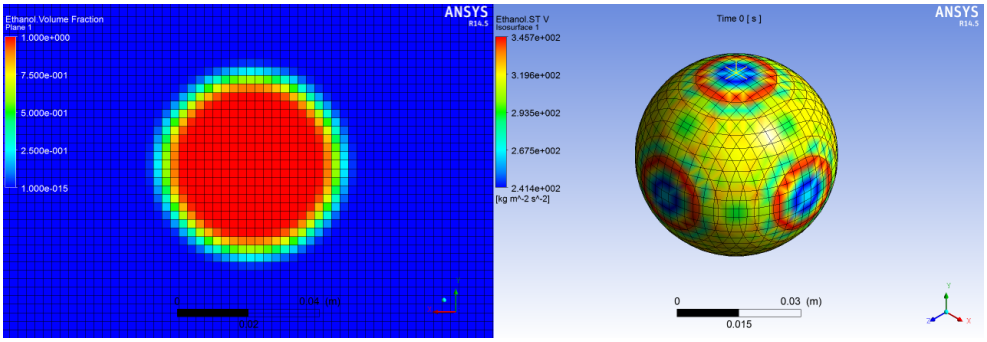

Figure 7.15 Coarse mesh for a spherical ethanol drop (32 x 32).

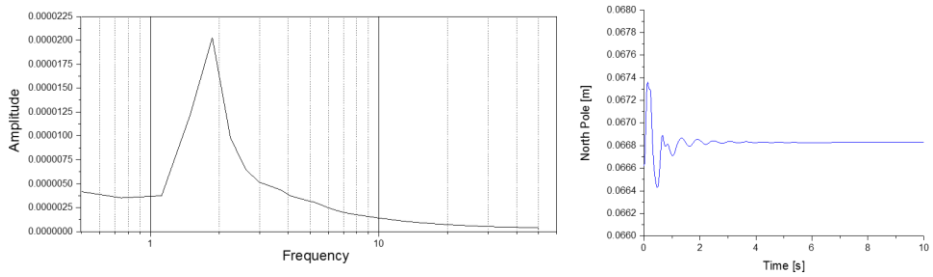

Figure 7.16 Oscillating frequency for an initially spherical ethanol droplet in air.

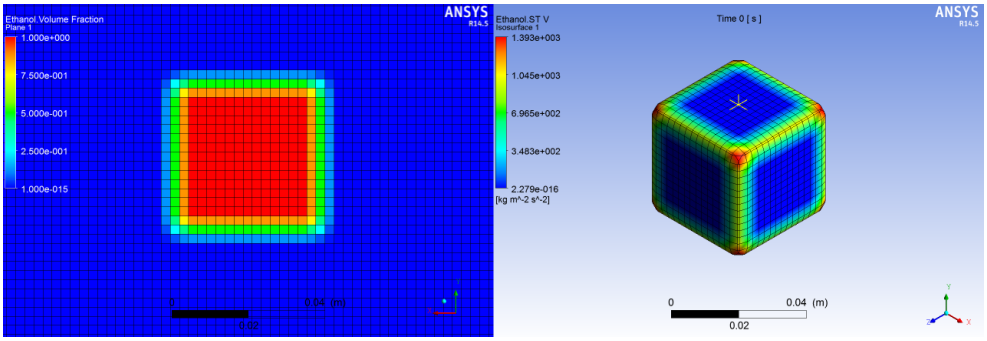

Figure 7.17 Coarse mesh for a cubic ethanol drop (32 x 32).

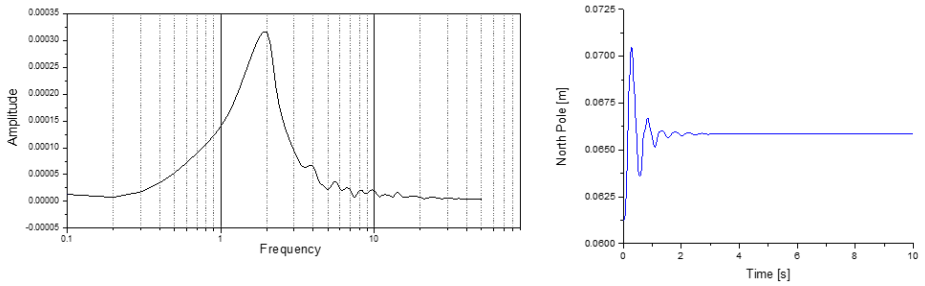

Figure 7.18 Oscillating frequency for an initially cubic ethanol droplet in air (coarse mesh).

In principle, damping should be larger in a coarse grid due to the discretization error in the convective part which acts as a diffusive term (numerical viscosity) in the momentum equation. As it was observed by Strublj et al. (2009) in their two-dimensional cases, also here we detected a slight

change with grid refinement which remains in the range of ±5 % (Strubelj et al., 2009). As it can be observed from refining the mesh (128 x 128) in the cubic case (Fig. 7.19), after 10 s of calculation the ethanol droplet is still oscillating. In this case, the oscillating period calculated from the simulation is around 0.536 s, which differs only in 0.19 % from the analytical solution (Fig. 7.20). This shows an improvement on the results of around 1.49 % by refining the mesh by a factor of 2.

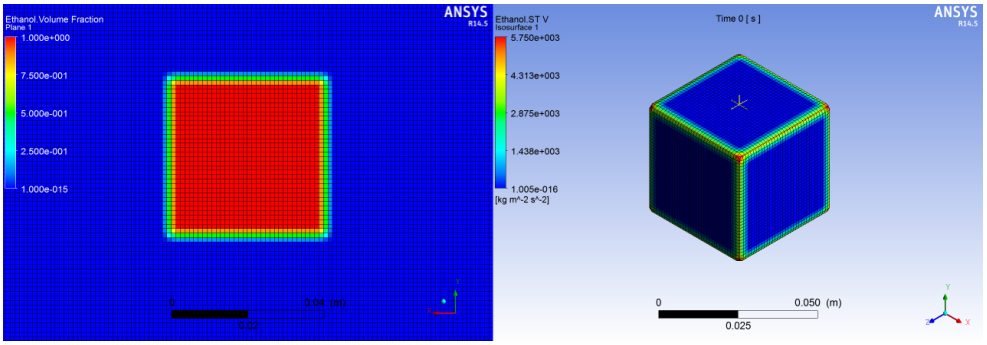

Figure 7.19 Fine mesh for cubic an ethanol drop (128 x 128).

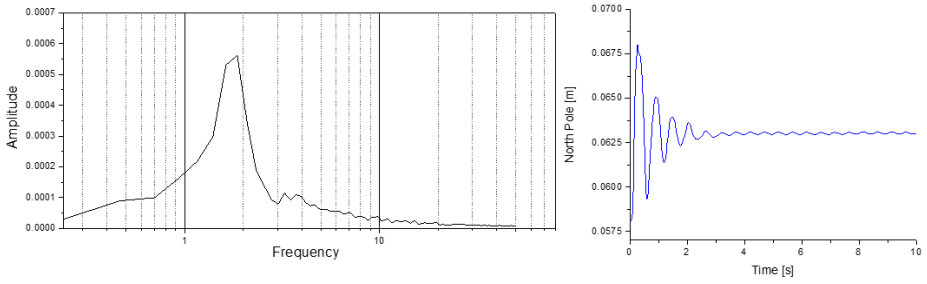

Figure 7.20 Oscillating frequency for an initially cubic ethanol droplet in air (fine mesh).

Such good results are more difficult to obtain with the ellipsoidal test case. When using the coarser mesh (Fig. 7.21), the oscillating period obtained from the calculation is 1.12 s while the analytical solution is around 1.55 s which gives a difference between the two results of 23 % (Fig. 7.22). Furthermore, it seems as if the droplet slightly shifted position in the axial direction, which could be occurring due to parasitic air velocities affecting the droplet interface.

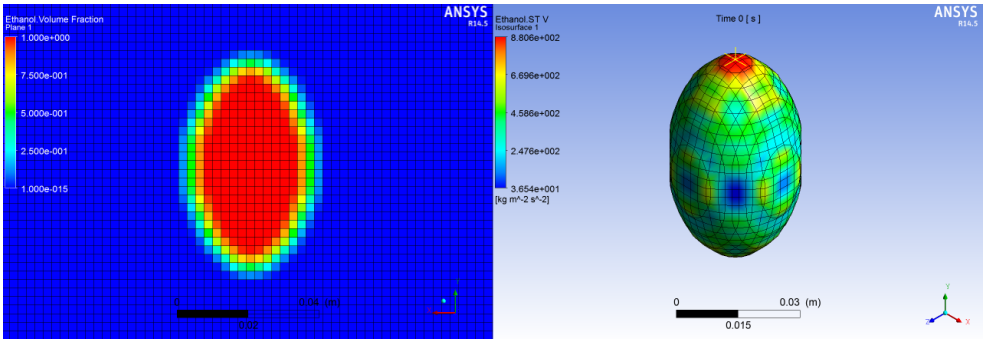

Figure 7.21 Coarse mesh for an ellipsoidal ethanol drop (32 x 32).

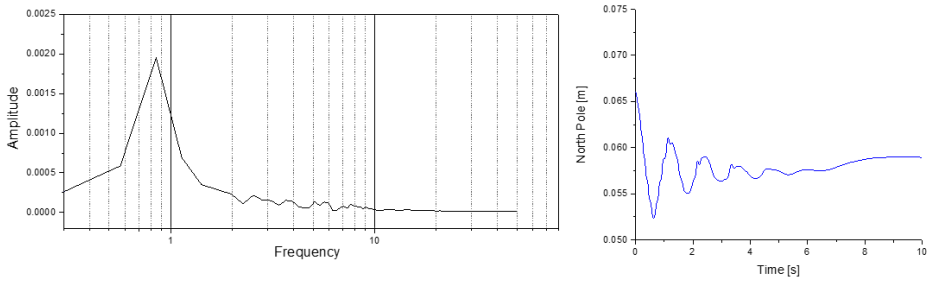

Figure 7.22 Oscillating frequency for an initially elliptical ethanol droplet in air (coarse mesh).

When the mesh is refined (128 x 128) in this case (Fig. 7.23), the droplet is no longer displaced. As with the refinement in the cubic case, the damping decreases obtaining a non-trivial oscillation even after 10 s of calculation. In this case, the oscillating period calculated from the simulation is around 1.25 s, which differs 19.3% from the analytical solution (Fig. 7.24). This shows an improvement on the results of around 4.8% by the refinement of the mesh, which agrees with the previously discussed observations from Strublj et al. (2009).

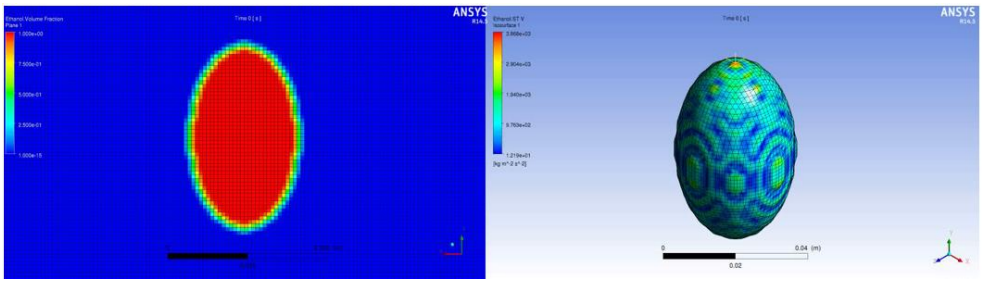

Figure 7.23 Coarse mesh for an ellipsoidal ethanol drop (128 x 128).

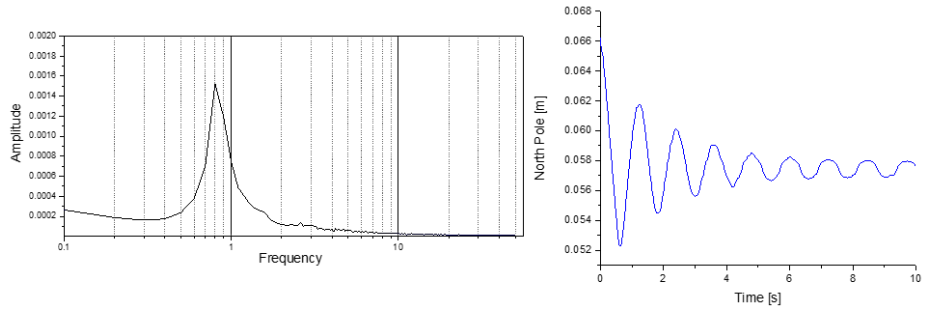

Figure 7.24 Oscillating frequency for an initially ellipsoidal ethanol droplet in air (fine mesh).

7.3.4 Rising bubble morphology and velocity validation

Tomiyama et al. (2001) studied the shapes and velocities of single bubbles rising through a vertical pipe under bubble column and pipe flow conditions. The experiments were made using air-water, and a pipe 24.8 mm in length. The ratio λ of equivalent bubble diameter (d_B) to the diameter of the tube (D_T) was varied from 0.2 to 2.0. In this dissertation, the test cases using $\lambda = 0.6$ for stagnant and pipe flow, and $\lambda = 1.0$ for bubble column conditions have be simulated and will be discussed

here. The reason to choose these ratios is due to the similarity of size and shapes the bubbles encounter in both churn and slug flow.

When bubbles have a ratio λ greater or equal than 0.6, they are usually classified as Taylor bubbles and their terminal velocity is no longer a function of λ, but of D_T. In these cases, the terminal velocity can be expressed as in Eq. 7.18, Eq. 7.19, and Eq. 7.20.

$$V_T = Fr\sqrt[3]{\frac{(\rho_l-\rho_g)gD_T}{\rho_l}} \tag{7.18}$$

$$Fr = 0.345\left[1 - exp\left(\frac{3.37-Eo_D}{10}\right)\right] \tag{7.19}$$

$$Eo_D = \frac{g(\rho_l-\rho_g){D_T}^2}{\sigma} \tag{7.20}$$

As for the velocity of a single rising bubble in pipe flow, the correlation suggested by Nicklin et al. (1962) and Collins et al. (1978) for a Taylor bubble is used, and can be expressed as in Eq. 7.21.

$$V_B = C\overline{V_l} + V_T \tag{7.21}$$

Where the constant C can be calculated for Re > 2300 as shown in Eq. 7.22.

$$C = 1.18 + 0.32exp[0.0017(2300 - Re)] \tag{7.22}$$

For the current cases, the terminal velocity for the stagnant fluid V_T should have a theoretical value of 0.216 m/s. The bubble velocity for the pipe flow case, V_B, was calculated as 1.396 m/s when the liquid velocity was defined as 1 m/s.

Finally, Tomiyama also proposed an analytical model to study the shape of the bubble (Fig. 7.25), and it is presented by Eq. 7.23 to Eq. 7.26, where R_{int} is the radius of the bubble interface, and Z is the distance from the nose of a bubble directed downward.

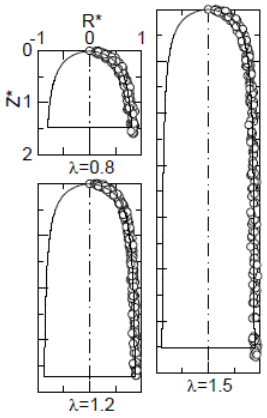

Figure 7.25 Comparison of measured (symbols) and calculated (curves) bubble shapes (Tomiyama et al., 2001).

$$R_1^* = 0.9 - \left[Z^{*0.7} + 0.9^{1/a}\right]^a \tag{7.23}$$

$$R_2^* = \frac{R_{int}}{R_T} \tag{7.24}$$

$$Z^* = \frac{Z}{R_T} \tag{7.25}$$

$$a = min(3.26x10^{-4}Re_l - 2.83,\ 2.29x10^{-5}Re_l - 2.36) \tag{7.26}$$

The first test was performed on a representative mesh, using 24 cells in the radial direction, and a time step of 10^{-4} s. Since stagnant flow was chosen, laminar flow conditions were assumed. A constant drag coefficient of 0.44 was set for this calculation. In order to separate the effects of all other forces in GENTOP, and study only the effect of the surface tension implementation, the inhomogeneous "free surface" model inherited from CFX with an aggressive interface compression scheme was used. For this first case, the surface tension has been deactivated. As the bubble rises in the channel, the shape and interface is highly disturbed, and the gas structure is in constant oscillation. This is consistent with the behavior observed in the GENTOP validation on the MT-Loop pipe flow cases. The terminal velocity was found to be 0.219 m/s, deviating from the theoretical solution by only 1.38 %. In terms of the morphology of the bubble, Fig. 7.26, it shows a very deformed structure which is certainly not expected for this case. A comparison using the Tomiyama analytical model in this case, would yield unphysical results.

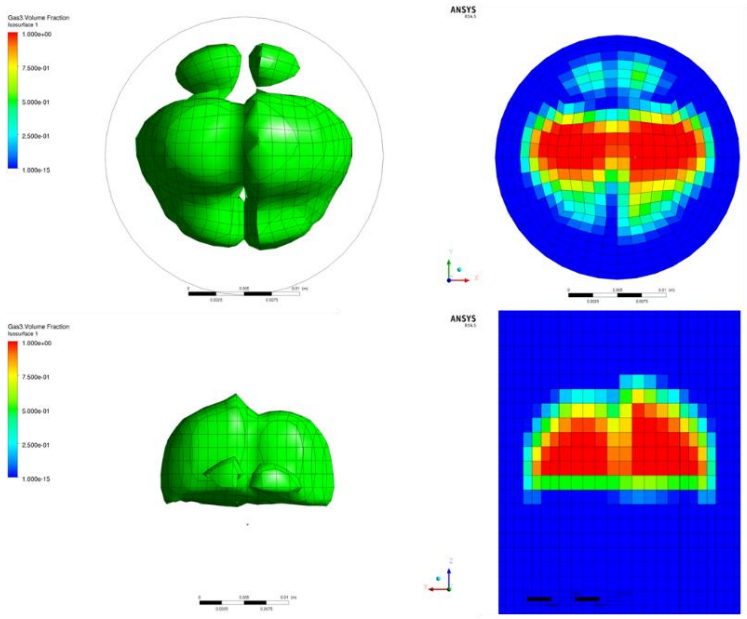

Figure 7.26 Morphology of a single rising bubble of λ = 0.6 without surface tension (V_L = 0.0 m/s).

When the newly implemented surface tension is activated, the shape of the bubble greatly improves, obtaining the expected cap-like gas structure. When the analytical Tomiyama model is used the error between the analytical and calculated results is only 0.41 % (Fig. 7.27). Here, the velocity hardly changes compared to the previous test, obtaining a value of 0.221 m/s.

This test case was then replicated using the full GENTOP concept. For this, two gas-fields were defined, where "Gas3" represents the potentially-continuous field, and "Gas2" represents the polydispersed structures. Seven iMUSIG size groups where used, and $D_{dg,max}$ was defined as 5.8 mm based on the sign change of the Tomiyama lift coefficient (Fig. 7.28).

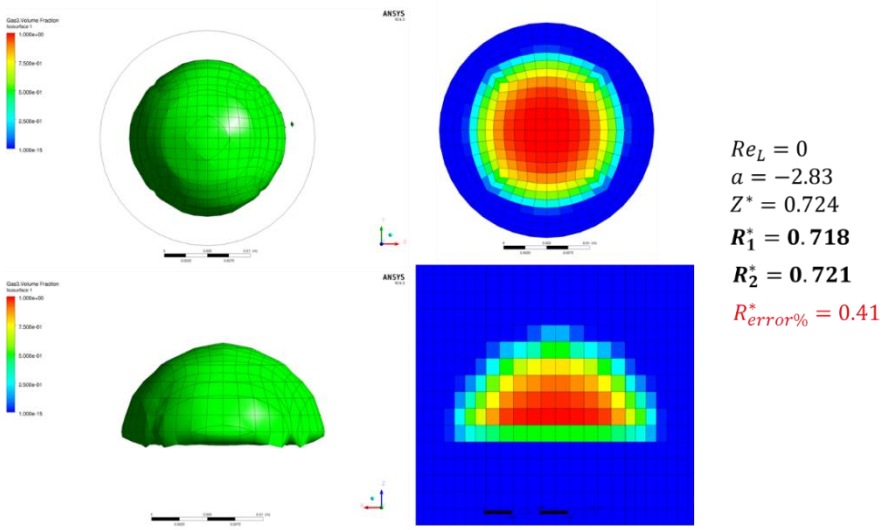

Figure 7.27 Morphology study of a single rising bubble of λ = 0.6 with the surface tension implementation (V_L = 0.0 m/s).

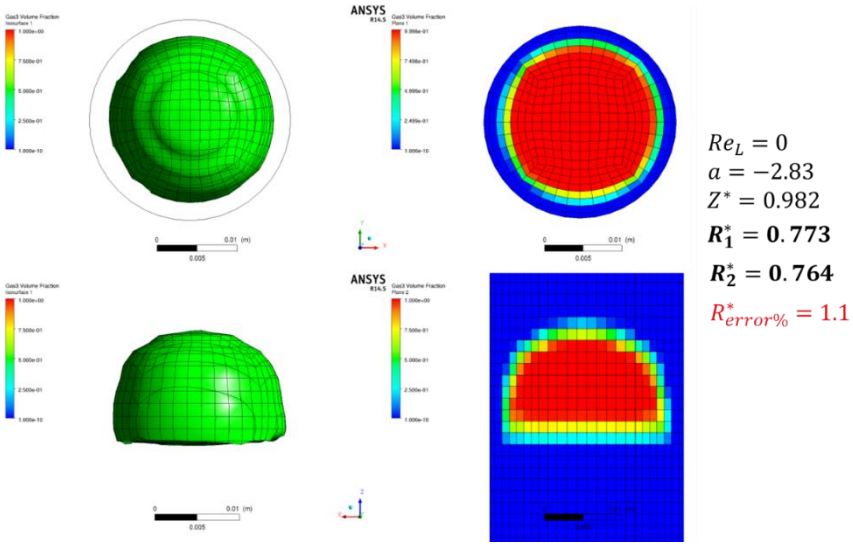

Figure 7.28 Morphology study of a single rising bubble of λ = 0.6 with the surface tension implementation using the full GENTOP concept (V_L = 0.0 m/s).

As it can be observed, the full GENTOP concept, including the surface tension, allows a much improved resolution of the continuous gas, and even without an interface compression scheme the surface tension force is strong enough to maintain the interface sharp. It can also be seen that, while there is some small shearing of the continuous gas, only a limited part is converted into dispersed ($\alpha_{Gas2} < 0.0022$), which is what would be expected in this test case. In terms of bubble morphology, there is only a small deviation from the analytical solution, 1.1 %.

In terms of velocities, contrary to the other two cases where a constant drag of 0.44 was defined, the AIAD drag coefficient for the free surface seems to highly underpredict the rising velocity of the calculation resulting in 0.135 m/s. This shows that a more classic coefficient of 0.44 for the free surface region on GENTOP instead of the full AIAD model could be sufficient for the proper prediction of velocity distribution for the resolved gas in vertical flow conditions.

When liquid velocity is included ($V_l = 1.0\ m/s$), the Re number increases to about 28,000. Here, the resolution of the bubble within the free surface seems to be reduced, and the difference between the analytical and calculated results for the morphology differs in about 13.7% at the end of the channel (Fig. 7.29). The inclusion of the liquid velocity shows an approximation to the analytical bubble velocity, as given by Eq. 7.21, of V_B equal to 1.30 m/s and a difference with the theoretical result of 6.8%.

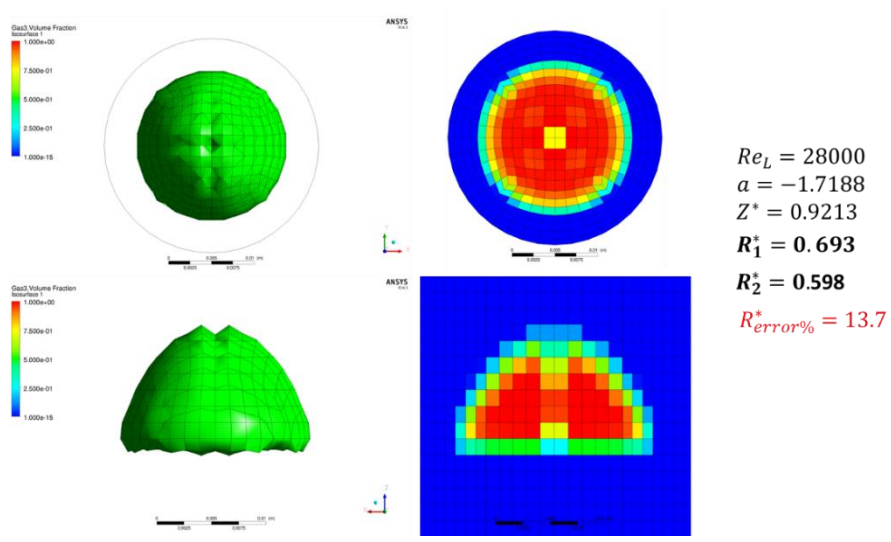

Figure 7.29 Morphology study of a single rising bubble of λ = 0.6 with the surface tension implementation (V_L = 1.0 m/s).

When using the full GENTOP approach in this case (Fig. 7.30), the bubble is again significantly more resolute, and the error between the morphology analytical solution from Tomiyama and the simulating result is only 6.1%. This shows a reduction of the morphology deviation of almost half in comparison with the non-GENTOP calculation. Furthermore, by adding the liquid velocity, the

resulting bubble velocity in the calculation (V_B) is equal to 1.27 m/s, underpredicting the theoretical value by only 9 % in this case.

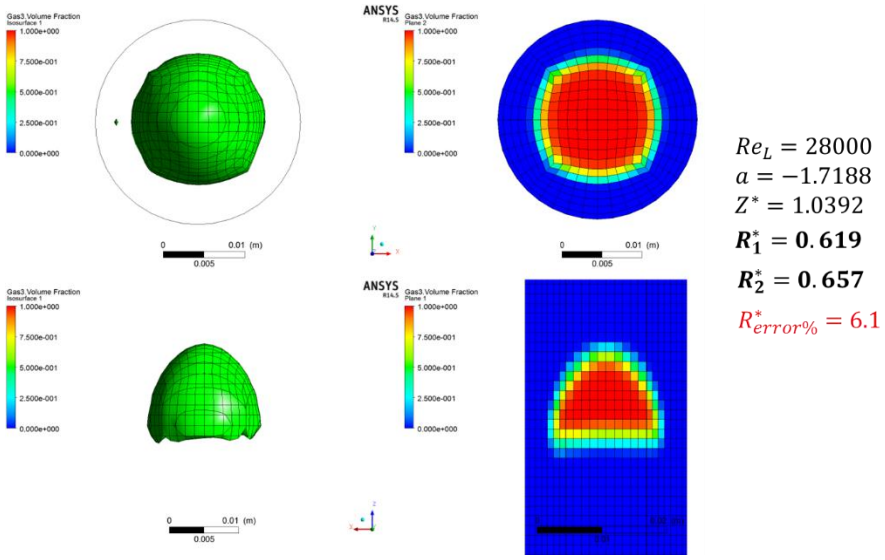

Figure 7.30 Morphology study of a single rising bubble of λ = 0.6 with the surface tension implementation using the full GENTOP concept (V_L = 1.0 m/s).

When the bubble grows to the same diameter as the pipe at λ = 1.0 (Fig. 7.31), its terminal velocity becomes slightly overpredicted in comparison to the smaller bubble case ($V_T = 0.234$ m/s) when the "Free Surface" model is used. Still, the difference with the theoretical value is only 8.3 %. In terms of the morphology of the bubble, the error against the analytical solution is still around 1 % (Fig. 7.32), but the resolution within the bubble in this case becomes excessively poor. Also, independently of the aggressive compression option scheme from the "free surface" model, there is still a strong diffusion at the interface.

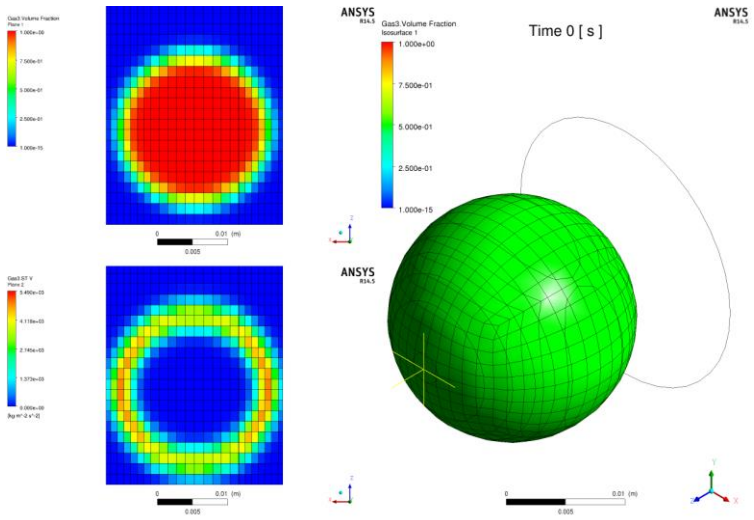

Figure 7.31 Initial state for a rising bubble in a vertical pipe with λ = 1.0 (V_L = 0.0 m/s).

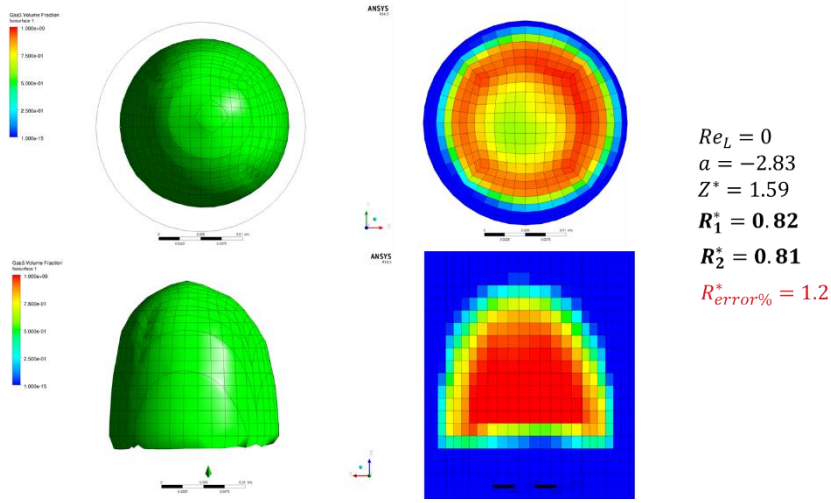

Figure 7.32 Morphology study of a single rising bubble of λ = 1.0 with the surface tension implementation (V_L = 0.0 m/s).

For the calculation using the full GENTOP concept, a terminal velocity of 0.136 m/s was found. While when using the "free surface" model, the velocities between different λ are only slightly separated (around 5.8%), the GENTOP cases go more accordingly with the experimental observations of Tomiyama. That is, after the bubble occupied 60 % of the pipe, its terminal velocity should not depend anymore of the diameter of the bubble.

In terms of the morphology of the resolved gaseous structure (Fig. 7.33), the error margin is maintained under the 2% range. This case also presents a maximum of dispersed gas void of a mere 3 % over the whole calculation, showing an even stronger integrity of the bubble compared to when modeling with λ = 0.6. Finally, the gaseous structure is clearly much better resolved in the GENTOP case, compared to the "free surface" modeling option once again. Also, the interface is significantly less diffuse, dispersing only between one to two cells.

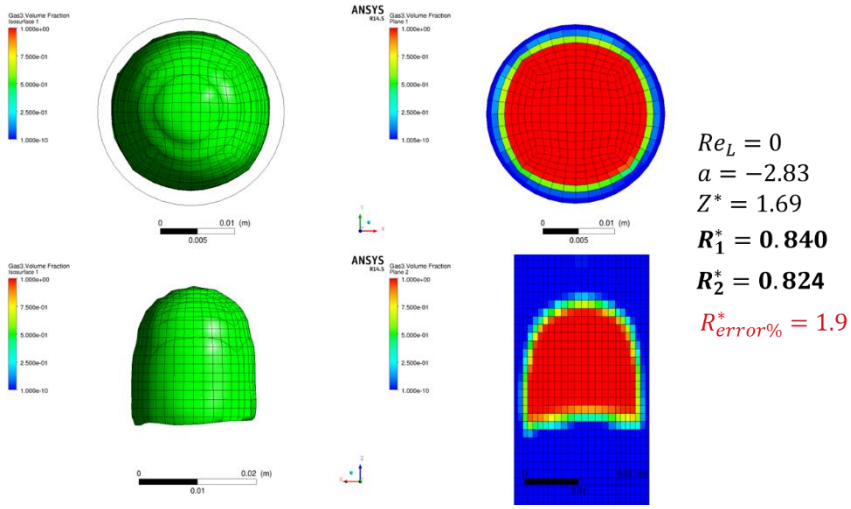

Figure 7.33 Morphology study of a single rising bubble of λ = 1.0 with the surface tension implementation using the full GENTOP concept (V_L = 0.0 m/s).

7.3.5 Wall adhesion validation

Three different cases were simulated in order to test the contact angle section of the surface tension implementation for the GENTOP concept. The three cases were based on a spherical drop of water residing on a wall-boundary surface (Fig.7.34). Gravity has been considered in this case, and depending on the pre-defined contact angle, the surface tension should be able to maintain the droplet standing with the proper inclination within the interface between the free surface and the wall. The complete domain, including the surroundings, in these cases counts with around 12 mm in length and a total of around three hundred thousand hexahedral cells. A refinement of the mesh by a factor of 1.5 was also prepared. In that case, the domain surrounding the droplet was also expanded. The diameter of the droplet was 4 mm in all cases.

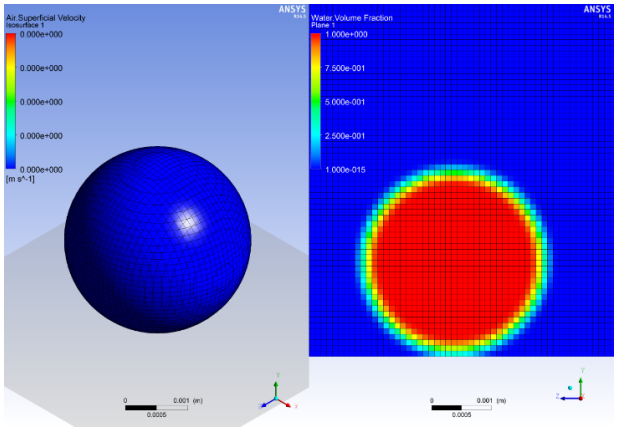

Figure 7.34 Initial state for calculations of contact angle for a residing bubble.

The first contact angle defined was 30 degrees, and while it is difficult to observe the result in an static image; the droplet starts opening while the vectors of the surface tension force push towards the outside of the free surface, until the residing angle of 30 degrees has been achieved. At this moment, the force changes direction and slightly modifies its magnitude in order to maintain the pre-defined contact angle (Fig. 7.35).

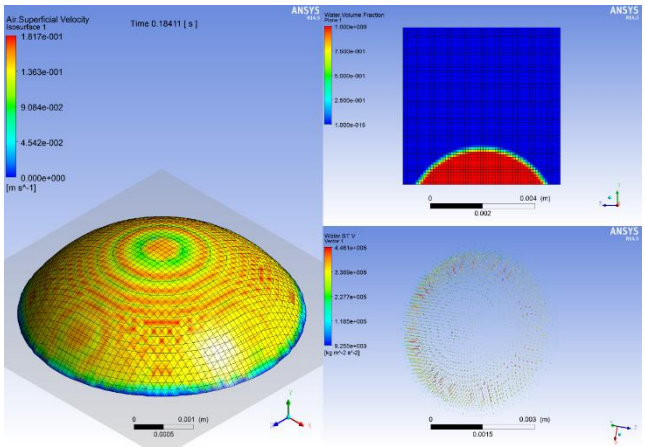

Figure 7.35 Final state of the calculation for a residing bubble with a contact angle of 30º.

In the second case, a residing angle of 90 degrees was established. In a similar manner as in the previous test, the contact angle was successfully achieved within the first 0.1 s and maintained during the rest of the 0.6 s of calculation (Fig.7.36).

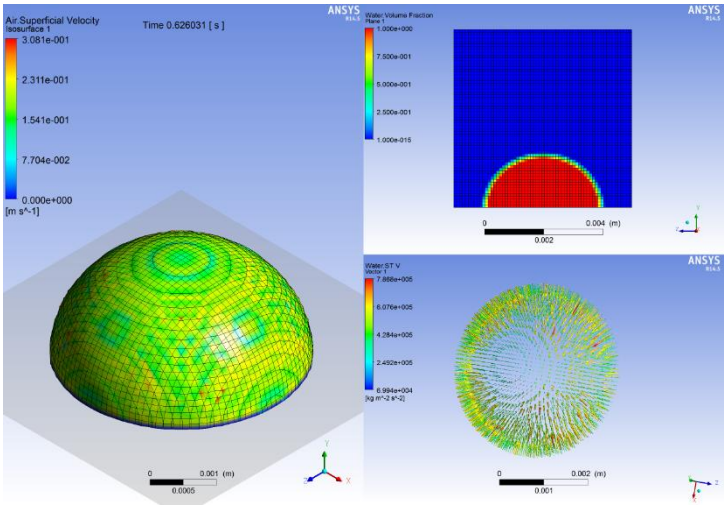

Figure 7.36 Final state of the calculation for a residing bubble with a contact angle of 90º.

Finally, an extreme non-physical case with a contact angle of 179 degrees was defined, obtaining a final residing angle of around 168 degrees (Fig. 7.37a). This last case was also studied using the refined mesh by a factor of 1.5. The refinement showed virtually no changes (Fig. 7.37b).

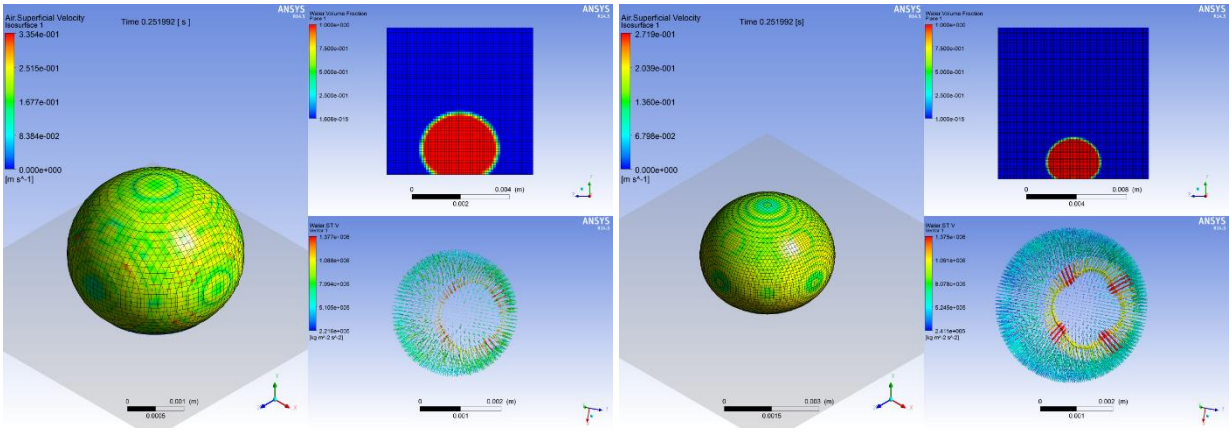

Figure 7.37 Final state of the calculation for a residing bubble with a contact angle of 179º A) without and B) with a grid refinement by a factor of 1.5.

7.3.6 MT-Loop case 118

After successfully testing the surface tension and contact angle effect by itself and within the latest state of the full GENTOP concept, the formulation can be finally applied to more complex high void fraction cases.

The first important improvement which the surface tension addition had in the MT-Loop case, refers to the formation of the bubbles shortly after the injection point. In Chapter 6, it was observed

that there was an inability to completely cluster the structures leading to a "transition zone", which was dominated by stripes of semi-continuous void for at least half the pipe. This effect can be seen from Fig. 7.38a, where at t = 3.74 s, the bubbles start being resolved only after more than half the pipe. This also means that there was nothing really physical to compare before the last two measurement levels. The addition of the surface tension force to the formulation clearly shows a dramatically strong reduction of the striping on the previously called "transition zone" (Fig. 7.38b). The striping now vanishes after less than a quarter of the pipe, and a clear formation of continuous gas can be observed almost immediately. This improvement is the result of a quick and more physical blend out of the cluster force, and the soft blend-in of the surface tension throughout the gradient of volume fraction.

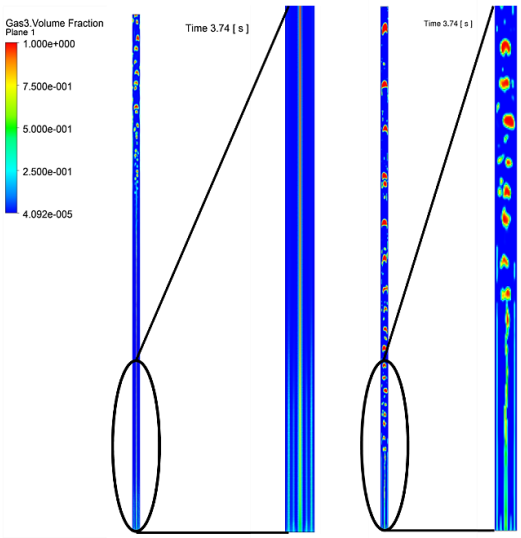

Figure 7.38 Plane contour representation of the continuous gas for MT-Loop case experiment 118 A) without and B) with the surface tension implementation.

Qualitatively, it can be observed from Fig. 7.39a, how the interface of the bubble used to vanish while the gaseous structure collides and moves along the wall. In the new model, the correct calculation of the curvature of the interface provides that the previous collisions no longer occur (Fig. 7.39b). Furthermore, as in the previously presented Tomiyama simulations, the continuous structures present a much better resolution when the surface tension model is activated. Also, like the cases presented in previous sections, the interface shows a dramatical reduction of the numerical diffusion in comparison with the previous model.

For the quantitative study of this test case, four measurement planes are being taken into account, separated by around 0.5 m each. The first measurement plane is within the first quarter of the pipe, where there is still a striping effect similar as in the model without surface tension (Fig. 7.40a). As it can be also seen from the qualitative images, the void fraction which composed these stripes is significantly lower, which is shown by a dropping on the spikes closer to the walls. Furthermore, the time averaging of the calculation when using the surface tension model, shows an almost perfect fit

for the centerline of the pipe in comparison to the experimental data. This last result comes as no surprise since, while for the calculation with surface tension a straight immovable line of void is observed, in the latest simulation there are vertical and horizontal gradients, which appear due to the effect of the tension force. This creates a plume-like behavior shortly after the gas injection. Shortly after the first quarter of the pipe (Fig. 7.40b) the void radial profile starts to disperse showing a more physical result comparable to the experimental data. The results of this measurement plane already show a large significant improvement over the calculations without the surface tension model.

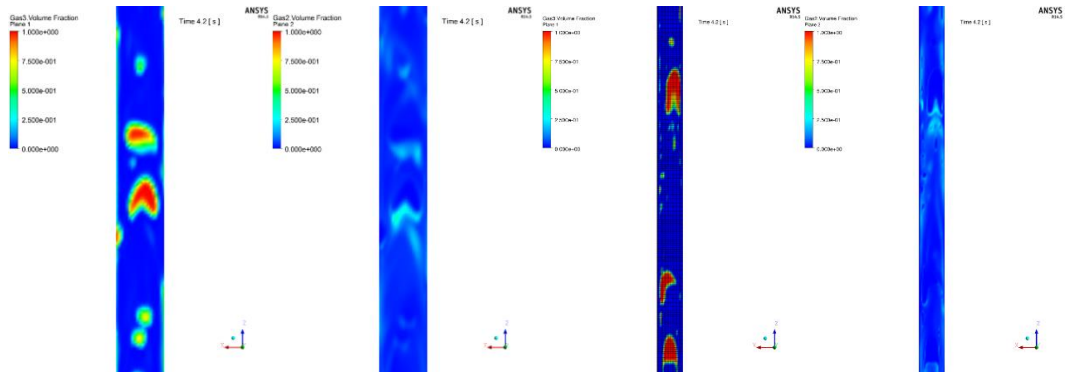

Figure 7.39 Plane contour representation of the continuous and dispersed gas for MT-Loop case experiment 118 A) without and B) with the surface tension implementation.

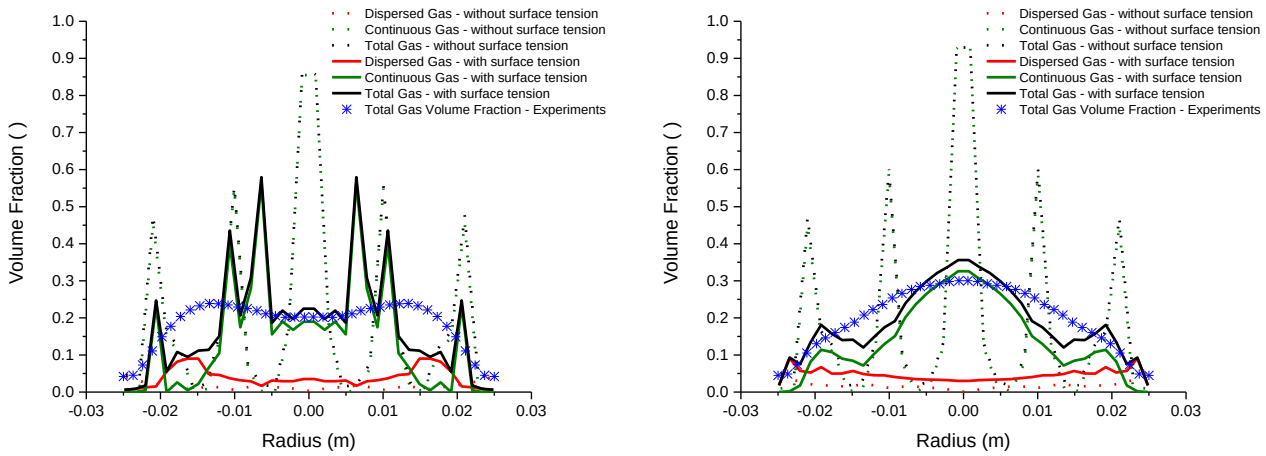

Figure 7.40 Void fraction radial distribution of MT-Loop calculation case 118 with and without surface tension for A) L/D = 8.4 and B) L/D = 16.2.

Already at exactly half of the pipe (Fig. 7.41a) an almost perfect profile with only a slight underprediction in the center line void can be observed. In the calculation without surface tension, at this point straight stripping can still be seen. For the final measurement plane at 3 m over the injection points (Fig. 7.41b) the void does disperse further, showing a flatter profile and a stronger underprediction in the center part of the pipe. As shown in Chapter 6, this is the only level where the calculation without surface tension could be compared to the experimental data. The slight apparent

loss of mass observable in Fig. 7.41a to 7.41b, is due to discretization deviations based on the fact that the GENTOP concept (specifically the mass transfer of the complete coalescence model) has been implemented via user functions and is not being discretized alongside the normal mass and momentum equations within the solver.

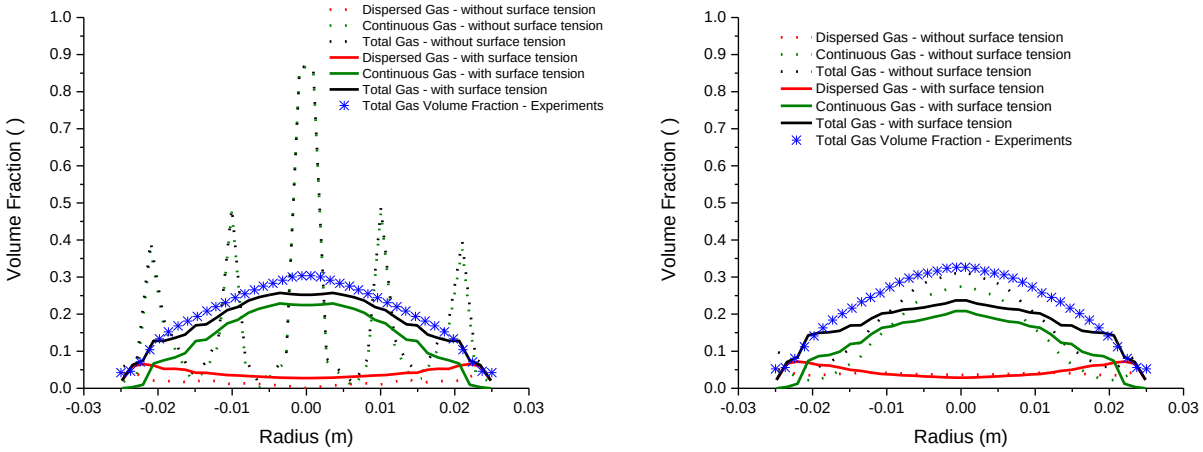

Figure 7.41 Void fraction radial distribution of MT-Loop calculation case 118 with and without surface tension for A) L/D = 29.9 and B) L/D = 59.2.

It is important to mention that in the plots with the inclusion of surface tension, the unphysical increase of void at the wall cells, clearly observable at L/D = 59.2, does no longer appear. In terms of radial velocity profiles, the trend, as before, is comparable to the void fraction distribution (Fig. 7.42 and Fig. 7.43). In these cases, an overprediction in the centerline of the pipe, and an underprediction when getting closer to the walls is observable. This deviation decreases when moving to higher measurement plane positions.

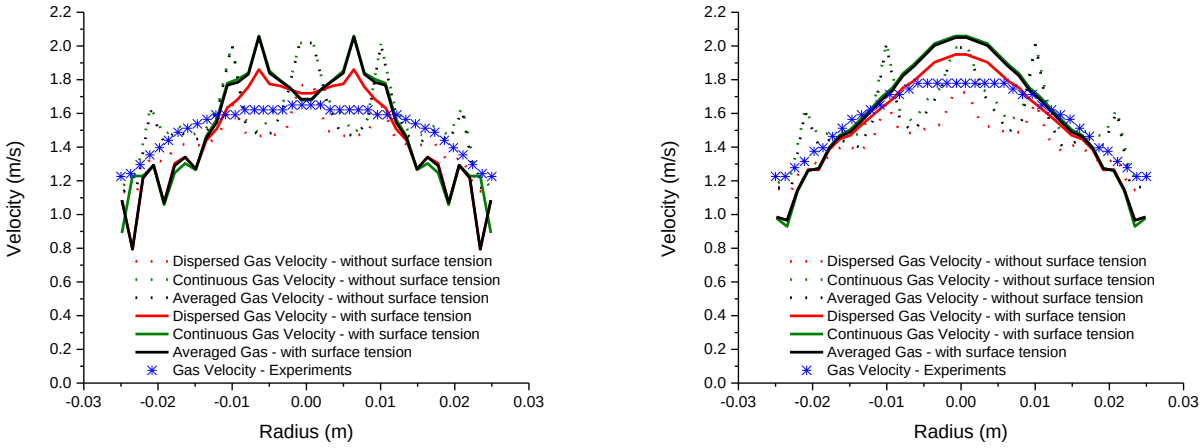

Figure 7.42 Velocity radial profiles of MT-Loop calculation case 118 with and without surface tension for A) L/D = 8.4 and B) L/D = 16.2.

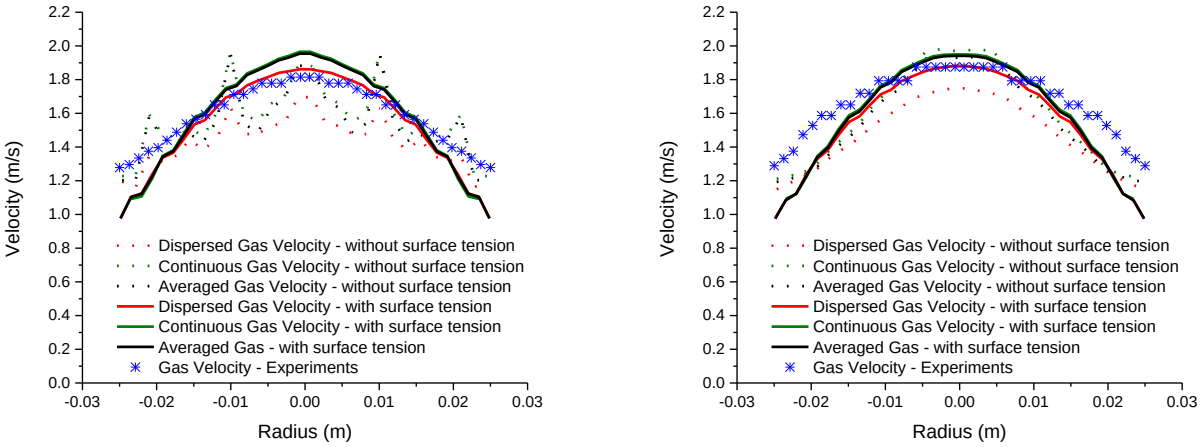

Figure 7.43 Velocity radial profiles of MT-Loop calculation case 118 with and without surface tension for A) L/D = 29.9 and B) L/D = 59.2.

In terms of bubble size distribution, close to the inlet (Fig. 7.44a), a large peak is observed between 33 and 38 mm. Since the void fraction profile is still in a striping-like zone, these results cannot be successfully compared to the experimental data. Moving upwards to the next measurement plane position (Fig. 7.44b), the largest over prediction can be observed for bubble sizes between 34 mm to 47 mm. The large peak from 17 mm to 20 mm seen in the calculation without surface tension, is no longer observable here.

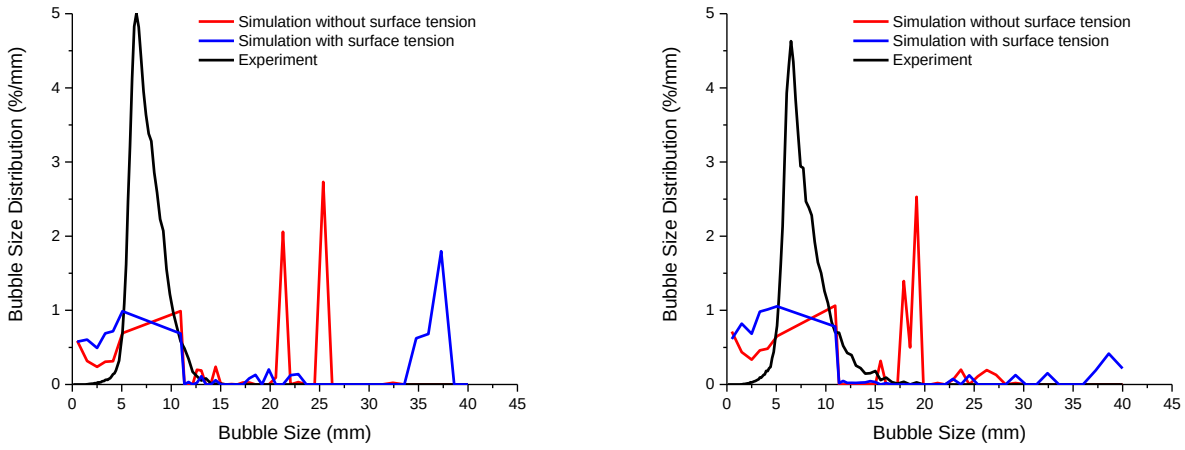

Figure 7.44 Bubble size distribution of MT-Loop calculation case 118 with and without surface tension for A) L/D = 8.4 and B) L/D = 16.2.

At mid pipe (Fig. 7.45a), the overprediction of larger bubble sizes increases when surface tension is activated, but the large peak observed for sizes between 20 mm and 25 mm for the case without surface tension, vanishes. For the highest measurement plane position (Fig. 7.45b), there is still an overprediction for sizes from 37 to 40 mm. The distribution between sizes 20 to 33 mm are now

comparable to the experimental data. Finally, the size distribution for sizes lower than 10.8 mm seem to be better predicted in the current case.

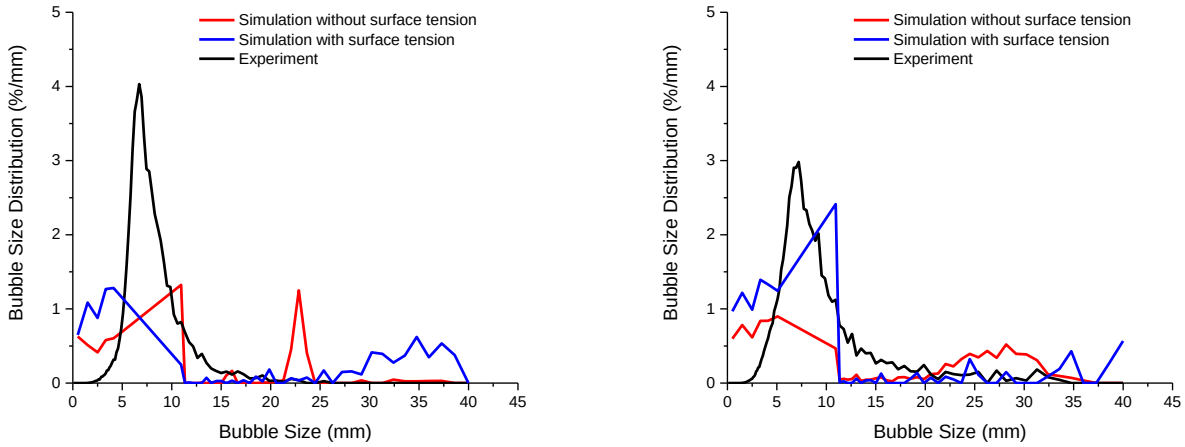

Figure 7.45 Bubble size distribution of MT-Loop calculation case 118 with and without surface tension for A) L/D = 29.9 and B) L/D = 59.2.

The increase in bubble sizes observed for the size distribution could perhaps be solved by resolving the largest eddies in the calculation, which are currently being filtered by the RANS approach. Using large eddy simulation (LES), for example, could introduce an extra shear term in order to provide the breakup of the continuous gas structures into smaller bubble sizes.

7.4 Chapter summary

This chapter dealt with the previously reported issues of modeling high gas volume fraction cases using the GENTOP concept. First, relatively simple solutions have been proposed and successfully implemented for lifting the limitations on the characteristic length of the cell and time discretization. In terms of interfacial transfers, the formulation has been modified to eliminate the swarm factor correction inside the drag coefficient as previously defined based on the AIAD concept. Also within the interfacial transfer, while the original formulation for the morphology transition adopted a critical value of the void fraction equal to 0.3, which represents the upper limit for bubbly flow conditions, this was eliminated, and a more general formulation was proposed for the morphology switch criterion, φ_{morph}. The original clustering method has also been modified. While the old formulation used a critical volume fraction value to activate the clustering force, this was found to be inconsistent with the rest of the concept, resulting for example in clustering effects within the free surface region and leading to destabilization of the interface. The improved implementation is applied consistently with the critical volume fraction gradient of the gas and with the φ_{fs} formulation. A technique has been developed in order to obtain the bubble size distribution for

calculation where the GENTOP concept is used, not only for the dispersed (iMUSIG) field, but also for the resolved structures. It was found that by modeling using the GENTOP approach, certain trends for large bubble sizes which were not possible to get using the full polydispersed approach, can now be captured with certain deviations from the original value. A full surface tension force, including contact angle, has also been introduced within the free surface formulation for the GENTOP concept. This formulation has been weighted against the originally implemented surface tension force in CFX, and has been successfully validated against a series of analytical models. These validation cases include oscillating ethanol droplets of different shape, single rising bubbles which occupy 60 % or more of the pipe, and droplets of water residing in a planar surface with different contact angles. When the model was used along the MT-Loop case 118, an almost complete reduction of the striping effect was obtained alongside with an improved resolution of the bubble, and a non-wetting behavior against the wall of the pipe. In terms of bubble size distribution, an overprediction of large bubble sizes clearly shows the need of an extra shear term which could be provided by considering the resolution of large eddies commonly filtered by the RANS approach.

8 Summary and Conclusions

The modeling of the churn-turbulent flow regime, along with its subsequent high void fraction transitions, presents a very difficult challenge which has remained unsolved for a long time. In the literature, it is clear that one of the main reasons for that is the consideration of idealistic conditions that are commonly assumed for this flow regime. A first step was taken in order to fully understand the known-physics behind the churn-regime and transitions from and to this flow pattern. It was noticed that there was a general contradiction and lack of understanding of the churn and slug-like bubbles, but it was clear that, despite many attempts from system codes, only CFD approaches have the possible conditions to simulate these types of space and time dependent, highly-turbulent flows.

Using as a well-known validated set of baseline models for bubbly flows, polydispersed Eulerian-Eulerian multi-fluid two gas-field approach calculations based on the TOPFLOW experimental facility were made. The experiments were under transitional flow from bubbly to churn, as well as churn-turbulent flow at different liquid velocities. The results show that the secondary gas field was behaving in an unphysical manner in positions closer to the inlet boundary, producing a very slow transition of void towards the center of the pipe, and a large peak for void fraction radial distribution which was not comparable to the experimental data.

Using the advantageous iMUSIG approach, a third group velocity field for the gas phase was set. Based on the literature, this group was separated using a distorted limit spherical bubble diameter proposed by Ishii and Zuber (1979). The separation into a new velocity field, without accounting for further physical modifications, showed a significant improvement by eliminating the unphysical peak which was previously observed. The new calculations, allowed to better separate the effect of the bubble closure laws for the churn-like bubbles, showing a too fast migration of these types of structures towards the center of the pipe. Based on previous experiences and literature, it was thought that the lift force contribution was working too strongly in comparison to the turbulent dispersion force. A nullification of the lift force showed hardly any change on the void radial distribution, only producing a 5% general lowering of the void profile. By studying the effect of the other closure relations on this third gas field, it was seen that the wall force was producing the previously observed unphysical effect on the very large deformable churn bubbles. A nullification of this force produced a rather flat profile of void distribution. By reactivating the lift force, a stronger effect was noticed in the calculations.

This lift force effect was further studied, by means of modifications on the lift coefficient for the third gas field. The lift force, based on the lift coefficient as proposed by Tomiyama for $Eo > 10$, was indeed acting too strongly in comparison to the turbulent dispersion force. While a case-dependent solution was proposed for these churn and slug cases, further improvement of the physics behind the

lift formulation for these types of gas structures is no longer possible with the use of the current modeling techniques. Indeed, there are no known experimental nor DNS data which could help provide information for a better formulation of the lift for churn and slug-like bubbles.

The use of the hybrid model known as GENTOP, still under development, was proposed. This allowed to fully-resolve the largest deformable gas structures, avoiding the use of idealistic conditions of the current closure laws for these bubbles, while modeling the small bubbles as dispersed gas. It also provided for mass transfer between both gas morphologies. The original model has been previously validated only against qualitative data, and some of the parameters were set based on those test cases. Calculation for both, churn-turbulent and slug flow regimes based on the TOPFLOW and MT-Loop facilities, allowed to study the limitations of the model by quantitative analysis of void fraction and velocity profiles. Some of the characteristic behavior of churn-turbulent and slug flows typical from the experimental data, was already captured by the first calculations, showing for example entrainment of dispersed gas in the wake of the large continuous bubbles. A critical striping-like behavior of void was observed for more than half of the pipe, rendering the results incomparable to experimental data until the last two measurement planes with the lower position being at L/D = 49.4 for the MT-Loop case. Another important effect was that of a void fraction increase at the wall of the pipe, which seems to come from the fact that the model does not account the surface tension within the free surface region. Minor changes were also made during these first calculations including improvements on the complete coalesce formulation and the addition of a no-slip boundary condition for the continuous phase.

Major improvements were later made to the concept. Simple but effective solutions were proposed to lift the limitation of the concept in both, the characteristic length of the cell, and the time averaged discretization. It is now possible to use the concept alongside complex meshes with non-homogenous cell sizes and adaptive time steps. The interfacial transfer model was also modified by improving the formulation which was used for the drag of the potentially-continuous gas, and by improving the formulation of the morphology criterion. This was done by allowing dependence only on the interface detecting algorithm, and thus eliminating assumptions for the pre-defined critical void fraction parameter. The clustering force was also modified into a more consistent algorithm which depends on the interface detection function, and reduced non-physically based assumptions.

A small software has been developed in order to further improve the quantitative analysis of the GENTOP calculations. The algorithm works as a post-processing step calculating the bubble number and sizes by using either a void fraction limit value or the interface detection function. It was found that the calculations using GENTOP were able to predict a similar trends with certain deviations as seen in the experimental data. While the GENTOP simulations showed a distribution dominated by a peak-like behavior for large bubble sizes, the simulations based on the polydispersed approach only showed a soft lowering planar-like trend instead.

Surface tension and wall adhesion models were finally introduced into the free surface region of the GENTOP concept. These models were first weighted against the original CFX implementation and then thoroughly validated against a series of analytical and empirical data. These test cases included comparisons with the analytically calculated period of oscillating ethanol droplets of different initial shapes, water droplets residing in a planar-like surface affected by gravity, and rising bubbles under pipe flow and bubble column conditions which initially occupy 60% and 100% of the pipe. In terms of the oscillating ethanol droplets, the deviation from the analytical solution was generally less than 2 % for all cases but the elliptical-initial shape, where the deviation increased to around 20%. A mesh refinement by a factor of 2 only improved the solution by less than 5%. The residing water droplet case allowed the successful validation of the contact angle formulation of the surface tension.

When the self-developed surface tension force was introduced on single rising bubbles using the inhomogeneous "Free Surface" model inherent from CFX and a constant drag coefficient of 0.44, the terminal and bubble velocities achieved values deviated from the theoretical solutions by less than 2% and 7%, respectively. The bubbles in these cases presented a very poor resolution and a large diffusive interface, even when using the aggressive inherent compression scheme from CFX. When repeating the same calculations using the full GENTOP concept, the resolution of the bubble largely increased, and the interface was shown to be very sharp in all cases, independently of the lack of an interface compression scheme. The terminal and bubble velocities were largely under predicted in these cases when using the full AIAD model for the free surface. This shows that perhaps a simpler coefficient of 0.44 could be enough to capture the correct velocity of the continuous gas. When comparing the morphology of the bubbles against analytical solutions, the deviation on the calculation for stagnant fluid was generally less than 2%. For the pipe flow conditions, the simulated and analytical solution deviated by 13.7 % for the "Free Surface" CFX approach, and dropped by almost half (6.1%) when the full GENTOP concept was used.

Finally, the surface tension modification on GENTOP was tested against the MT-Loop cases, showing a large improvement on almost all of the previously observed limitations. The most important of all was the extreme reduction of the striping-like behavior of previous calculations from the middle of the pipe to less than a quarter. This allowed to finally obtain results comparable to the experimental data as soon as L/D = 16.2. The void radial profile in all these cases actually showed an acceptable prediction, which almost perfectly matched the experimental data as soon as the middle the pipe was reached (L/D = 29.2). Similar to the previous observations in other test cases, the addition of the surface tension showed a large improvement on the resolution of the continuous large deformable bubbles, and a very refined interface. This showed that the sole addition of the surface tension model within the free surface region is enough to produce a very sharp interface, without the aid of any other sharpening algorithm. Also, the correct calculation on the curvature of the interface

in the continuous bubbles prevents them from blending and moving along the wall, reducing the unphysical void peak close to the wall boundary observed in previous calculations. In terms of bubble size distribution, while the large unphysical peaks were no longer observable compared to the previous calculations, there is now a considerable overprediction of the largest bubble sizes. Perhaps that over prediction can be resolved by solving the large eddies present in the liquid phase, which could introduce extra shear on the surface of the continuous bubbles, increasing their breakup into smaller sizes.

As a "side product" of this research, a calculation using the new modifications on the GENTOP implementation was performed for annular flows, and compared against the experimental data from the TOPFLOW facility experiment 184. The results showed an acceptable prediction of velocity profiles already at the middle of the pipe (L/D = 22.9). At that position, the gas core was underpredicted, while by L/D = 39.7, a void profile comparable to the experimental data was obtained. While these are not perfect results, it clearly shows the potential of the modified GENTOP model for simulating more complex high void fraction cases, including the possibility of full boiling phenomena cases including transitions, in the near future. This was not possible with the original version of the concept.

Based on the previous conclusions, the possible direction for further development should be focused on improving the models for turbulence for the hybrid GENTOP approach, and to test the current state of the concept for much more complex cases, including calculations where full transitions from bubbly to slug or churn-flow are included.

References

Al Issa, S.; Macian-Juan, R. “Experimental Investigation of CCFL in Large Diameter Hot-Leg Geometry”. Proceedings of ICONE21. Paper 16510. Chengdu, Chine (2013).

Al-Masry, W.A.; Ali, E.M.; Aqeel, Y.M. “Determination of bubble characteristics in bubble columns using statistical analysis of acoustic sound measurements”. Chem. Eng. Res. Des., 83 (A10): 1196-1207 (2005).

Al-Masry, W.A.; Ali, E.M. “Identification of hydrodynamic characteristics in bubble columns through analysis of acoustic sound measurements-Influence of the liquid phase properties”. Chem. Eng. Prosc., 46 (2): 127-138 (2007).

“ATHLET Mod 3.0 Cycle A: Program Overview”, Gesellschaft fur Anlagen und Reaktorsicherheit (GRS) mbH (2012).

Barbosa, J.; Govan, A.H.; Hewitt, G.F. “Visualization and modeling studies of churn flow in vertical pipe”. Int. J. Multiphase Flow, 27: 2105-2127 (2001).

Barkshi, B.R.; Zhong, H.; Jiang, P.; Fan L.S. “Analysis of flow in gas-liquid bubble columns using multi-resolution methods”. Chem. Eng. Res. Des., 73 (A6): 608-614 (1995).

Berthelsen, P. “A short introduction to the level set method and incompressible two-phase flow, a computational approach”. Report Norwegian University of Science and Technology (2002).

Bartosiewicz, Y.; Lavieville, J.; Seynhaeve, J.M. “A first assessment of the NEPTUNE_CFD code: instabilities in a stratified flow comparison between the VOF method and a two-field approach”. Int. J. of Heat and F. Flow 29 (2): 460-478 (2008).

Bestion, D.; Latrobe, A.; Paillere, H.; Laporta, A.; Techendorff, V.; Staedkte, H.; Aksan, N.; d’Auria, F.; Vihavainen, J.; Meloni, P.; Hewitt, G.; Lillingon, J.; Mavko, B.; Prosek, A.; Macek, J.; Malacka, M.; Camous, F.; Fichot, F.; Monhardt, D. “European Project for Future Advances in Science and Technology for Nuclear Engineering Thermal-Hydraulics – EUROFASTNET, Final Report” Technical Report, Commission of the European Communities (2002).

Bestion, D. “From the direct numerical simulation to system codes – perspective for the multi-scale analysis of LWR thermalhydraulics”. Nucl. Eng. Tech. 42(6) (2010).

Bestion, D. “Applicability of two-phase CFD to nuclear reactor thermalhydraulics and elaboration of Best Practice Guidelines”. Nucl. Eng. Des, In Press (2011).

Beyer, M.; Lucas, D.; Kussin, J.; Schütz, P. “Air-water experiments in a vertical DN200-pipe”. FZD-505 TOPFLOW Wissenschaftlich-Technische Berichte (2008).

Bhaga, D.; Weber, M.E. “Bubbles in viscous liquid: shapes, wakes and velocities”. J. Fluid Mech., 150: 61-85 (1981).

Bolotnov, I. A.; Jasen, K.E.; Drew, D. A.; Oberai, A. A.; Lahey, R. T.; Podowski, M. Z. “Detached direct numerical simulations of turbulent two-phase bubbly channel flow”. Int. J. Multiphase Flow, 37(6): 647-659 (2011).

Boure, J.A.; Bergles, A.E.; Tong, L.S. “Review of two-phase flow instability”. Nucl. Eng. And Des., 25:165-192 (1973).

Blumberg, P.N.; Lavoi, G.A.; Tabaczynsli, R.J. “Phenomenological models for reciprocating internal combustion engines”. Prog. in Energy and Comb. Sci., 5: 123-167 (1979).

Brackbill, J.U.; Kothe, D.; Zemach, C. “A continuum method for modeling surface tension”. J. Comput. Phys. 100: 335-354 (1992).

Briens, L.A.; Briens, C.L.; Margaritis, A.; Hay, J. “Minimum liquid fluidization velocity in gas-liquid-solid fluidized bed of low-density particles”. Chem. Eng. Sci., 52 (21-22): 4231-4238 (1997).

Burns, A.; Frank, T.; Hamill, I.; Shi, J. “The Favre Averaged Drag Model for Turbulent Dispersion in Eulerian Multi-phase Flows”. 5th International Conference on Multiphase Flow, ICMF04, Japan (2004).

Canot, E., Caltagirone, J.-P. “Test-case no. 10: parasitic currents induced by surface tension (PC)”. Multiphase Science and Technology 16, 69–74 (2004).

Černe, G.; Petelin, S.; Tiselj, I. ‘Coupling of the interface tracking and the two-fluid model for the simulation of the incompressible two-phase flow”. J. Comput. Phys. 171: 776-804 (2001).

CFX-Theory User Manual, ANSYS V14.0.

Chen, R.C.; Reese, J.; and Fan, F.-S. "Flow Structure in a Three-Dimensional Bubble Column and a Three-Phase Fluidized Bed". AIChE J., 40(7): 1093-1104 (1994).

Chen, P.; Dudukovic, M.P.; Sanyal, J. “Three-Dimensional Simulation of Bubble Column Flows with Bubble Coalescence and Breakup”. AIChE J., 51(3): 696-712 (2005).

Chen, J.; Yang, N.; Ge, W.; Li, J. “Computational Fluid Dynamics Simulation of Regime Transition in Bubble Columns Incorporating the Dual-Bubble-Size Model”. Ind. Eng. Chem. Res., 48: 8172-8179 (2009).

Collins, R. “The effect of a containing cylindrical boundary on the velocity of a large gas bubble in a liquid”. J. Fluid Mech., 28: 97-112 (1967).

Da Riva, E.; Del Col, D. “Numerical simulation of churn flow in a vertical pipe”. Chem. Eng. Sci., 64: 3753-3765 (2009).

Deendarlianto; Höhne, T.; Lucas, D.; Vallée, C.; Montoya, G. “CFD studies on the phenomena around counter-current flow limitations of gas/liquid two-phase flow in a model of a PWR hot leg”. Nuclear Eng. and Des., 241 (12): 5138-5148 (2011).

Drahos, J.; Zahradnik, J.; Puncochar, M.; Faviola, M.; Bradka, F. “Effect of operating conditions on the characteristics of pressure fluctuations in a bubble column”. Chem. Eng. Prosc., 292 (2): 107-115 (1991).

Drew, D.A. “Mathematical Modeling of Two-Phase Flow”. Ann. Rev. Fluid Mech., 15: 261 (1983).

Egorov, Y. “Contact condensation in stratified steam-water flow”. EVOL-ECORA –D07 (2004).

Ellenberger, J.; & Krishna, R. “A Unified Approach to the scaleup of gas-solid fluidized and gas-liquid bubble column reactors”. Chem. Eng. Sci., 49: 5391-5411 (1994).

Ellis, N.; Bi, H.T.; Lim, C.J.; Grace, J.R. “Influence of probe scale and analysis method on measured hydrodynamic properties of gas-fluidized beds”. Chem. Eng. Sci., 59 (8-9): 1841-1851 (2004).

Emonot, P.; Souyri, A.; Gandrille, J.L. “CATHARE 3: A new system code for thermal-hydraulics in the context of the NEPTUNE project”. The 13th International Topical Meeting on Nuclear Reactor Thermal Hydraulics (NURETH-13). Japan (2009).

“ERCOFTAC Best Practice Guidelines”. Computational Fluid Dynamics of Dispersed Multi-Phase Flows (2011).

Frank, Th.; Zwart P.J.; Krepper, E.; Prasser, H.-M.; Lucas, D. “Validation of CFD models for mono- and polydisperse air-water two-phase flows in pipes. Nucl. Eng. Des. 238: 647-659 (2008).

M.M. Francois, D.B. Kothe, E.D. Dendy, J.M. Sicilian, M.W. Williams, Balanced force implementation of the continuum surface tension force method into a pressure correction algorithm, Technical Report FEDSM2003-45175, in: Proceedings of the Seventh ASME/JSME Joint Fluids Engineering Conference, July 6–11, Honolulu, HI (2003).

Fu, X. “Interfacial area measurement and transport modeling in air-water two-phase flow”. PhD Thesis, Purdue University, U.S.A (2001).

Fu, X.; Ishii, M. “Two-group interfacial area transport in vertical air-water flow I. Mechanistic model”. Nuclear Eng. and Des., 219(2): 143-168 (2003).

Fukano, T.; Inatomi, T. “Analysis of liquid film formation in horizontal annular flow by DNS”. Int. J. Multiphase Flow, 29: 1413-1430 (2003).

Govan, A.H.; Hewitt, G.F.; Richter, H.J.; Scott, A. “Flooding and churn flow in vertical pipes”. Int. J. Multiphase Flow, 17: 27-44 (1991).

Griffith, P.; Wallis, G.B. “Two-phase slug flow”. J. Heat Transfer 83: 304-320 (1961).

Guillen, D.; Shelley, J.; Antal, S.; Tselishcheva, E.; Podowski, M.; Lucas, D.; Beyer, M. “Optimization of a Two-Fluid Hydrodynamic Model of Churn-Turbulent Flows”. Proceedings of the 17th International Conference on nuclear Engineering (ICONE17), Paper ICONE17-75113 (2009).

Harmathy, T.J. “Velocity of large drops and bubbles in media of infinite or restricted extent”. AIChE J., 6: 281-288 (1960).

Hänsch, S.; Lucas, D.; Krepper, E.; Höhne, T. “A multi-field two-fluid concept for transitions between different scales of interfacial structures”. Int. J. Mult. Flow 47:171-182 (2012).

Hänsch, S.; Lucas, D.; Höhne, T.; Krepper, E.; Montoya, G. “Application of a multi-field concept to the dam-break case with an obstacle”. Proc. of the 15th International Topical Meeting on Nuclear Reactor Thermalhydraulics, NURETH-15, Pisa, Italy (2013).

Hewitt, G.F.; Hall-Taylor, N.S. “Annular Two-Phase Flow”. Pergamon Press, Oxford, UK (1970).

Hewitt, G.F.; Martin, C.J.; Wilkes, N.S. “Experimental and modeling studies of annular flow in the region between flow reversal and the pressure drop minimum. PCH Physicochem. Hydrodyn., 6: 69-86 (1985).

Heywood, J.B. “Engine combustion modelling – An overview”. Combustion Modelling in Reciprocating Engines, Mattavi and Amann, Plenum Press (1980).

Hibiki, T.; Ishii, M. “Two-group interfacial area transport equations at bubbly-to-slug flow transition”. Nucl. Eng. Des., 202(1): 39-76 (2000).

Hinze, J. O. “Critical speed and size of liquid globules”. Appl. Scient. Res., A1: 275-288 (1948).

Holler, V.; Ruzicka, M.; Drahos, J.; Kiwi-Minsker, L.; Renken, A. “Acoustic and visual study of bubble formation processes in bubble column staged with fibrous catalytic layers”. Catalysis Today, 79-80: 151-157 (2003).

Hosokawa, S.; Tomiyama, A.; Misaki, S.; Hamada, T. “Lateral Migration of Single Bubbles Due to the Presence of Wall”. ASME 2002 Joint U.S.-European Fluids Engineering Division Conference. Montreal, QC, Canada (2002).

Höhne, T.; Vallée, C. “Experiments and numerical simulations of horizontal two-phase flow regimes using an interfacial area density model”. J. Comp. Fluid Dynamics (2010).

Höhne, T.; Deendarlianto; Lucas, D. “Numerical simulations of counter-current two-phase flow experiments in a PWR hot leg model using an area density model”. Int. J. Heat Fluid Flow 31 (5): 1047-1056 (2011).

Ishii, M.; Zuber, N. “Drag Coefficient and Relative Velocity in Bubbly, Droplet or Particle Flows”. AIChE J., 25: 843-855 (1979).

Ishii, M.; Kim, S. “Development of one-group and two-group interfacial area transport equation”. Nuclear Sci. and Eng. J., 146(3): 257-273 (2004).

Jayanti, S.; Hewitt, G.F.; Low, D.E.F.; Hervieu, E. “Observation of flooding in the Taylor bubble of co-current upwards slug flow”. Int. J. Multiphase Flow, 19: 531-534 (1993).

Jayanti, S.; Tokarz, A.; Hewitt, G.F. “Theoretical investigation of the diameter effect on flooding in countercurrent low”. Int. J. Multiphase Flow, 22: 307-324 (1996).

Kikuchi, R.; Yano, T.; Tsutsumi, A.; Yoshida, K.; Punchochar, M.; Drahos, J. “Diagnosis of chaotic Chem. Eng. Sci., 52 (21-22): 3741-3745 (1997).

Kim, S. “Interfacial area transport equation and measurement of local interfacial characteristics”. PhD Thesis, Purdue University (1999).

Kocamustafaogullari, G.; Ishii, M. “Foundation of the interfacial area transport equation and its closure relations”. Int. J. Heat and Mass Transfer, 38: 481-493 (1995).

Krepper, E.; Lucas, D.; Prasser, H.-M. “On the modelling of bubbly flow in vertical pipes”. Nucl. Eng. Des., 235: 597-611 (2005).

Krepper, E., Beyer, M.M Frank, Th.; Lucas, D.; Prasser, H.-M. “Application of a population balance approach for polydispersed bubbly flows”. 6th Int. Conf. on Multiphase Flow, Leipzig (2007).

Krepper, E.; Frank, Th.; Lucas, D.; Prasser, H.-M; Zwart, P.J. “The Inhomogeneous MUSIG model for the simulation of polydispersed flow”. Nucl. Eng. Des., 238: 1690-1702 (2008).

Krepper, E.; Ruyer, P.; Beyer, M.; Lucas, D.; Prasser, H.-M.; Seiler, N. “CFD simulation of polydispersed bubbly two-phase flow around an obstacle”. STNI Article ID 320738 (2009).

Krepper, E.; Rzehak, R.; Lucas, D. “Extended Validation of a Baseline Closure Model”. Application of CFM/CMFD Codes to Nuclear Reactor Safety and Design and heir Experimental Validation. Zurich, Switzerland (2014).

Krishna, R.; Ellenberger, J.; Hennephof, D.E. “Analogous description of the hydrodynamics of gas-solid fluidized beds and bubble columns”. Chem. Eng. J., 53(1): 89-101 (1993).

Krishna, R.; Urseanu, M.I.; van Baten, J.M.; Ellenberger, J. “Rise velocity of a swarm of large gas bubbles in liquids”. Chem. Eng. Sci., 54: 171-183 (1999).

Krishna, R.; van Baten, J.M. “Eulerian simulations of bubble columns operating at elevated pressures in the churn turbulent flow regime”. Chem. Eng. Sci., 56: 6249-6258 (2001).

Letzel, H.M.; Schouten, J.C.; Krishna, R.; Van Den Bleek, C.M. “Characterization of regimes and regime transition in bubble columns by chaos analysis of pressure signals”. Chem. Eng. Sc., 52 (24): 4447-4459 (1997).

Leyer, S.; Wich, M. “The integral Test Facility Karlstein”. Sci. Tech. Nucl. Inst., Article ID: 439374 (2012).

Levich, V. G. “Physicochemical Hydrodynamics”. Prentice-Hall, Englewood Cliffs, NJ. 636-546 (1962).

Liao, Y; Lucas, D. “A literature review of theoretical models for drop and bubble breakup in turbulent dispersions”. Chem. Eng. Sci., 64: 3389-3406 (2009).

Liao, Y; Lucas, D. “A literature review of theoretical models for the coalescence process of fluid particles”. Chem. Eng. Sci., 64: 3389-3406 (2010).

Liao, Y.; Lucas, D.; Krepper, E.; Schmidtke, M. “Development of a generalized coalescence and breakup closure for the inhomogeneous MUSIG model”. Nucl. Eng. Des., 24: 1024-1033 (2011).

Liao, Y.; Rzehak, R.; Lucas, D.; Krepper, E. “Baseline Closure Model for Dispersed Bubbly Flow: Bubble-Coalescence and Breakup”. Chem. Eng. Sci., 122: 336-349 (2015).

Lin, T.-J.; Reese, J.; Hong, T.; Fan, L.-S. “Quantitative analysis and computation of two-dimensional bubble columns”. AIChE J., 42 (2): 301-318 (1996).

Liu, X.; Lienhard J.H. “The hydraulic jump in circular jet impingement and in other thin liquid films”. Experiments in Fluids 15: 108-116 (1993).

Lo, S. “Application of the MUSIG model to bubbly flows”. AEAT-1096, AEA Technology. (1996)

Lopez de Bertodano, M. “Two Fluid Model for Two-Phase Turbulent Jet”. Nucl. Eng. Des. 179: 65-74 (1998).

Lucas, D.; Krepper, E.; Prasser, H.-M. “Development of co-current air-water flow in a vertical pipe”. Int. J. Mult. Flow. 31: 1304-1328 (2005).

Lucas, D.; Beyer, M.; Szalinski, P.; Schutz P. “A new database on the evolution of air-water flows along a large vertical pipe”. Int. J. Thermal Sci., 49: 664-674 (2010).

Luo, H; Svendson, H.F. “Theoretical model for drop and bubble break-up in turbulent flows”. AIChE J., 42(5): 1225-1233 (1996).

Manera, A.; Rohde, U.; Prasser, H.-M. Prasser; van der Hagen, T.H.J.J. “Modelling of flashing-induced instabilities in the start-up phase of

natural-circulation BWRs using the two-phase flow code FLOCAL". Nucl. Eng. And Des. 235: 1517-1535 (2005).

Mattavi, J.N.; Groff, E.G.; Lienesch, J.H.; Matekunas, F.A.; Noyes, R.N. "Engine improvements through combustion modelling". Combustion Modelling in Reciprocating Engines, Mattavi and Amann, Plenum Press (1980).

Matsui, G. "Identification of flow regimes in vertical gas-liquid two-phase flow using differential pressure fluctuations". Int. J. Multiphase Flow, 10 (6): 711-720 (1984).

Mayinger, F.; Weiss, P.; Wolfert, K. "Two-phase flow phenomena in full-scale reactor geometry". Nucl. Eng. And Des, 145: 47-61 (1993).

McQuillan, K.W.; Whalley, P.B.; Hewitt, G.F. "Flooding in vertical two-phase flow". Int. J. Multiphase Flow, 11: 741-760 (1985).

Minato, A.; Takamori, K.; Ishida, N. "An extended two-fluid model for interphase behavior in gas-liquid two-phase flow". Proc. 8th Int. Conf. Nucl. Eng., ICONE-8045, April 2-6, Baltimore, USA (2000).

Mishima, K.; Ishii, M. "Flow regime transition criteria for upward two-phase flow in vertical tubes". Int. J. Heat and Mass Transfer, 27(5): 723-737 (1984).

Montoya, G.; Deendarlianto; Lucas, D.; Höhne, T; Vallée, C. "Image-Processing-Based Study of the Interfacial Behavior of the Countercurrent Gas-Liquid Two-Phase Flow in a Hot Leg of a PWR". Sci. Tech. Nuclear Int., Article ID: 209542 (2012).

Montoya, G.; Liao, Y; Lucas, D.; Krepper, E. "Analysis and Applications of a Two-Fluid Multi-Field Hydrodynamic model for Churn-Turbulent Flows". Proceedings of the 2013 21st International Conference on Nuclear Engineering (ICONE21) – ICONE21-16297. Chengdu, China (2013).

Montoya, G.; Lucas D.; Krepper, E.; Hänsch, S.; Baglietto, E. "Analysis and Applications of a Generalized Multi-Field Two-Fluid Approach for Treatment of Multi-Scale Interfacial Structures in High Void Fraction Regimes". Proc. Int. Congress on Adv. on Nucl. Power Plants. ICAPP2014-14230, USA (2014a).

Montoya, G.; Baglietto, E.; Lucas, D.; Krepper, E.; Höhne, T. "Comparative Analysis of High Void Fraction Regimes using an Averaging Euler-Euler Multi-Fluid Approach and a Generalized Two-Phase Flow (GENTOP) concept". Proceedings of the 2014 22st International Conference on Nuclear Engineering (ICONE22). Prague, Czech Republic (2014).

Montoya, G.; Baglietto, E.; Lucas, D. "Implementation and Validation of a Surface Tension Model for the Multi-Scale Approach GENTOP". Proceedings of the 16th International Topical Meeting on Nuclear Reactor Thermalhydraulics (NURETH-16). Chicago, USA (2015).

Murray, C. "Overview of TRACE V5.0". Regulatory Information Conference. U.S.NRC (2007).

Murzyn, F.; Chanson, H. “Free surface fluctuations in hydraulic jumps: experimental observation Exp. Therm. Fluid Sci. 33: 1055-1064 (2009).

Navarro, M. “Study of countercurrent flow limitation in a horizontal pipe connected to an inclined one”. Nucl. Eng. Des., 235 (10-12):1139-1148 (2005).

Nicklin, D.J.; Davidson, J.F. “The onset of instability in two-phase slug flow”. Int. Mech. Eng. Proc. Symp. Two-phase Flow, Paper No. 4 (1962).

Nishikawa, K.; Sekoguchi, K.; Fukano, T. “On the pulsation phenomena in gas-liquid two-phase flow”. Bulletin of JSME, 12 (54): 1410-1416 (1969).

Olmos, E.; Gentric, C.; Poncin, S.; Midoux, N. “Description of flow regime transitions in bubble columns via laser Doppler anemometry signals processing”. Chem. Eng. Sci., 58 (9): 1731-1742 (2003).

Osher, S.; Sethian, J. A. "Fronts propagating with curvature-dependent speed: Algorithms based on Hamilton–Jacobi formulations", J. Comput. Phys. 79: 12–49 (1988).

Owen, D.G.; Hewitt, G.F. “An improved annular two-phase flow model”. Proc. Third International Conference on Multiphase Flow, The Hague, Netherlands, Paper C1 (1986).

Pan, Y.; Duduković, M.P. “CFD Simulations of a Bubble Column-2D versus 3-D”. Proc. Of 6th World Congress of Chemical Engineering, Melbourne, Australia (2001).

Park, Soung Hee; Kim, Sang Done. “Characterization of pressure signals in a bubble column by wavelet packet transform”. Korean J. Chem. Eng., 20 (1): 128-132 (2003).

Parvareh, A.; Rahimi, M.; Alizadehdakhel, A.; Alsairafi, A.A. “CFD and ERT investigations on two-phase flow regimes in vertical and horizontal tubes”. Int. Communication in Heat and Mass Transfer, 37: 304-311 (2010).

Podowski, M.Z. “On the consistency of Mechanistic Multidimensional Modeling of Gas/Liquid Two-Phase Flows”. Nucl. Eng. Des., doi: 10.1016/j.nucengdes.2008.10.022 (2009).at

Pokharna, H.; Mori, M.; Ransom, V. “Regularization of Two-Phase Flow Models: A Comparison of Numerical and Differential Approaches”. J. Comp. Phys., 134: 282-295 (1997).

Prasser, H.-M; Beyer, M.; Carl, H.; Manera, A.; Pietruske, H.; Schütz, P. “Experiments on upwards gas/liquid flow in vertical pipes”. FZD-482 TOPFLOW Wissenschaftlich-Technische Berichte (2007).

Prince, M.J.; and Blanch, H.W. “Bubble Coalescence and Break-Up in Air-Sparged Bubble Columns”. AIChE J., 36(10): 1485-1499 (1990).

RELAP5/MOD3 Code Manual Volume I: Code Structure, System, Models, and Solution Methods, RELAP 5 Code Development Team, NUREG/CR-

5535, INEL-95/0174, Volume I, Idaho National Engineering Laboratory (1995).

Robert, M; Farvacque, M.; Parent, M.; Faydilde, B. “CATHARE 2 V2.5: a fully validated CATHARE version for version for various applications”. The 10th International Topical Meeting on Nuclear Reactor Thermal Hydraulics (NURETH-10). Seoul, Korea (2003).

Rzehak, R.; Krepper, E. “Bubble induced turbulence: Comparison of CFD models”. International Symposium on Multiphase flow and Transport Phenomena. Agadir, Morocco. April 22-25 (2012).

Rzehak, R.; Krepper, E.; Ziegenhein, T.; Lucas, D. “A Baseline Model for Monodispersed Bubbly Flows”. 10th International Conference on CFD in Oil & Gas, Metallurgical and Process Industries (CFD2014). Trondheim, Norway (2014).

Sato, Y., Sekoguchi, K. “Liquid velocity distribution in two-phase bubble flow”. Int. J. Multiphase Flow, 2: 79 (1975).

Schiller, L.; Naumann, A.“ Über die grundlegenden Berechnungen bei der Schwerkraftaufbereitung“. Z. Ver. Dtsch. Ing., 77: 318-326 (1935).

Shaikh, A; Al-Dahan, M. “A Review on Flow Regime Transition in Bubble Columns”. Int. J. Chem. Reactor Eng., 5(R1) (2007).

Shah, Y.T.; Kelkar, B.G.; Godbole, S.P.; Deckwer, W.-D. “Design Parameters Estimations for Bubble Column Reactors”. AIChE J., 20(3): 353-379 (1982).

Shawkat, M.E.; Ching, C.Y.; Shoukri, M. “Bubble and liquid turbulence characteristics of bubbly flow in a large diameter vertical pipe”. Int. J. Mult. Flow, 34: 767-785 (2008).

Sosnovsky, E. “Nuclear Reactor Multiphysics via Bond Graph Formalism”. Doctor of Science in Nuclear Science and Engineering Thesis, Massachusetts Institute of Technology (2014).

Stevanovic, V.; Prica, S.; Maslovaric, B. “Multi-Fluid Model Predictions of Gas-Liquid Two-Phase Flows in Vertical Tubes”. FME Transactions, 35(4): 173-181 (2007).

Stewart, C. W. “VIPRE-01: a thermal hydraulic code for reactor cores”. NP-2246-SR: 1-3. Electric Power Research Institute, Palo Alto, Calif., USA (1989).

Strubelj, L.; Tiselj, I.; Mavko, B. “Simulations of free surface flows with implementation of surface tension and interface sharpening in the two-fluid model”. Int. J. Heat Fluid Flow 30: 741-750 (2009).

Sun, X. “Two-group interfacial area transport equation for a confined test section”. PhD Thesis, Purdue University (2001).

Sun, X.; Ishii, M.; Kelly, J.M. “Modified Two-Fluid Model for the Two-group Interfacial Area Transport Equation: Ann. Nucl. Energy. 30:1601 (2003).

Sun, X.; Kim, S.; Ishii, M.; Beus, S.G. “Modeling of bubble coalescence and disintegration in confined upward two-phase Flow.” Nuclear Eng. and Des., 230(1-3): 3-26 (2004).

Sun, X; Liu, Y.; Ozar, B.; Ishii, M.; Kelly, J. “Study on Drag Coefficients for Two Groups of Bubbles”. Proceedings of the 12th International Conference on Nuclear Engineering. Arlington, Virginia, USA (2004b).

Sussman, M.; Smereka, P.; Osher, S. “A level set approach for computing solutions to incompressible two-phase flow”. J. Comput. Phys. 114: 146-159 (1994).

Taitel, Y.; Barnea, D.; Dukler, A.E. “Modeling flow pattern transition for steady upwards gas-liquid flow in vertical tubes”. AIChE J., 29: 345-354 (1980).

Takamasa, T.; Tomiyama, A. “Three-Dimensional Gas-Liquid Two-Phase Bubbly Flow in a C-Shaped Tube”. Ninth International Topical Meeting on Nuclear Reactor Termal Hydraulics (NURETH-9), San Francisco, CA (1999).

Tiselj, I.; Stojan, P. “Modelling of Two-Phase Flow with Second-Order Accurate Scheme”. J. Comp. Phys., 136: 503-521 (1997).

Tomiyama, A. “Struggle with Computational Bubble Dynamics”. Proceedings International Conference on Multiphase Flow, France (1998).

Tomiyama, A.; Shimada, N. “(N+2)-field modeling for bubbly flow simulation”. Comput. Fluid Dyn. J. 9 (4): 418-426 (2001).

Tomiyama, A. “Rising Velocities and Shapes of Single Bubbles in Vertical Pipes” Proc. ICMF, New Orleans, USA (2001b).

Tomiyama, A.; Tamai, H.; Zun, I.; Hosokawa, S. “Transverse Migration of Single Bubbles in Simpler Shear Flows”. Chem. Eng. Sci., 57: 1849-1858 (2002).

Tomiyama, A.; Sakoda, K.; Hayashi, K.; Sou, A.; Shimada, N.; Hosokawa, S. “Modeling and Hybrid Simulation of Bubbly Flow”. Multiphase Sci. Tech., 18: 73-110 (2006).

TRACE V5.0 Assessment Manual, United States Nuclear Regulatory Commission.

TRACE V5.0 Theory Manual: Field equations, solution methods, and physical models, United States Nuclear Regulatory Commission.

Tryggvason, G.; Bunner, B.; Esmaeeli, A.; Juric, D.; Al-Rawahi, N.; Tauber, W.; Han, J.; Nas, S.; Jan, Y.-J. “A Front Tracking Method for the Computations of Multiphase Flow”. J. Comp. Physics 169: 708-759 (2001).

Tselishcheva, E.; Podowski, M.; Antal, S.; Guillen, D.; Beyer, M; Lucas, D. “Analysis of Developing Gas/Liquid Two-Phase Flows”. 7th International Conference on Multiphase Flow (ICMF) (2010).

Tsuchiya, K.; Furumoto, A.; Fang, L.S.; Zhang, J. “Suspension Viscocity and Bubble Rise Velocity in Liquid-Solid Fluidized Beds”. Chem. Eng. Sci., 52: 3053 (1997).

Urseanu, M. “Scaling up bubble column reactors”. PhD Thesis, University of Amsterdam. Amsterdam, Netherlands (2000).

Vermeer, D.; Krishna, R. “Hydrodynamics and Mass Transfer in Bubble Columns Operating in the Churn-Turbulent Regime”. Ind. Eng. Chem. Process Des. Dev., 20(3): 475-482 (1981).

Vial, C.; Poncin, S.; Wild, G.; Midoux, N. “A simple method for regime identification and flow characterization in bubble columns and airlift reactors”. Chem. Eng. Prosc., 40 (2): 131-151 (2001).

Vijayan, P.K.; Austregesilo, H.; Teschendorff, V. “Simulation of the unstable oscillatory behavior of single-phase natural circulation with repetitive flow reversals in a rectangular loop using the computer code ATHLET”. Nucl. Eng. And Des, 155: 623-641 (1995).

Yuan, Y.; Randall, L. “Surface Science Techniques”. Springer Series in Surface Sciences, Vol. 51 (2013).

Walley, P.B. “Boiling, Condensation, and Gas-Liquid Flow”. Clarendon Press, Oxford (1987).

Wallis, G.B. “The onset of droplet entrainment in annular gas liquid flow”. General Electric Report, No. 62 GL127 (1962).

Wallis, G.B. “One-Dimensional Two Phase Flow”. New York McGraw-Hill (1969).

Wang, X. “Simulations of Two-phase Flows Using Interfacial Area Transport Equation”. PhD Dissertation, The Ohio State University (2010).

Weisman, J. “Elements of nuclear design”. Second Edition. Elsevier Scientific Pub. Co, New York, USA (1983).

Williams, M.W.; Kothe, D.B.; Puckett, E.G. “Accuracy and Convergence of Continuum Surface Tension Models”. LA-UR-98-2268 (1998).

Wheeler, C.L.; Stewart, C.W.; Cena, R.J.; Rowe, D.S.; Sutey, A.M. “COBRA-IV-I: An interim version of COBRA for thermal-hydraulic analysis of rod bundle nuclear fuel elements and cores”. Technical Report BNWL-1962, Pacific Northwest Laboratories, Richland, WA, USA (1977).

Zhang, J.-P.; Grace, J.R.; Epstein, N.; Lim, K.S. “Flow regime identification in gas-liquid flow and three-phase fluidized beds”. Chem. Eng. Sci., 52 (21-22): 3979-3992 (1997).

Ziegenhein, T.; Rzehak, R.; Lucas, D. “Transient Simulation for Large Scale Flow in Bubble Columns”. Chem. Eng. Sci., 122 (2015).

Zuber, N.; Findlay, J.A. “Average volumetric concentration in two-phase flow systems”. J. Heat Transfer, 87: 453-468 (1965).

Appendix A

A.1 Annular Flows.

One of the main motivations for this doctoral dissertation is based on the future possibility of full boiling calculation for PWR and BWR, both in core and safety systems. While not a direct objective of the dissertation, it is important to emphasize that all the modifications which have been done to the original GENTOP concept during this work, have allowed the possibility of finally modeling annular flows with certain limitations. This was not possible with the previous version of the concept. The calculations presented here are based on the TOPFLOW facility case 184. The gas and liquid superficial velocities are 3.185 m/s and 1.017 m/s, respectively. The continuous gas is named "Gas3", and "Gas2" is the dispersed polydispersed field. The separation between the two gas-fields is based on the sign change from the Tomiyama lift coefficient.

Qualitatively (Fig. A.1), the results look similar to the experimental data, where a continuous core of gas ("Gas3") moves to the center of the pipe. The smaller bubbles represented by "Gas2" have the higher concentration closer to the walls, and could be also entrained alongside the distorted gas-core structures.

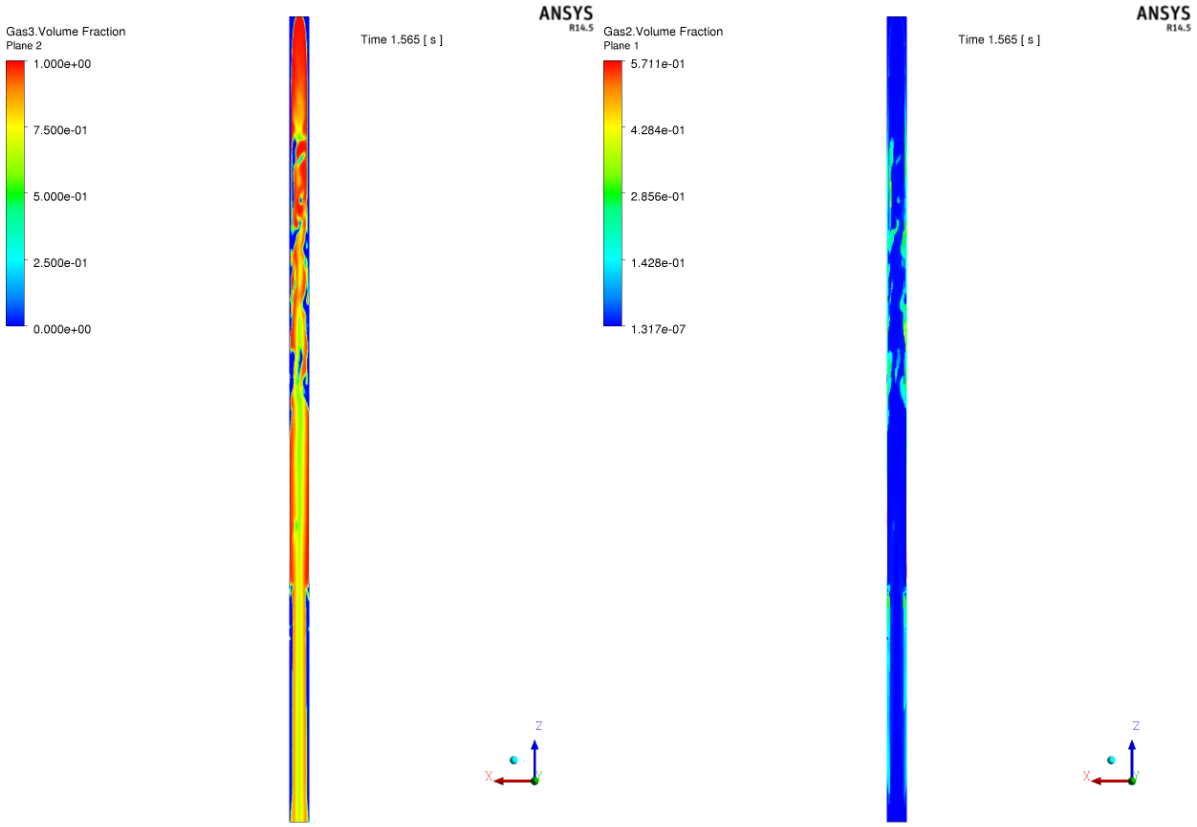

Figure A.1 Plane contour exemplification of the continuous gas for TOPFLOW experiment case 184 A) without and B) with transient boundary conditions.

Quantitatively, as it can be observed from the inlet boundary profile (Fig. A.2a), only continuous gas is injected. At L/D = 2.8, some of the continuous gas has broken up, and dispersed gas can be seen concentrated at the walls of the system (Fig. A.2b). By the middle of the pipe at L/D = 22.9, the continuous gas has still not dispersed enough from the wall injection to be comparable to the experimental data (Fig. A.3a). It is not until L/D = 39.9, that the void radial profile shows a similar trend as in the experimental data, showing a slight overall under prediction (Fig. A.3b).

All velocity profiles (Fig. A.4 and A.5) show a very good agreement against the experimental data. While for L/D = 22.9 there is still a not-completely flat profile for the void at the center core of the pipe, the velocity prediction at this point agreed quite well with the experiments.

While these are by no means perfect results, they clearly show the potential of the latest formulation of the GENTOP concept alongside the iMUSIG approach to model highly complex flows, including, maybe in the near future, the full boiling phenomenon with transitions from low to high void fraction regimes.

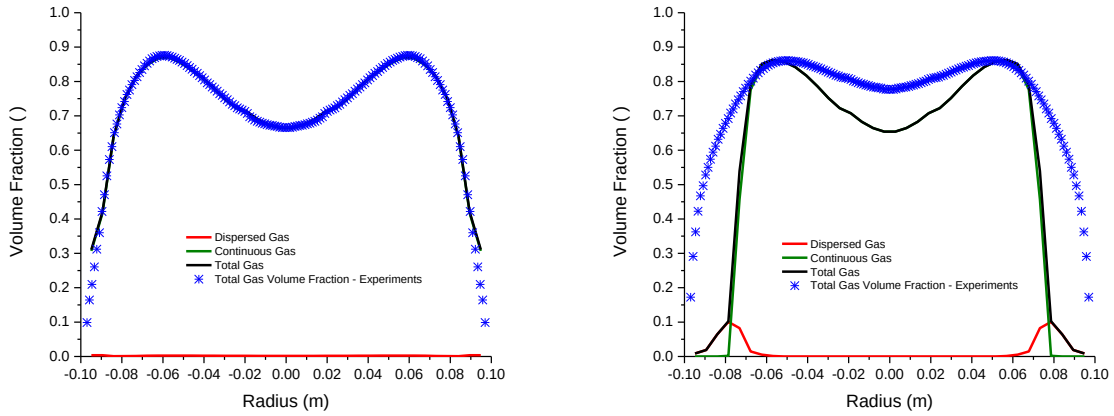

Figure A.2 Void fraction radial distribution of TOPFLOW calculation case 184 with at A) L/D = 1.4 and B) L/D = 2.8.

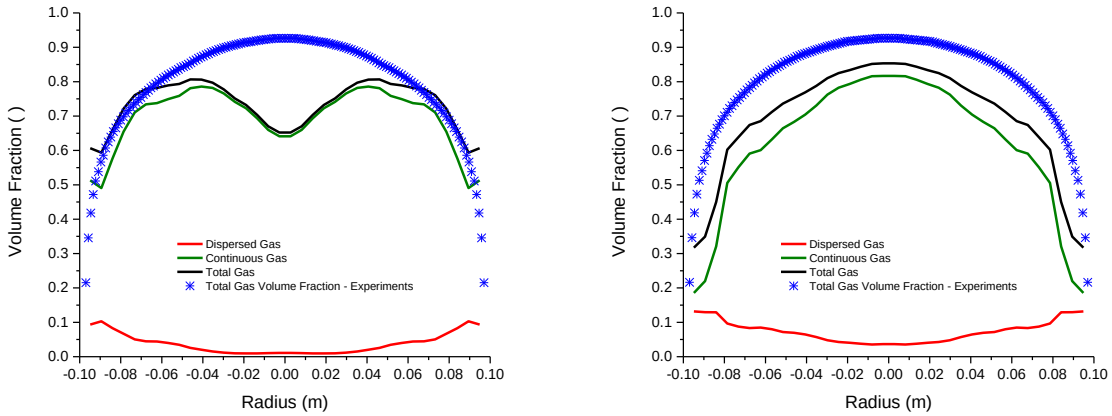

Figure A.3 Void fraction radial distribution of TOPFLOW calculation case 184 with at A) L/D = 22.9 and B) L/D = 39.7.

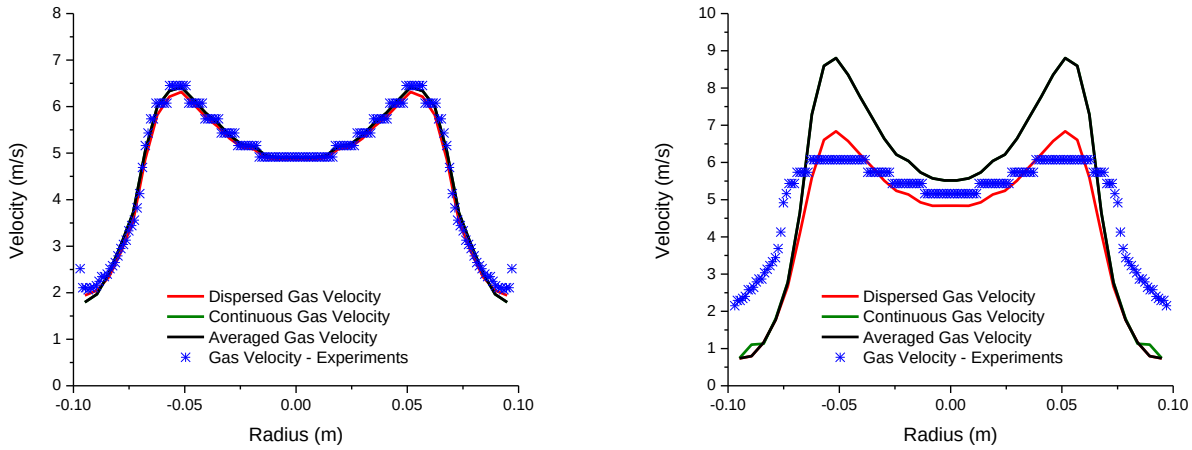

Figure A.4 Velocity distribution of TOPFLOW calculation case 184 with at A) L/D = 1.4 and B) L/D = 2.8.

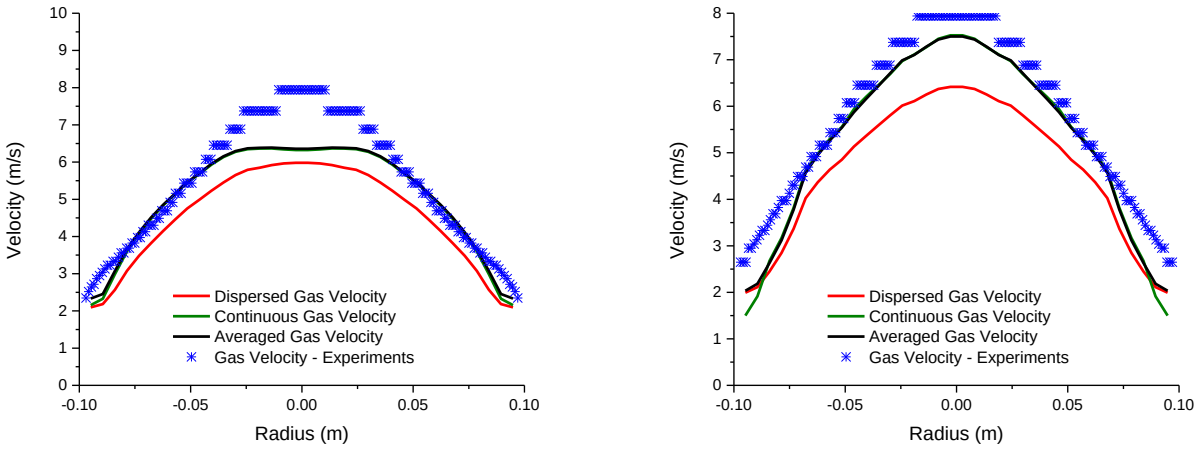

Figure A.5 Velocity distribution of TOPFLOW calculation case 184 with at A) L/D = 22.9 and B) L/D = 39.7.